A New Femtosecond Electron Diffractometer for Structural Dynamics Experiments at Cryogenic Temperatures

by

Albert Bart Smit

Thesis presented in partial fulfilment of the requirements for the degree of Master of Science in Laser Physics in the Physics Department at Stellenbosch University

Department of Physics,
University of Stellenbosch,
Private Bag X1, Matieland 7602, South Africa.

Supervisor: Prof. H. Schwoerer

December 2014

Declaration

By submitting this thesis electronically, I declare that the entirety of the work contained therein is my own, original work, that I am the sole author thereof (save to the extent explicitly otherwise stated), that reproduction and publication thereof by Stellenbosch University will not infringe any third party rights and that I have not previously in its entirety or in part submitted it for obtaining any qualification.

Signature: .....
A.B. Smit

Date: 10 November 2014 .....

Abstract

A New Femtosecond Electron Diffractometer for Structural Dynamics Experiments at Cryogenic Temperatures

A.B. Smit

Department of Physics,
University of Stellenbosch,
Private Bag X1, Matieland 7602, South Africa.

Thesis: MSc

December 2014

In this thesis, a femtosecond electron diffraction (FED) set-up that is capable of investigating the photo-induced switching of $Cu(DCNQI)_2$ from being an insulator to being a conductor is presented. Movies of atomic structural changes with temporal resolution within the typical photo-switching transition timescales (sub-picoseconds) are obtainable with this set-up by employing a femtosecond laser. The experimental technique and the design of a crucial instrument of the machine, the electron gun, are extensively described and characterised both numerically and experimentally.

The interest in observing atomic structural changes of $Cu(DCNQI)_2$ in real time is because of the rich variety of the radical salts available that show alloy-specific Charge Density Wave (CDW) transitions. Valuable insights about the driving mechanisms behind these structural changes that are responsible for a change in conductivity are obtainable, as well as the relation between crystal alloys and their transition characteristics. Electron diffraction patterns of crystals in their metallic phase (room temperature) are shown in this thesis, but diffraction patterns of cryo-cooled $Cu(DCNQI)_2$ in its insulating phase are still to be acquired.

The temporal resolution of the atomic movie can be improved by recompression of electron pulses that are debunched due to Coulomb repulsion and electron energy spread within a pulse. Numerical and preliminary experimental results presented in this work expose the potential of a simple compression technique. In this way, more electrons in a single electron pulse can be afforded which allows to perform experiments at shorter integration time or lower repetition rate.

Uittreksel

'n Nuwe Femtosekonde Elektron Diffraksiemeter vir Strukturele Dinamika Eksperimente by Cryogene Temperature

("A New Femtosecond Electron Diffractometer for Structural Dynamics Experiments at Cryogenic Temperatures")

A.B. Smit

Departement Fisika,
Universiteit van Stellenbosch,
Privaatsak X1, Matieland 7602, Suid Afrika.

Tesis: MSc

Desember 2014

In hierdie tesis word 'n femtosekonde elektron diffraksie opstelling aangebied wat daartoe in staat is om die foto-geïnduseerde omskakeling in $Cu(DCNQI)_2$ van nie-geleier tot geleier te ondersoek. Deur gebruik te maak van 'n femtosekonde laser in hierdie opstelling, is 'rolprente' van strukturele veranderinge op atoomskaal met 'n tyd resolusie beter as die tipiese foto-omskakelings tydskaal (sub-pikosekonde) verkrygbaar. Die eksperimentele tegniek en die ontwerp van 'n noodsaaklike instrument van die masjien, die elektron geweer, word breedvoerig beskryf en numeries en eksperimenteel gekenmerk.

Die belangstelling om strukturele veranderinge in $Cu(DCNQI)_2$ op atoom skaal in reële tyd waar te kan neem is as gevolg van die ryke verskeidenheid van radikale soute, wat allooispesifieke ladings digtheid golf (CDW) oorgange toon, wat beskikbaar is. Waardevolle insigte oor die meganismes wat hierdie strukturele veranderinge wat 'n verandering in geleiding veroorsaak dryf is verkrygbaar, sowel as die verwantskap tussen die kristal allooi en die oorgang kenmerke. Diffraksie patrone van kristalle in die metaalagtige fase (kamer temperatuur) word in hierdie tesis getoon, maar diffraksie patrone van cryo-verkoelde $Cu(DCNQI)_2$ in die nie-geleier fase moet nog verkry word.

Die tyd resolusie van die atomiese rolprent kan verbeter word deur die elektron puls — wat deur Coulomb afstoting en elektron energie spreiding versprei is — weer saam te pers. Numeriese en voorlopige eksperimentele resultate toon die potensiaal van 'n eenvoudige kompressie tegniek. Hierdeur kan meer elektrone in 'n elektron puls gegun word en so die integrasie tyd of die herhalingstempo van die eksperimente verkort kan word.

Samenvatting

In deze thesis wordt een femtoseconde elektron diffractie opstelling gepresenteerd dat in staat is om de foto-geinduceerde insulator-tot-geleider omschakeling in $Cu(DCNQI)_2$ te onderzoeken. Filmpjes van atomische structurele veranderingen met een tijdresolutie beter dan de typische foto-omschakelings tijdschaal (sub-picoseconde) zijn verkrijgbaar met deze set-up door gebruik van een femtoseconde laser. De experimentele techniek en het ontwerp van een cruciaal instrument van de machine, het elektronen kanon, worden uitvoerig beschreven en numeriek en experimenteel gekarakteriseerd.

De interesse om atomische structurele veranderingen in $Cu(DCNQI)_2$ in real-time waar te kunnen nemen komt door de rijke variatie die van deze radicale zouten beschikbaar zijn die allooi-specifieke ladings dichtheid golf (CDW) transities bevatten. Waardevolle inzichten over de drijvende mechanismen achter deze structurele veranderingen die een verandering in geleiding veroorzaken zijn verkrijgbaar, zowel als de relatie tussen de variatie van kristal allooi en de transitie kenmerken. Diffractie patronen van kristallen in de metallische fase (kamer temperatuur) worden in deze thesis getoond, maar diffractie patronen van cryo-gekoelde $Cu(DCNQI)_2$ in de isolator fase moeten nog verworven worden.

De tijdresolutie van de atomische film kan verbeterd worden door de elektron puls — die ontbundeld is door Coulomb afstoting en elektron energie spreiding — weer samen te persen. Numerieke en voorlopige experimentele resultaten gepresenteerd in dit werk tonen de potentie van een eenvoudige compressietechniek. Hierdoor kunnen meer elektronen in een elektron puls worden veroorloofd waardoor de integratie tijd of de herhalingsfrequentie van de experimenten verkort kan worden.

Acknowledgements

The results presented in this thesis would not have been possible without the help and support of a lot of people. Therefore, I would like to start by thanking some of them.

The first person to thank is my supervisor Prof. Heinrich Schwoerer for making my dream to do a Master of Science in South Africa become reality. I am forever grateful for the opportunity of doing my post-graduate studies in this beautiful country in an excellent academic environment. This really was an opportunity with which I couldn't do anything else than take it with both hands. Heinrich's inexhaustible supervision that goes beyond academics makes me confident that the choice to do my degree in his group was the right one. The intensive involvement that he provides helped me grow my skills in experimental physics. I am thankful for him allowing his students to gain benefit from all the international contacts that he has. We all acquired a lot of knowledge when pioneers from the FED community were attracted to Stellenbosch for a workshop that was organised in October 2013.

Furthermore, I would like to thank my former lab-colleague Dr. Nicolas Erasmus for the efforts that he has made and the patience that he has had while teaching me how to work with the set-up. I am thankful for his welcoming approach of introducing me to the lab and to a new country. Also, a word of thanks to Aminat Suleiman for her significant contributions in the laboratory and Florian Hüwe for growing the crystals that we are currently investigating. Thanks to Kerstin Haupt and Andrea Rohwer for preparing the sample to be FED-proof. In general, I'd like to say a big thanks to all the Laser Research Institute (LRI) colleagues for creating such a pleasant atmosphere and great working environment.

A special thanks to the excellent departmental workshop for without them we would not have been where we are now. I especially express my gratitude to Lawrence Ashworth who built and tested the new vacuum chamber and who built the electron gun that is presented and characterised in this thesis. Also thanks to Gerhard Louwrens, who is an outstanding technician in terms of laser technology, electronics and anything else that he is asked for.

Last but not least I would like to thank my parents for being so supportive in my decision to pursue my goal to study in South Africa — *ontzettend bedankt voor jullie onvoorwaardelijke steun en support in elke keuze die ik maak.* To Lungile Sithole, words can't describe my gratitude for your loving support and understanding during the scope of this project — *ngiyabonga kakhulu.*

Contents

1. Introduction

Following the movement of atoms in matter in real time down to the femtosecond (10^{-15} s) timescale gains great interest of physicists, chemists and biologists. The ability to observe the evolution of structural changes can provide insight and fundamental understanding of a whole range of problems. Examples of such problems are photoinduced reactions in fundamental physics and biochemistry, like transitions in condensed matter between different phases of conductivity, magnetism and structure. In an attempt to understand displacement of atoms during transitions, of which one is discussed in this thesis, being able to directly make a time resolved movie on atomic scale can reveal hints of how transitions function and how they are directed. In other words: a technique for four-dimensional measurements allowing to be able to watch atomic motions is desirable.

Unfortunately, the human eye is only sensitive to the visible light in the electromagnetic spectrum, meaning that we are diffraction limited and can't directly resolve atomic structures even if the strongest optical microscope is used. Waves with a short enough wavelength — and thus a sufficiently low diffraction limit — can resolve atomic separation that is typically in the Angström (10^{-10} m) order. X-ray and electron sources have thus been used to resolve static atomic structures. But, introducing the time as the fourth dimension makes things even more complicated: time scales of intrinsic motions, vibrations and phonon periods are down to the picosecond (10^{-12} s) regime. The human eye only has a temporal resolution of 40 – 100 ms[1] and even the best electronics are not fast enough to be employed for capturing atomic motion. So in order to make four-dimensional molecular movies, a technique should be employed that is not based on electronics but on the speed of light.

Before jumping into the details of how atomic spatial accuracy in combination with sufficient temporal resolution is achieved, let us first look at a simple analogy to explain the concepts behind such experiments.

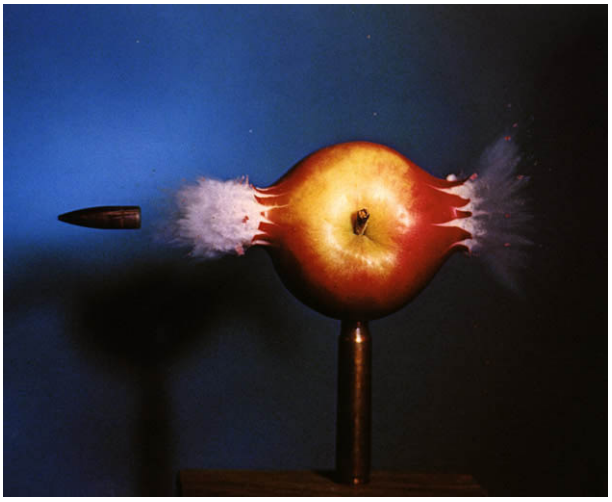

Figure 1.1: A stroboscope is used to capture a sharp image of fast dynamics happening in an apple, something that could not have been achieved by a slow detector. Picture taken from [2].

To start off, a fast dynamical transition in the macroscopic world is considered. Displayed in figure 1.1 is a photo from 1964 of an apple exploding after it has been 'pumped' with a bullet. With long shutter times of around 20 ms for normal 'slow' detectors, it would not be possible to acquire pictures that are as sharp as these. With a bullet travelling at $v = 300$ m/s, the bullet would have travelled 6 m during acquisition of this photo. The solution is to put the sample — the apple — in a perfectly dark room. If a light flash with a duration of $\frac{1}{3}$ µs is switched on shortly after the explosion, the slow camera will only collect data during the arrival of this short 'probe' stroboscope flash. Temporal resolution of the image is now not determined by camera's shutter time, but by the duration of the probe pulse. The bullet only travels 0.1 mm while being exposed to the light flash. The way forward to make a full movie of this explosion instead of a single image could be done by replacing the apple with a new one after each pump shot. The experiment should be repeated, but the delay between pump (bullet) and probe (light pulse) arrival time should be increased after each shot. This will only work if the apple explodes in a similar manner for each shot. Better would be the availability of an apple that returns back to its original state from shot to shot. Another advantage of that case is the repeatability of the same experiment. One could consider averaging over multiple shots for a single pump-probe delay time in order to increase brightness of the photo.

This pump-probe technique explains the principles of Femtosecond Electron Diffraction (FED) and Ultrafast X-ray Diffraction (UXD) which are techniques used to watch atomic motions directly in crystalline matter. Experimentally, ultrabright electron[3; 4] and X-ray sources[5] have been successfully used to observe atomic motion directly. The pump in the case of atomic movies (as opposed to macroscopic movies) is a short laser pulse that is directly irradiating the sample (as opposed to an actual bullet). The photoexcitation, with appropriate pulse energy, serves to initiate whatever transition that is under investigation. As a probe — a stroboscope flash in the macroscopic analogy — either an X-ray or electron 'flash' with a sufficiently low diffraction limit is used. For the exposure time of each frame in the molecular movie to be short (and thus temporal resolution to be high), these X-ray or electron 'flashes' (or more scientifically: pulses) need to be short. Both FED and UXD have shown to be effective in atomically resolving structural dynamics. In our laboratory, we chose for a 'table-top' FED set-up. It is a simpler and more compact set-up, whereas expensive high intensity lasers or bulky synchrotrons would be needed for UXD.

Perfect synchronisation between the short pump light pulse and the short electron probe pulse is achieved by having both paths come from the same laser source. Different temporal 'snapshots' to map out long time-evolutions of dynamics are acquired by carefully changing the delay between the pump and the probe in order to tune their arrival times. The $t = t_0$ position (time of pump impact) can be determined so that the temporal response can be correlated to the movie. For samples that fully reverse back to their original state from shot to shot upon photo-excitation (which was not the case in the apple-bullet analogy), integration over many shots improves the signal-to-noise ratio needed to monitor structural changes.

The first FED molecular movie published in 2003 was on the melting of 10 – 100 nm thin aluminium samples, revealing the homogeneous nucleation on an atomic level during this phase transition by analysing the disappearing of diffraction rings within hundreds of femtoseconds[6]. This opened the door for more advanced experiments such as photoinduced structural changes during more exotic phase transitions. Work done on TaS_2 samples, for example, pushed the field to perform close to its 200 fs temporal limit and gained valuable insight into how the strong electron-lattice correlation energy drives a metal-to-insulator transition[7]. Our South African research chair in photonics has contributed significantly to the field by having published molecular movies of similar phase transitions in $TaSe_2$ crystals. Knowledge on

the forces that act during photoexcitation that lead to structural phase transitions (and thus a change in material properties) was gained during this research. Former colleagues and Ph.D. students Dr. Kerstin Haupt and Dr. Nicolas Erasmus have both performed successful FED experiments on different types of $TaSe_2$ and TaS_2 crystals in our set-up[8; 9]. Dr. Erasmus has used the $TaSe_2$ sample to demonstrate the potential for an alternative method of data collection where one in theory can resolve an entire molecular movie in a single shot experiment[10]. This is specifically relevant for the investigation of samples that do not fully reverse back to their initial state upon photoexcitation (or those that are destroyed when exposed to a limited number of shots), such as some biological samples.

Advancements have accumulated ever since, such as the publication of FED experiments on the photoinduced opening reaction of a cyclisation-ring in diarylethene[11], as well as a photoinduced metal-to-insulator transition ('photoswitching') in an organic EDO-TTF crystal[12]. The experiment on diarylethene was challenging because of the limited amount of shots that the sample could be exposed to before breakdown. EDO-TTF experiments required the need to perform the experiments at a low repetition rate to prevent accumulative heating (i.e. have enough time from shot to shot to let the sample recover fully) while scattering cross sections of organic components are typically much smaller. These two limitations complicate the weak signals to be strong enough so that they can be detected with appropriate significance. The impressive analysis of the EDO-TTF data has resulted in movies of combinations of bending, sliding and motion molecular modes rather than atom displacements only. Other advancements in the FED field are time resolved molecular movies of samples in gas- or solution phase[13; 14].

Our group is keeping up with these advancements by our current goal to investigate the photo-induced switching of a metal-to-insulator phase transition in the organic crystal Copper-DCNQI. This crystal has the potential to push research in short-time scale dynamics further as, ultimately, physics happening during such phase transitions could in the future possibly be controlled. Because of the complicated molecular character of such crystals, and the ability to make small alterations to such complex organic compounds, one could speculate that time constants of these dynamical transitions could be carefully tuned by altering certain organic compounds.

In this thesis, the reader is provided with an overview of the new Ultra High Vacuum (UHV) chamber for FED-experiments that was developed during the scope of this project. The characteristics of this set-up will be carefully described and compared to our old High Vacuum (HV) set-up that has been operational for six years. This is followed by a short background on the interesting properties of the organic crystals $Cu(DCNQI)_2$ in the third chapter. The relevance of the yet to be performed FED experiments on these crystals is discussed. Results of the cryo-cooled electron diffraction $Cu(DCNQI)_2$ experiments that have already been done in the old HV chamber are summarised. This serves as a justification for why an UHV chamber is needed in our laboratory. The fourth chapter then demonstrates the results of numerical calculations that were performed for optimisation of the newly implemented UHV electron gun. The results of experimental characterisation of the electron pulses that are generated by both the old and the new gun are presented and compared in the fifth chapter. The sixth chapter justifies the benefits of recompression of electron pulses and sheds light on how this can be implemented in the investigation of phase-transition dynamics in our organic crystals. The final chapter summarises the entire MSc project and concludes with a short discussion on the future outlook of this project.

2. An UHV-FED Experimental Set-up

The FED pump-probe technique as described in chapter 1 can be utilised to investigate the type of phase transitions that will be explained in chapter 3. In this chapter the details of the newly built ultra-high vacuum (UHV) FED set-up and its components are discussed. An overview of the set-up, which was built and implemented during this master studies, is given in figure 2.1. It mainly consists of a femtosecond laser, a 150 fs-short laser pulse used as a pump and a sub-ps 30 keV - 50 keV kinetic energy electron pulse used as a probe and the electron detection. These are described in the following. This chapter serves as a general overview of the set-up, whereafter the details of an important part of the set-up — the electron gun — is extensively covered in chapter 4.

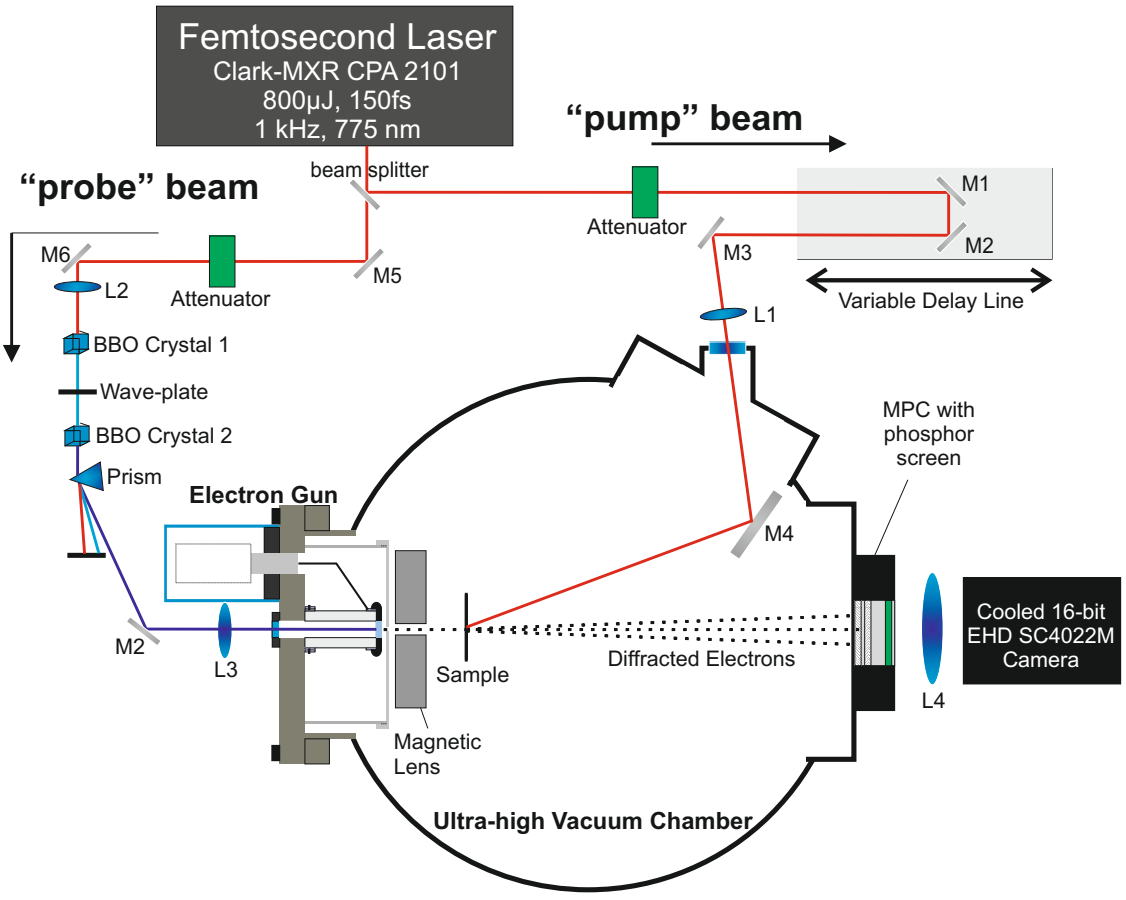

Figure 2.1: Overview of the newly developed UHV FED-setup, capable of doing pump-probe experiments on cryo-cooled temperature controllable samples for acquiring sub-ps time resolution molecular movies. It mainly consists of a pump beam, probe beam and electron detection. Mirrors are labelled 'M' and optical focussing lenses are labelled 'L'.

Within the scope of this MSc, the writer of this thesis also extensively worked with the old high vacuum (HV) FED set-up, so comparisons between the two set-ups are made. Similarities, differences and improvements will be pointed out where this is appropriate. No time-resolved

electron diffraction experiment has been performed with the new UHV FED set-up yet, but it is fit to perform pump-probe electron diffraction experiments.

2.1 Femtosecond Laser System

The FED set-up starts with a femtosecond chirped pulse amplifier laser (*Clark-MXR 2101*), which on itself consists of three lasers. The whole system is manufactured in a temperature controlled two story housing and can be controlled via a computer interface. The first level of the laser houses an Erbium doped fiber ring laser, which produces 1550 nm pulses with a 40 MHz repetition rate. These pulses are stretched; frequency doubled to 775 nm in a BBO crystal and recompressed. The product serves to seed the amplifier on the second level which is a Ti:Sapphire laser cavity. A Nd:YAG laser, also housed on the second level, produces 1064 nm light. Its frequency doubled light pumps this Ti:Sapphire crystal at 532 nm. A Pockels cell (controlled with a high voltage supply and delay timer) placed inside the Ti:Sa cavity controls the number of round trips of the stretched amplified pulse. Before leaving the laser, the output of the Ti:Sa cavity gets recompressed in the final grating compressor. The final output of the entire laser system are pulses with 150 fs duration and 900 µJ pulse energy. These pulses are produced with a repetition rate of 1 kHz and have a central wavelength of 775 nm. We share the total output power of this laser with a group working on femtosecond time resolved absorption spectroscopy. For our experiments, we have a pulse energy of around 250 µJ energy available that we can switch between the old HV and the new UHV system.

2.2 Pump Beam

It was mentioned in chapter 1 that both pump and probe beam come from the same laser source in order to achieve optimum synchronisation between pump and probe. In this manner, the delay between the arrival time for both pump and probe pulses are correlated from pulse to pulse. The laser output beam is split into the pump and probe path with a 50/50 beamsplitter[1]. In the apple-bullet analogy of this experiment, the impact time of the bullet on the apple is comparatively short, meaning that the 'pump' time of the apple is a well-defined point in time. In the case of FED, this is done by illuminating the short (focussed) laser pulses onto the sample. In our case, this can be done by using the fundamental 775 nm beam as it is. However, if due to the absorption characteristics of the sample a different wavelength is required, the fundamental beam can be substituted by the output of a noncollinear optical parametric amplifier (NOPA) with tuneable wavelength.

In order to acquire a molecular movie over a long time scale, the arrival between the pump and the taking of the snapshot (probe — as will be discussed in section 2.3) needs to meet the following criteria:

- Firstly, the arrival time of both pump and probe pulses needs to be calibrated such that they arrive at the same time ($t = t_0$),
- After calibration, the delay between pump and probe arrival needs to be tuneable. By 'stitching' together snapshots of the sample for a range of pump and probe arrival time delays, a full molecular movie can be acquired.

In chapter 5, the initial $t = t_0$ alignment of the delay stage will be explained. Tuning of the pump-probe arrival time is done by introducing a mechanical delay stage (labelled as 'variable

[1]Pump power can be easily increased by changing the beamsplitter, allowing the pump path to receive more energy.

delay line' in figure 2.1). An extra pathlength through air of 30 µm — which means a shift of 15 µm of the delay stage — corresponds to a delay of 100 fs. Numbers like these are easily achieved with commercial mechanical translation stages, such as the *Standa* stage used in our pump path. It is important to note that the speed of the electron probe beam varies from v = 0.33c – 0.40c for electron kinetic energies of 30 – 50 keV. This means that for temporal overlap, the geometrical probe beam path is longer than the pump beam path.

Fluence of the pump pulses that excite the sample under investigation needs to be carefully controlled. Exposing delicate samples to too high fluences will destroy them (around $>$ 3 mJ/cm^2 for TaS_2). Low fluences might not initiate any phase transition at all (around $<$ 0.5 mJ/cm^2 for TaS_2). In some samples, different fluences can initiate different phase transitions as we have seen in our experiments[8], making controllability of the pump fluence even more crucial. Another argument for accurate fluence tunability is that one controversy that has been under investigation is which mechanisms are accountable for the processes driving a CDW formation and destruction. By performing fluence dependent FED measurements and determining the amount of energy needed to induce such a phase transition, hints of which one of the following processes is happening can be revealed[9]:

- A phase transition can be purely thermodynamically driven (the energy given to the electrons by the pump pulse is converted so that a lattice equilibrium is obtained).
- Only selected degrees of freedom, like electrons or particular phonons, are responsible for the phase transition.

For the first scenario, the pump energy required to induce a phase transition would have to equal the energy needed to heat the sample to above the phase transition temperature. For the second scenario, less energy would be sufficient. To find out which statement is true, pump fluence needs to be carefully controllable.

To be able to do such accurately determined fluence experiments, the pulse energy and the area of the incident beam to the sample needs to be measured. The first can easily be determined by temporary inserting a power meter in the laser beam path, allowing us to choose the pump beam power carefully by tuning the filter wheel (labelled 'Attenuator' on the left of figure 2.1). Pulse energy can then be easily calculated using the following formula:

$$E_{pulse} = \frac{P_{average}}{PRR} \tag{2.2.1}$$

where E_{pulse} is the pulse energy, $P_{average}$ the average power and PRR the pulse repetition rate.

The spotsize of the incident pump beam at sample position is reduced by a focussing lens (labelled 'L1' in figure 2.1) that is placed outside the vacuum. The spotsize at sample position can be carefully estimated by inserting a flip mirror after the focussing lens, to direct the light onto a CCD camera. The pathlength from the focussing lens to the camera should be equal to the pathlength from the lens to the sample. Dependence of the spotsize on the sample position can be investigated by putting the camera on a translation stage, allowing to determine spotsize for a certain range. We have decided that the spotsize will have to be at least around five times as big as the sample[2] when the sample gets excited, so that the entire sample area gets illuminated (and hopefully thus photoexcited) in a homogeneous manner. By varying the lens position, the spotsize at sample position can be controlled. An idea of what that spotsize typically is, is obtained with the following calculation: in case of an ideal Gaussian beam, the angular spread is given by[15]:

[2]Samples typically have a diameter of 50 – 200 µm.

$$\theta = \frac{\lambda}{\pi w_0}. \tag{2.2.2}$$

Where λ is the wavelength of the laserlight and w_0 the minimum FWHM beam waist of the beam. In our case, lens 'L1' is a 1000 mm focussing lens. With our laser spotsize being around 5 mm (corresponding to a beam waist of 2.5 mm) this leads to an angular spread of arctan[(2.5 mm)/(1000 mm)] = 0.0025 rad. In the case of λ = 775 nm laserlight, this corresponds to a minimum beam waist of (775 nm)/($\pi\cdot$ 0.0025 rad) = 100 µm according to equation 2.2.2. The Rayleigh length for this focus is given by[15]:

$$Z_R = \frac{\pi w_0^2}{\lambda} = \frac{\lambda}{\pi\theta^2}, \tag{2.2.3}$$

The Rayleigh length is ($775\cdot10^{-9}$ nm)/($\pi\cdot$[0.0025 rad]^2) = 39 mm for lens 'L1' with f = 1000 mm and λ = 775 nm. The beam waist profile of a perfect Gaussian beam is given by:

$$w^2(z) = w_0^2\left(1 + \frac{z^2}{z_R^2}\right) \tag{2.2.4}$$

Where w is the beam waist as function of distance z, w_0 the beam waist at the focus (100 µm) and z_R the Rayleigh length (39 mm). The analytical perfect Gaussian beam profile for our pump beam is plotted in figure 2.2.

Accurately placing the CCD camera at the same pathlength distance from the flip mirror is not something that can be done precisely, meaning that we have to accept that there is an error in the spotsize. Fortunately having a long Rayleigh length of 39 mm makes the spotsize less sensitive to the position. Knowing the beam waist parameters of the pump beam has the advantage that the spotsize at sample position can be easily tuned by simply moving the lens. If, however, for whatever reason, we believe that we need to know the spotsize more accurately, the focussing lens 'L1' could be replaced with a spotsize reducer. The output of such a reducer is a collimated beam with a smaller, known, spotsize (that is not tuneable).

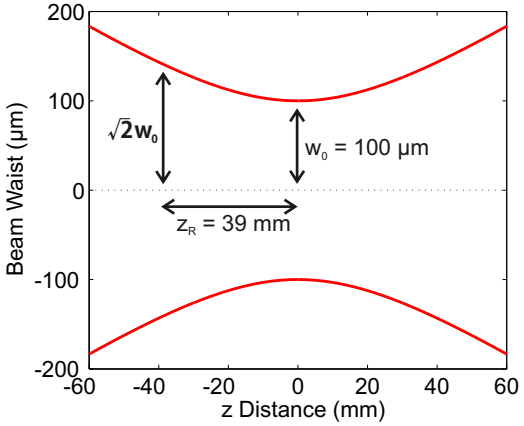

Figure 2.2: The FWHM spotsize of the focussing pump beam plotted as a function of distance, based on the ideal Gaussian beam profile (equation 2.2.4).

This UHV set-up pump beam path is not much different than the one in the old HV set-up, of which a detailed description is available in Chapter 3.2 of ref. [16]. In the old set-up, a rotatable half wave-plate and polariser combination attenuates the beam, whereas in the new case a neutral density filter is used. However, we have a half wave-plate and polariser to our direct availability if it turns out to be advantageous.

To summarise section 2.2 with our first macroscopic analogy: The details of the bullet that will be shot through the apple have been explained. To continue the chapter, the details of the stroboscope flash that probes the dynamics initiated by the bullet will be explained.

2.3 Probe Beam

As mentioned our probe 'flash' needs to be able to resolve atomic structures and the exposure time of the atomic snapshots needs to be short to achieve high temporal resolution. To do so, we employ a 30 – 50 keV electron pulse. The pulsed electron beam needs to meet the following conditions:

- The effective de Broglie wavelength has to be sufficiently small($\lambda \leq 2d$, where d in this case is the lattice constant of the crystal under investigation) so that we are not diffraction limited,
- The transverse coherence has to be at least a few d so that diffraction peaks can be resolved,
- The pulse has to be shorter than a picosecond for sufficiently low temporal resolution of our atomic movie.

The theory of electron diffraction has already been explained in a number of books, so the reader is referred to for example reference [17] for the fundamentals of electron diffraction. Most relevant principles are highlighted below.

In chapter 1 it was discussed that crystals under investigation have lattice constants in the Angström regime. Braggs law teaches us that if spacing between such crystal planes is d, and if these planes are ordered in a periodic structure, then under irradiation of a coherent wave front, constructive interference of the radiation from crystal planes occurs when the path difference is an integral number n of wavelengths λ, so that

$$2d \sin\theta = n\lambda. \tag{2.3.1}$$

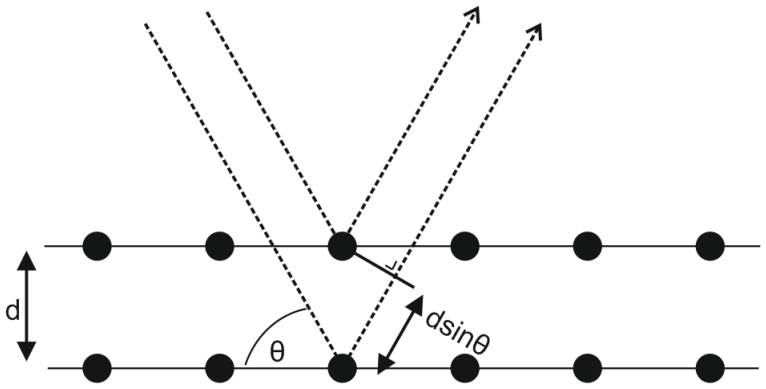

Figure 2.3: Bragg diffraction. When two beams (same λ and same phase) are scattered off two different crystal planes, then in this case the lower beam travels an extra pathlength of $2d\sin\theta$. For constructive interference, this length must equal an integer multiple of the wavelength of the incoming beams (equation 2.3.1).

This law is also shown in figure 2.3 and is satisfied only for wavelength $\lambda \leq 2d$, a condition that can't be satisfied with visible laser light. When the condition is satisfied, the resultant diffracted constructive interference beams form a diffraction pattern which reveals the atomic structure of the crystal under irradiation. With regard to the three conditions mentioned in the bullet points above, in chapter 5 it will be shown that the requirements for the transverse coherence and pulse duration are met for 30 – 50 keV kinetic energy electron pulses. To

determine the effective wavelength mentioned in the first point, one can simply fill out the formula for the de Broglie wavelength (which holds because we are working with non-relativistic electrons):

$$\lambda = \frac{\mathrm{h}}{\sqrt{2\mathrm{m}_e E_k}} \tag{2.3.2}$$

Where h is Plancks' constant, m_e the rest mass of an electron and E_k the kinetic energy of the electron, given by

$$E_k = \frac{1}{2}\mathrm{m}_e v^2. \tag{2.3.3}$$

In our case, we work with electron energies of 30 – 50 keV which corresponds to an effective wavelength of 0.071 – 0.055 Å, which is sufficient for lattice constants in the Angström regime. In our set-up, Bragg diffraction in transmission is done rather than diffraction in reflection.

2.3.1 Frequency Tripled Light Generation

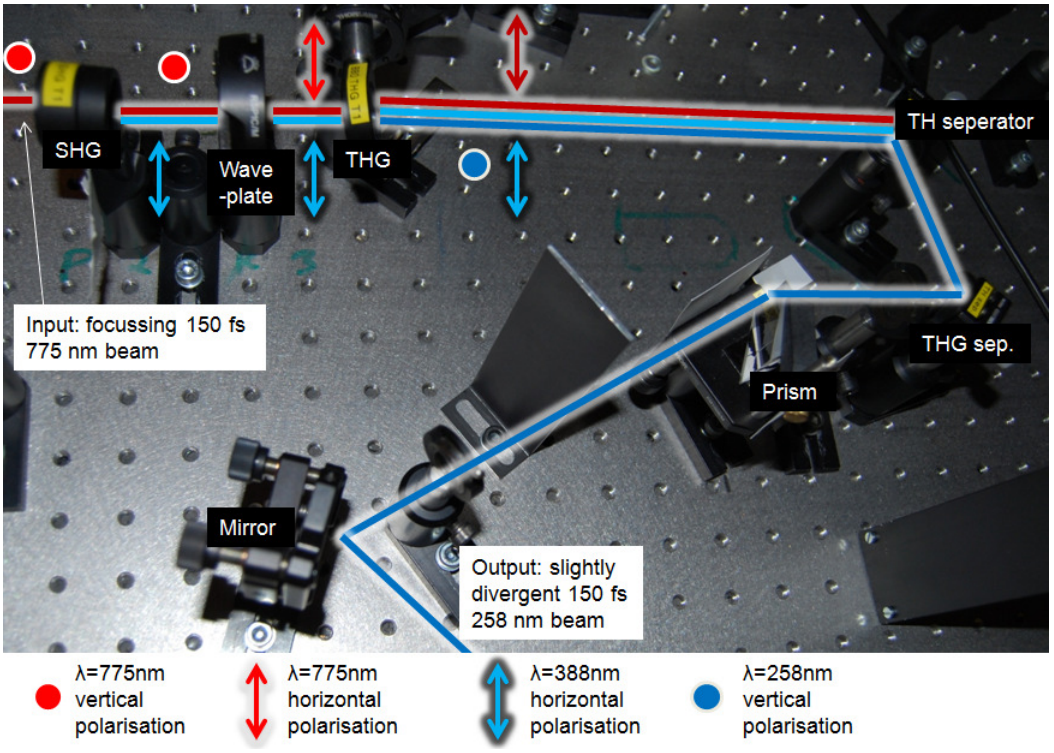

Figure 2.4: Experimental set-up for third harmonic generation ($\lambda = 258$ nm) of the fundamental laser light ($\lambda = 775$ nm). The generated 3rd harmonic beam serves as an input for pulsed electron beam generation.

In order to generate electron pulses, as will be explained in section 2.3.2, frequency tripled light is desirable over the fundamental light due to its higher photon energy. The photon energy 1.60 eV of the fundamental light is not sufficient for the single photon excitation process for electron pulse generation. The frequency tripled photon energy of 4.81 eV is preferred. The tripling is done by a basic femtokit (FK series) from Eksma optics. A photo of the implemented set-up is shown in figure 2.4. The frequency tripling is produced by the

optical elements labelled 'L2', 'BBO Crystal 1', 'Wave-plate', 'BBO Crystal 2' and 'Prism' in figure 2.1. The set-up mainly consists of two beta barium borate (BBO) crystals, the first one being a type 1 second harmonic generation (SHG) BBO crystal with a 6x6mm aperture, P-coated at 400-800nm. Lens 'L2' focusses the vertically polarised 775 nm light such that enough intensity for the nonlinear processes to happen is achieved. A zero order dual wave-plate after the first crystal flips the horizontal polarisation of the SHG light to vertical polarisation, while maintaining the fundamentals' vertical polarisation. This is necessary so that phase matching conditions in the second crystal are met, which is a type 1 third harmonic generation (THG) BBO crystal with a 6x6 mm aperture, P-coated at 400-800/266 nm.

The output of the second crystal is a beam that contains the SHG, THG, as well as the fundamental light. The fundamental and SHG light are filtered out by means of two SHG separators and a prism. The output of this experimental set-up is a purely 258 nm beam, which is divergent (angular spread of 0.0033 rad) due to the 750 mm focal length focussing lens (labelled 'L2' in fig. 2.1) placed before the frequency tripling set-up. This beam, of which the spectrum is shown in figure 2.5, serves as the input for the electron beam generation.

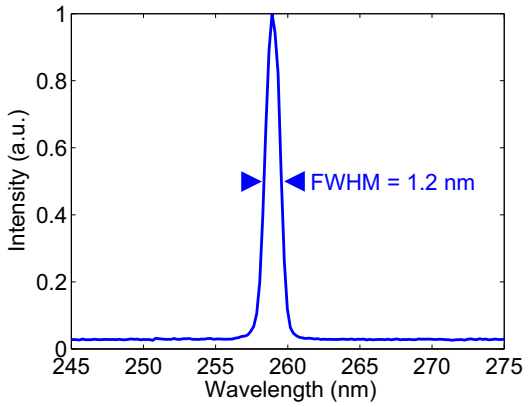

Figure 2.5: Spectrum of the output of the 3rd harmonic generation set-up.

2.3.2 Pulsed Electron Beam Generation

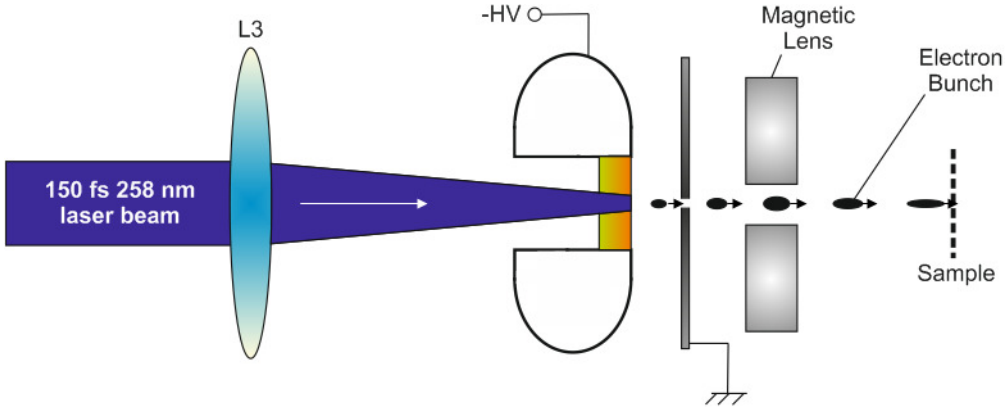

Figure 2.6: Conceptual sketch of the working of an electron gun. The 3rd harmonic pulsed laser beam is converted into a focussing pulsed electron beam by means of a cathode-anode configuration and a magnetic lens.

The working of an electron gun is explained through the conceptional sketch in figure 2.6. The third harmonic light is focussed by a lens (labelled 'L3' in both figures 2.1 and 2.6) onto a cathode that is applied to a high negative voltage. The cathode consists of a window with a 10 nm thin semi-transparent gold layer sputtered onto it (produced for us by Ray Meng Gao from the University of Toronto). The photon energy of 4.83 eV is sufficient to generate free

electrons from gold by employing the photoelectric effect[18; 19]. Advantage of using UV light (that overlaps with the work function of the cathode) are that the electron beam intensity is very stable. Furthermore, the bandwidth ΔE of the electron beam is kept to a minimum. 10 nm of gold is almost transparent for the 258 nm laser pulse, which means that photo-electrons are generated along the entire 10 nm path. However, due to the low initial kinetic energy of the electrons ($h\nu_{photon}$ - $E_{workfunction} \ll 1$ eV), electrons in the gold volume do not reach the back surface of the gold layer. Only electrons from the gold surface contribute to the accelerated pulse. This means that the initial electron pulse duration is the same as the UV pulse duration (150 fs). However, pulse duration increases as a function of the travelling distance through the vacuum of the electrons (due to Coulomb repulsion within such an electron pulse and the initial energy spread ΔE)[20]. A detailed discussion of this undesirable effect, that increases the temporal duration of the 'snapshots' that are being taken by the electron probe beam and thus worsens the temporal resolution of diffraction patterns, is covered in chapter 4. After the generation of electrons, they accelerate in a strong (10 MV/m) electric field towards the grounded anode and are focussed through the sample onto the detector by a magnetic lens[3]. In this manner, sharp diffraction peaks that are generated in transmission are focussed onto the detector, revealing the atomic structure of the sample under investigation.

To conceptually simplify the probe, let us go back to the bullet through an apple analogy: we have now explained the details of the flash that was used to take a snapshot of the apple. However, in this case the snapshot has atomic precision and sub-picosecond temporal resolution. In chapter 4, the redesign of the electron gun will be discussed.

Shown in figure 2.7a is a cross-sectional view of the design of the electron gun that is employed in the old HV chamber. The anode and cathode set-up as illustrated in figure 2.6 are clearly visible. For this design, it was chosen to electronically decouple the cathode on high voltage from the grounded chamber with an insulating macor tube of 25 cm. This was done to exclude the possibility of arcing. However, specifications indicate that the macor material has an insulation constant of 10 kV/cm, meaning that for a high voltage of 50kV a tube of 5 cm can be afforded. This gives a new design the potential to be significantly smaller. On the main tube of the old electron gun, which has a diameter of 100 mm, an extra tube with a diameter of 45 mm is welded at an angle of 30° so that the high voltage feedthrough can reach the cathode. This makes assembly and disassembly of this gun a mission, as explained in the appendix of ref. [22].

The design for the new electron gun on our new chamber is shown in figure 2.7b;c. Two primary considerations for the new electron gun are that the design has to be as compact as possible, and the assembly and disassembly of the gun should be easier than for the old gun. Instead of having a 100 mm flange size on the chamber we now chose for a 200 mm diameter sized flange on the chamber for the electron gun. The big advantage of having a bigger flange is that now both the high voltage- and the laser feedthrough are mounted on the front flange. This means that for the new gun, a second tube welded onto the main tube of the electron gun is no longer needed. This makes assembly and disassembly a lot easier as all the parts are accessible by simply removing the front flange. In figure 2.8 photographs of the old and the new gun are displayed. By looking at the photo of figure 2.8c it is obvious that all elements of the new gun are directly accessible.

[3]For a detailed description of the magnetic lens, I refer to section 3.1: magnetic lens in [16], section 1.2: magnetic lens in [21], section 4.4 in [22] and section 4.3.1 in [23].

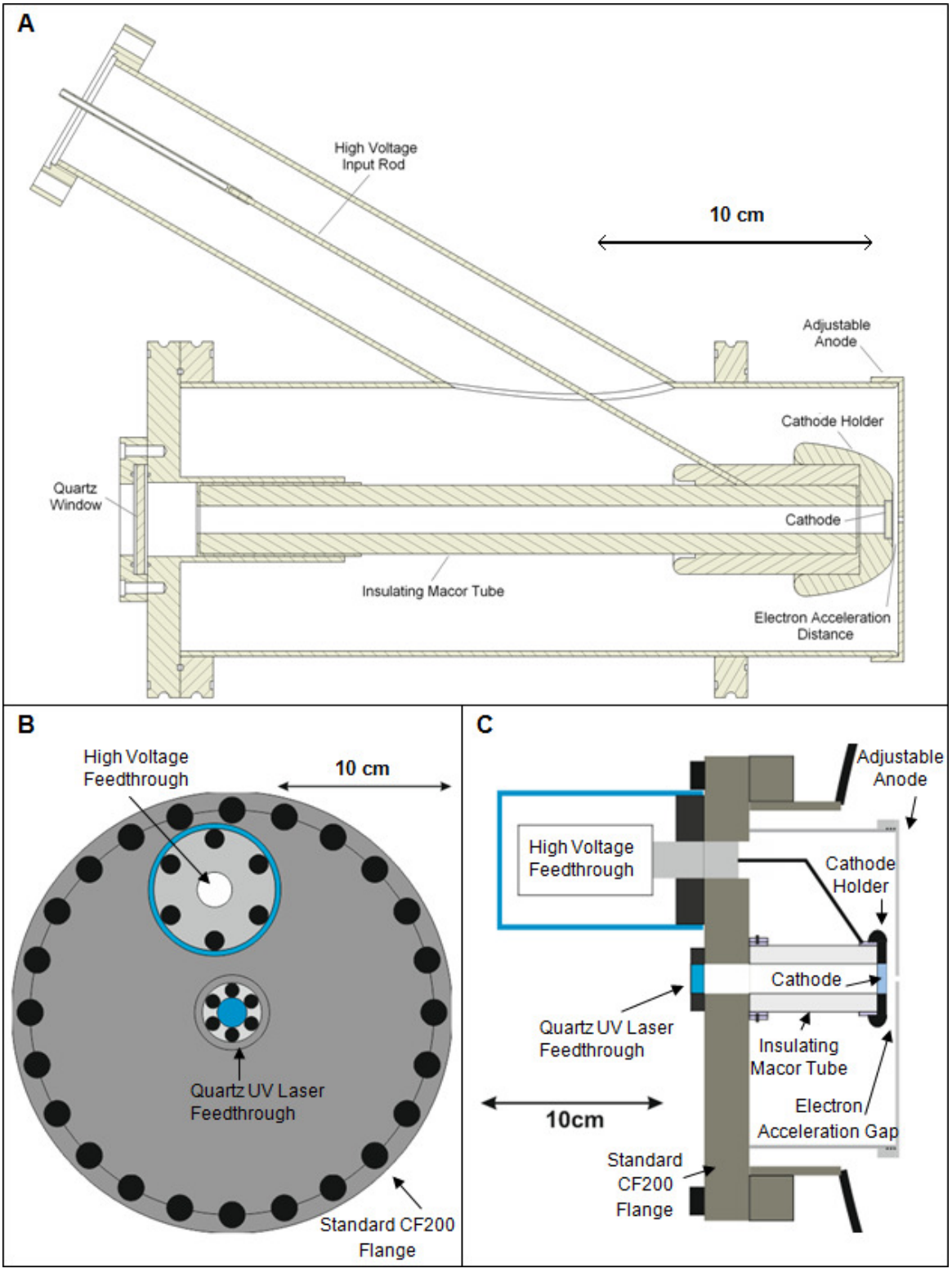

Figure 2.7: (a) Cross-sectional drawing of the electron gun as implemented in the old high vacuum FED set-up. (b) Front view of the electron gun design for the new UHV electron gun. (c) Cross-sectional drawing of the new UHV electron gun.

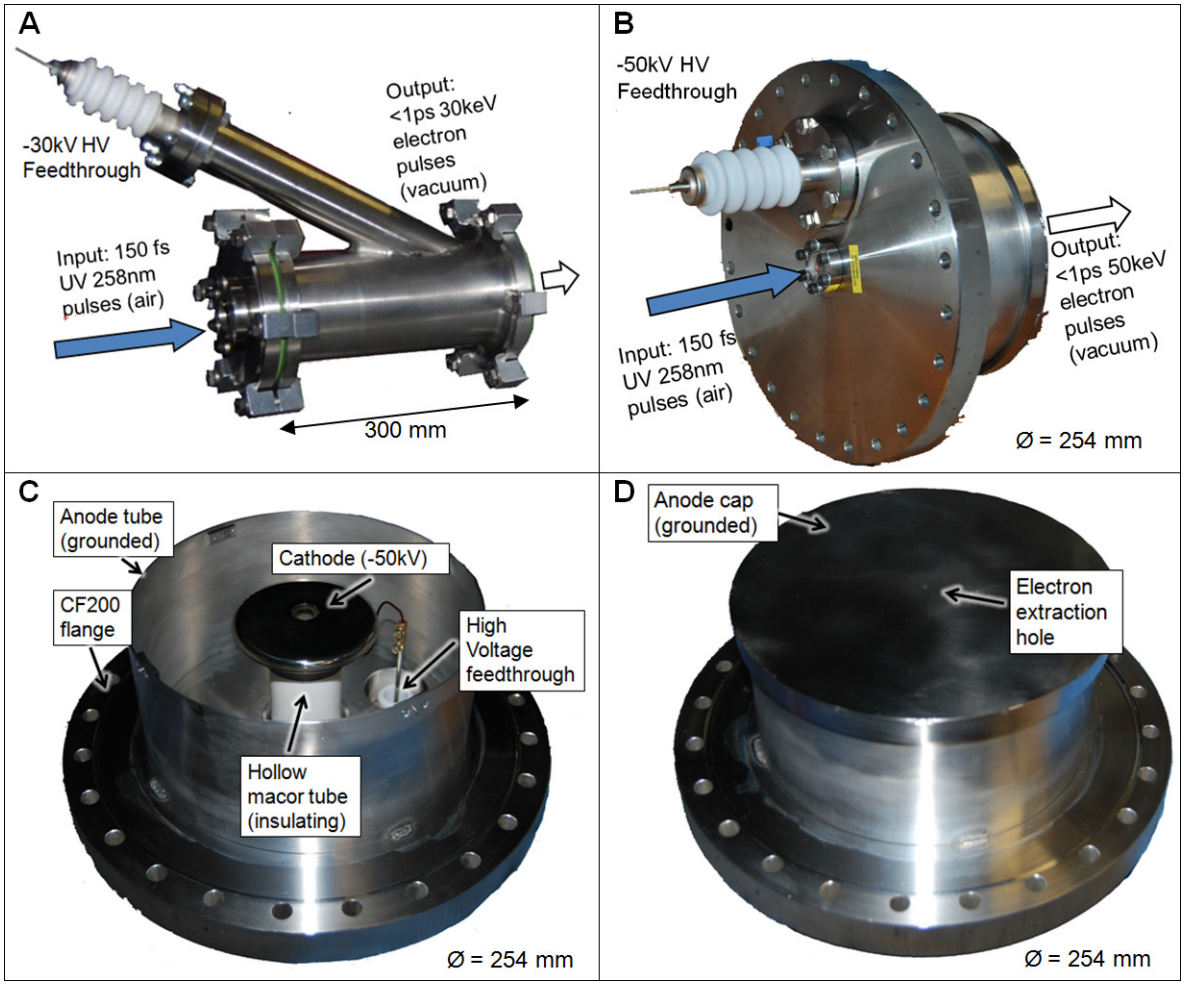

Figure 2.8: (a) Photograph of the old HV electron gun. (b) Photograph of the new UHV electron gun. (c) Photograph of the UHV electron gun with the anode cap removed. (d) Photograph of UHV electron gun with the anode cap mounted.

2.3.3 Detection of Electron Diffraction Patterns

The final element in the probe beam is the detection system which is a double Chevron Micro Channel Plate (MCP) and phosphor screen combination, situated around 50 cm behind the magnetic lens. This commercially purchased *BOS-50 Beam Observation System* from *Beam Imaging Solutions* works the same as the detection system in the old HV system: it converts the incident beam of electrons into an image that is visible through the glass viewport. The main aspects of the working of the detection system (labelled 'MCP with phosphor screen', 'L4' and 'Cooled 16-bit EHD SC4022M Camera' in figure 2.1) are summarised in this section.

MCP's are electron signal multipliers. The MCPs consist of hexagonally arranged circular capillaries (60% open-area-ratio) with metal oxide coated inner walls. The coated capillaries generate secondary electrons when they are struck by a charged particle or a photon. Our model has a 40 mm diameter active area MCP. To allow incoming particles to hit the walls in the capillaries, the two MCP plates are not mounted parallel with the incoming electron beam, but they are slightly slanted. The two plates are also slanted compared to each other for double gain (called Chevron stacking configuration). The electron snowball effect generated

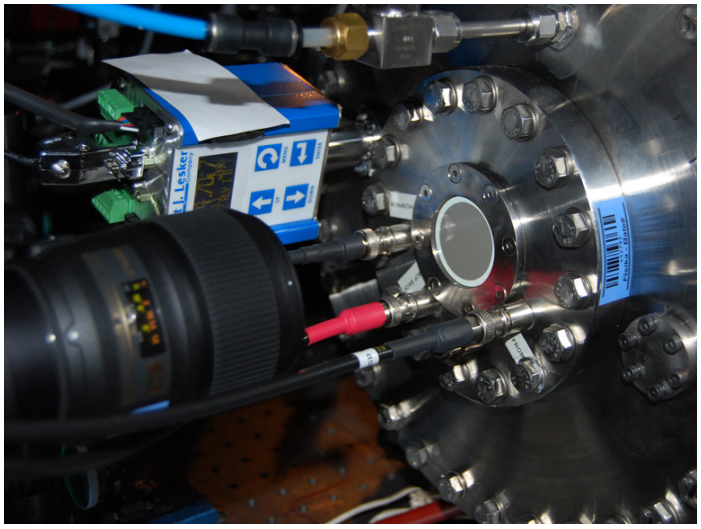

Figure 2.9: The electron signal output from the MCP and phosphor screen is observed from a glass window, visible on the right. This is detected by a 16-bit CCD camera with a lens mounted onto it, visible on the left. In the background, the gauge for monitoring pressure in the chamber is visible.

in the MCP plates results in an amplification of $> 10^8$. The detection system on the old HV chamber (commercially purchased from *'Tectra Physikalische Instrumente'*), which is an almost identical system, specifies amplification of $> 5 \times 10^6$. The electron signal is amplified by the MCPs by applying 1000 V across each MCP plate (2000 V across both plates). A voltage of +5000 V is applied to an aluminised phosphor screen which is uniformly deposited onto a glass plate. The electrons, now carrying 5000 eV kinetic energy, have enough energy to photoexcite the P-43 phosphor screen. Conversion efficiency from electron to photon is specified as $\eta = 0.063$ photons/eV/electron, with the system being sensitive for an electron beam energy range of 1 – 50 keV. Light emitted by the photoexcited phosphor ($\lambda = 560$ nm) is focussed by a commercial *Nikon AF-S Micro* 60 mm f/2.8 macro lens (labelled 'L4' in figure 2.1) onto a cooled 16-bit *EHD SC4022M* camera (15 mm by 15 mm CCD chip, corresponding to 2048 px by 2048 px) that is capturing the electron diffraction patterns. The entire MCP-phosphor assembly (figure 2.9) is housed within a CF100 flange with a glass viewport. The assembly is mounted onto a CF250 flange which has the advantage that an extension or contraction of the detection system can be implemented, allowing us to alter the magnetic lens to detector distance whenever we wish to do so.

2.4 The UHV Chamber

FED needs to be performed in a vacuum chamber for three reasons:

- Firstly, a vacuum is needed for electron propagation. The mean pathlength of electrons in a gas is given by:

$$L = \frac{\mathrm{k}T}{4\pi\sqrt{2}r^2p} \tag{2.4.1}$$

where k is the Boltzmann constant ($1.38 \cdot 10^{-23}$ $\mathrm{m^2kg\ s^{-2}K^{-1}}$), T the temperature, r the radius of the gas molecules (155 pm for N_2) and the p pressure of the gas. For room temperature and atmospheric pressure, the mean pathlength is only in the order

of 100 nm, which makes atmospheric pressure unsuitable for FED. For a pressure of 10^{-8} mbar, the mean pathlength of an electron is in the order of 10 km.

- Secondly, the electron gun generates high electric fields between the cathode and anode. Having gas in the gun fosters electric break down. Paschen's law is an equation for breakdown voltage as a function of pressure for a specified separation of objects:

$$V = \frac{\mathrm{B}pd}{\ln(\mathrm{A}pd) + \mathrm{C}}, \tag{2.4.2}$$

where V is the applied voltage, p the pressure (in Pascal), d the cathode-to-anode separation (5 mm in our case) and A, B and C are constants (1 $(atm{\cdot}m)^{-1}$, $4.36{\cdot}10^7 V/(atm{\cdot}m)$ and 12.8 [dimensionless] respectively). This is a rule of thumb that is not particularly accurate, especially not for the low p and d that it is applied for in this case. Nevertheless, the breakdown voltage according to equation 2.4.2 at 1 atm is 30 kV. Both high and low pressures are suppressing electric break down. The lowest breakdown voltage is at $1.5{\cdot}10^{-3}$ mbar: 327 V. At a pressure of $5{\cdot}10^{-4}$ mbar the breakdown voltage is 50 kV (the voltage that we apply to our cathode), which is still well above the pressures we work with.

- Lastly, as will be experimentally shown in chapter 3, when samples are cooled down to low temperatures, condensation of matter will occur onto the sample surface (boiling point of water and nitrogen are 273 K and 77 K respectively, eventually worsening the diffraction signal). In the field of UHV surface physics, a unit to study the adsorption of gasses onto surfaces is the 'Langmuir' (symbol: L). One Langmuir correlates to an exposure of 10^{-6} Torr for one second. When a sticking coefficient for a surface of 1.00 is assumed (that means, every gas molecule that hits the surface sticks to it), 1 L results in the surface being covered in a monolayer of the molecules of the absorbed gas. Under the assumption of a sample sticking coefficient of 1.00, the sample in our HV chamber absorbs a monolayer in 3 seconds for $p = 5{\cdot}10^{-7}$ mbar. For an UHV ($p = 1{\cdot}10^{-9}$ mbar this corresponds to 23 minutes. Clearly, employing low pressures prevents condensation of gasses onto the sample surface.

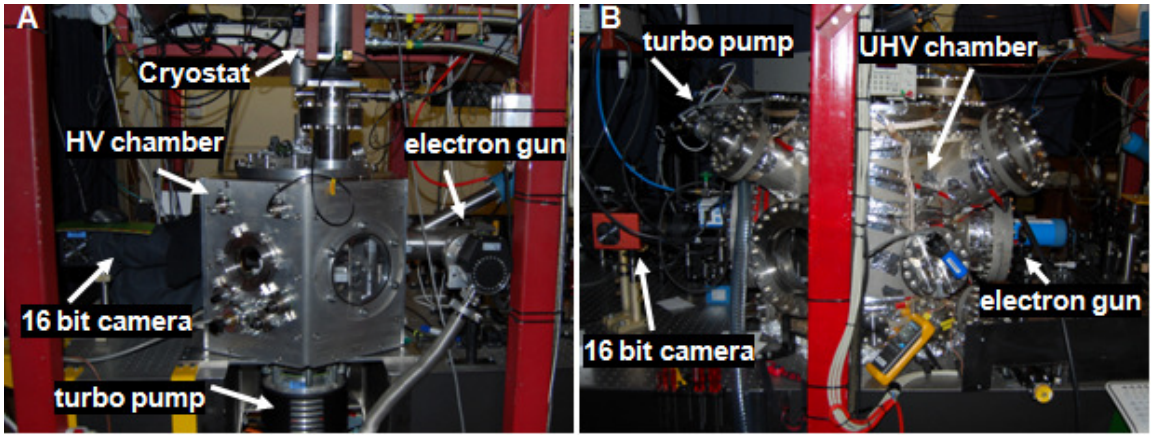

Figure 2.10: (a) Photograph of the old HV chamber. (b) Photograph of the new UHV chamber.

The old vacuum chamber (fig. 2.10a) has been operational for six years and the successful experiments performed by our group, that were mentioned in the introduction, were performed

in this chamber. The pressure of this Aluminium chamber is not exceptionally low for an FED set-up (pressures of around $1.7 \cdot 10^{-7}$ mbar are reached after long periods of baking and pumping). This pressure is achieved by pumping the chamber with a rotary vane 'rough' pump (*Adixen 2015SD* with a pumping capacity of 15 m^3/h) and a turbo pump (*Leybold TW70H* with a pumping capacity of 700 ℓ/s). When developing the old chamber, it was decided to pay the price for having 'bad' pressure because the chamber was designed to be as flexible as possible. It consists of a hexagonal stainless steel frame with 50 cm diameter. All Aluminium walls that are fitted with rubber O-rings are easy and quick to interchange, making it a perfect chamber to start off with.

The three reasons mentioned above to have a vacuum are not detrimental for the executed experiments in the old HV chamber. The conditions for the mean free pathlength of the electron and the breakdown voltage for the gun are met for the pressures achieved with the old HV chamber. With regard to the condensation problem in the HV chamber: the lowest temperature to which a sample was cooled in this chamber for a successful experiment was 180 K. A sticking coefficient of 1.00 of the sample is not a reasonable assumption for such a 'high' sample temperature, so absorption times of a monolayer onto the sample are much longer.

2.4.1 Technical Details of the UHV Chamber

In chapter 3 it will be shown that we can no longer afford the price of 'bad' pressure for this flexibility due to condensation onto the sample. Therefore, an Ultrahigh Vacuum chamber (pressures below $1 \cdot 10^{-8}$ mbar) was designed[4] and built in our departmental workshop facility[5] (figure 2.10b). All seals are now Copper Flanged (CF) seals instead of rubber O-rings. CF-seals have higher vacuum specifications: the faces of the two surfaces that the copper seal will connect have a knife edge. This edge cuts into the softer copper when the two surfaces are tightened towards each other by the screws and bolts (figure 2.11). This results in a leak-tight, metal-to-metal seal. Two pumps on the main chamber are pumping the vacuum: a *Vacutec Agilent SH-110* rough pump (pumping capacity of 110 ℓ/min) and an *Agilent Turbo-V 301* pump (pumping capacity of 300 ℓ/s). The pressure is monitored by a *Lesker KJL275256* and *KJLC392402YE* gauge combination with a total measuring range of $1{\cdot}10^{-9}$ mbar – 1 atm. To this date, the best pressure after baking and leak-testing achieved is around $5 \cdot 10^{-8}$ mbar. Recently, three MICOS translation stages for three-dimensional sample positioning and alignment have been installed in the vacuum. These threaded stages are specified for a vacuum down to $1 \cdot 10^{-9}$ mbar, but have a high surface area. It is expected that that after longer periods of baking (which enhances outgassing) the pressure will still improve. Secondly, our home-built magnetic lens was sealed to be air-tight, so that the massive surface area of the large number of coils that the lens consists of doesn't outgas into our vacuum. However, running a current through this coil (Power $\approx$ 1 W) increases the pressure with almost an order of magnitude. Resealing the airtight housing of this coil is expected to reduce outgassing from the coil. For these two reasons, we have an informed hope that after more baking and leak-testing endeavours pressures of well below $1 \cdot 10^{-8}$ mbar are achievable.

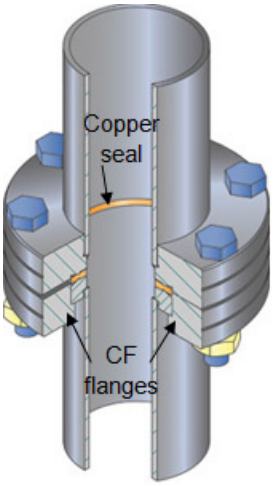

Figure 2.11: A CF flange and copper seal assembly

[4]Design thanks to Prof. H. Schwoerer.

[5]Vacuum chamber built and tested by Lawrence Ashworth.

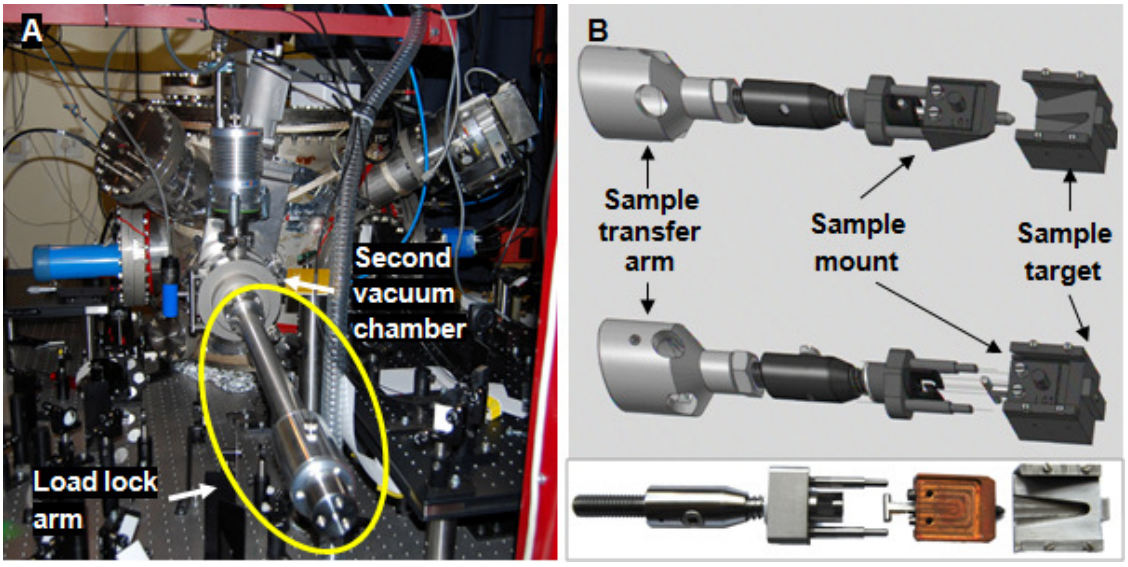

Figure 2.12: (a) Load lock arm and second vacuum chamber mounted onto the main vacuum chamber. (b) Exploded view and photograph of the transfer mount system, capable of exchanging samples without having to break the vacuum. Drawing made available by Tim Riedel from the University of Kiel.

2.4.2 Load Lock System

In the old HV chamber, it takes several hours to reach a pressure in the 10^{-5} mbar regime after having broken the vacuum and switching on the pumps again. Experiments can't be performed at higher pressures as this is the maximal operational pressure for the MCP-phosphor detection system. Practically, this means that after sample exchange no experiments can be performed on the same day, resulting in inconvenient and long delays. Furthermore, after sample exchange, the alignment of the sample onto the electron beam is usually lost. In the new UHV chamber, this has been dramatically improved by the implementation of a load lock system and transfer mount combination for sample exchange as depicted in figure 2.12. The load lock system consists of a second vacuum chamber, pumped down by an *Agilent IDP-2* rough pump (pumping capacity of 35 ℓ/min) and an *Axiden MDP5011 turbo pump* (pumping capacity of 7.5 ℓ/s), with the pressure being monitored by a *Lesker KJL275* gauge (measuring range of 10^{-4} mbar to 1.333 mbar). This second vacuum chamber is connected to the main chamber with a valve. When this valve is opened, the load lock arm can slide inwards and enter the main vacuum. Connected to this load lock arm is a transfer mount system[6] (figure 2.12b). Onto this transfer arm, a sample mount can be mounted or removed from a transfer target mount in the vacuum chamber.

The procedure to exchange a sample is as following:

- The second small load lock chamber is evacuated. After achieving a pressure of below 10^{-5} mbar, the valve is opened and the load lock arm is slid into the main chamber, such that it approaches the sample mount that is fixed to the target mount.
- The target mount, with the samples attached, is positioned in front of the transfer arm with the *MICOS* UHV stages.

[6]Design and availability of drawing thanks to Tim Riedel and Dr. Kai Rossnagel, physical copy of this design thanks to Lawrence Ashworth.

- The sample mount is unscrewed, slid back into the second load lock vacuum chamber, and the valve is closed.
- The second vacuum chamber is devacuated, the sample on the sample mount is interchanged and the second small vacuum chamber is evacuated again.
- After having reached a reasonable pressure of $< 10^{-5}$ mbar, the valve is reopened, the transfer arm with sample mount is slided into the main vacuum onto the transfer mount after which the sample is reattached onto the mount.
- Final step in the procedure is to again remove the transfer arm from the main vacuum and close the valve.

This whole procedure of sample exchange can be done in half an hour. This makes sample exchange and acquiring diffraction patterns on a whole range of samples within one day much more practical and efficient. But the most important improvement is that the vacuum doesn't have to be broken. Devacuating a UHV is detrimental for its pressure, as water and other molecules can enter the chamber and condensate onto the chamber walls or objects installed in the chamber.

2.4.3 Closed Cycle Cryostat System

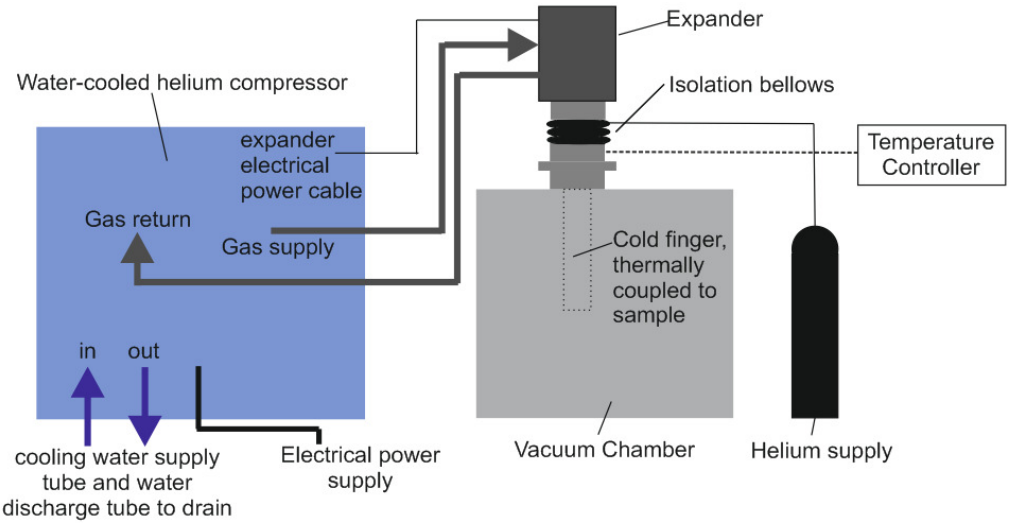

Figure 2.13: Sketch of the closed loop cryostat system capable of cooling samples to cryogenic temperatures, displaying how different compounds are connected.

In order to access the low phase transition temperatures (< 60 K) of the samples that are to be investigated in our FED set-up, a cryostat system (*Advanced Research Systems, Inc.* Expander model *DMX/GMX20*) connected to a compressor (model *ARS-4HW*) will be mounted on top of our new UHV chamber. The cryostat set-up is displayed in figure 2.13. This cryostat system was already used in the preliminary results that will be presented in chapter 3 and is currently (September 2014) still mounted onto the old HV chamber but will be transferred to the new UHV chamber this year still. The cylinder assembly, visibly mounted on the old HV chamber in figure 2.10a, has a cold finger inside the vacuum chamber that is thermally attached to a sample with a copper braid, which allows to control the sample temperature. A radiant heat shield is attached to the cold finger to minimise heating up of the cold finger.

The base of the cold finger can cool down to 10 K in less than 110 minutes, with an overall operating range of $<8 - 355$ K with a stability of 0.1 K. Desired temperature and cooling rate can be set with the temperature controller that is coupled to the cryostat and calibrated with a sensor at the cold finger tip as well as the sample. Practically, we have reached cold finger temperatures of 16 K and sample temperatures of 32 K due to the copper braid that makes the thermal connection between the cold finger and the sample. This braid is not being shielded from radiation. The high surface area of the braid makes it a good heat absorber. Using a copper braid of around 10 cm is inevitable as the sample needs to be able to move through the vacuum with the *MICOS* stages that it is mounted on.

The compressor works on the principle of the Gifford-McMahon refrigeration cycle. The compressor supplies electrical power to the expander. It also supplies the helium gas flow rate (on high pressure) that the expander converts into the desired refrigeration capacity. The compressor itself is cooled with cooling water. The inflow of high pressure and outflow of low pressure is driven by a motor turning a valve disk in the expander. The timing of the repetitive pumping cycle is done by opening and closing of the valve with a displacer that responds to the cyclical changes in gas pressure. When the gas reaches the lower portion of the expander, it is vented to the low-pressure return out of the valve motor base and back to the compressor.

Our expander is designed such that the sample is mechanically decoupled from the expander, meaning that vibrations from the expander are damped from the sample. The rooftop carries the expander, and the chamber carries the cold finger. Heat exchange is achieved by two gas heat exchange interfaces in the expander and cold finger, thermally coupling both parts. Isolation bellows in between the heat exchange interfaces are filled with helium gas from an external helium source for optimal heat exchange. Due to this mechanically decoupling of the cold finger and the expander, a direct soft sample mount connected to the cold finger experiences a vibration of under 140 nm. Independent sample mounting to the cold finger, as in our case, is specified to experience vibrations of $3 - 5$ nm.

3. FED on Cu(DCNQI)$_2$ Salts in a High Vacuum

Radical salts of dicyanoquinonediimine, M(R_1,R_2-DCNQI)$_2$ (see figure 3.1, M being Cu, Ag or Li), are crystals of interest because of the properties that they exhibit. Firstly, these salts has a very high conductivity at room temperature. Even more interesting is the phase transition that a group of this collection of salts undergoes: when cooling down, the conductivity drops with orders of magnitude within only a single Kelvin. Some types of these crystals even show a re-entry into the conducting state upon further cool down[24]. Whether these crystals undergo none, one or two phase transitions and at which temperature these transitions happen is dependent on the R_1 and R_2 sidegroups and metallic ion M in the crystal structure[25].

In this chapter, a background in the phase transition properties of these salts will be given. Light will be shed on why these organic crystals are such an excellent candidate for FED experiments. Static electron diffraction patterns that have been acquired with our old HV FED machine are presented. Time resolved experiments have not been successful yet for reasons described here as well.

3.1 Exotic Behaviour of M(R_1,R_2-DCNQI)$_2$ Salts

We mostly look at Copper-dimethyl-dicyanoquinone-diimine Cu(DMe-DCNQI)$_2$ (abbreviated as Cu(DCNQI)$_2$) where the metal component of the crystal is a copper ion and the R_1 and R_2 sidegroups are dimethyl groups. The structure of this crystal is displayed in figure 3.1a. These crystals are grown by Florian Hüwe from the experimental physics VI group from the University of Würzburg, who are long-term collaborators with our group.

The sudden drop and increase in conductivity in some of these crystals are due to the opening and closing of a band gap in the electronic band structure of the crystal. The opening of such a band gap is driven by a structural transition of the organic compounds — called a Charge Density Wave (CDW) formation — that is combined with ordering stacks in copper present in these crystals[26][1]. During CDW formation, three crystal planes of Cu(DCNQI)$_2$ cluster together, superimposing an additional periodicity of $3c$ along the c-axis of the crystal. Three parameters can be used to effectuate a CDW phase transition in these radical organic salts[27]:

- The crystal can be cooled down to below the material-specific metal-to-insulator phase transition temperature,
- Reduction of the appropriate amount of external pressure will induce the phase transition,
- Once the crystal is in the low-temperature insulating phase, a transition back to the metallic state can be photo-induced.

This last statement justifies why these samples are an attractive candidate for FED experiments: a crystal could be cooled into its insulating phase. The crystal can then be photo-switched to being metallic again, and this process could be temporally resolved with atomic

[1]Such CDW formations that also occur in inorganic crystals have been extensively studied by some of our former group members[9; 8].

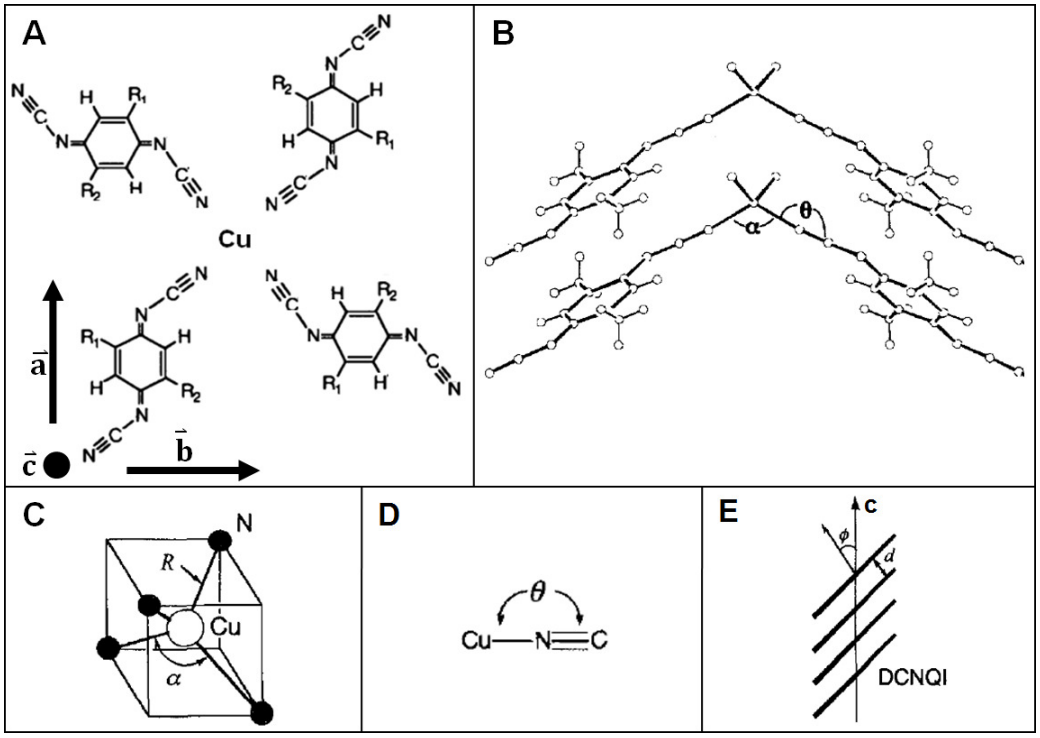

Figure 3.1: (a) Structure of Cu(DCNQI)$_2$ salts, looking into the c-plane. (b) 3D view of the stacking of the crystal planes, displaying angles α and θ. (c) The unit cell of the crystal, showing angle α and radius R. (d) The Copper and Nitrogen are connected with a nitrogen atom with angle θ. (e) Schematic of the crystal looking into the a or b plane, displaying angle ϕ and plane separation d. Image adapted from ref. [25].

precision by employing an electron probe beam in a pump-probe type experiment. In literature, it was shown that this sample can indeed be photo-switched, but only time resolved macroscopic effects such as contraction of the sample and conductivity of the sample have been measured[24]. The charge density wave configuration of the crystal planes in the sample has only been measured statically with an X-ray diffraction experiment[26]. By studying the dynamic metallic behaviour directed by the CDW transition with atomic precision in a sub-ps time resolution, new fields of solid state science can be triggered by this interesting category of materials.

What makes this crystal more compelling to study compared to its inorganic CDW congeners is the rich collection of counter ions or sidegroups that the organic compound can be substituted with: the R_1 and R_2 groups can be substituted with Me, MeO, Cl, Br or I and the metallic counterions can be substituted with metals such as Ag, Li and Cu. Even within, for example, a methyl side-group, hydrogen atoms can be deuterated. This on its own gives, again, rise to even different behaviour[27]. In short: a large spectrum with different types of characteristics is available making this a very attractive crystal to study. Indicated in figure 3.1a-e are the lattice constants a, b, c and the angles α, θ, ϕ and atomic separation R in these crystals. Interchanging the metal compound or the sidegroups in the organic compounds results in the crystal to have different values for these variables, ultimately leading to it having different properties. Different types of M(R_1,R_2-DCNQI)$_2$ salts have been divided into three groups because of their characteristics as following; M(R_1,R_2-DCNQI)$_2$ salts that[25]:

- Don't undergo a metal-to-insulator transition down to 1.2K (group 1),
- Undergo one metal-to-insulator transition when cooled down to 1.2K (group 2),

- Undergo a metal-to-insulator transition, but also an insulator-to-metal re-entry transition when cooled down to 1.2K (group 3).

The Cu(DCNQI)$_2$ crystals that we have to are our availability are h$_8$-Cu(DCNQI)$_2$, d$_6$-Cu(DCNQI)$_2$ and (70%:30%) h$_8$/d$_6$-Cu(DCNQI)$_2$ which are group 1, group 2 and group 3 members respectively. In d$_6$-Cu(DCNQI)$_2$, all six hydrogen atoms in the two methyl groups are deuterated. (70%:30%) h$_8$/d$_6$-Cu(DCNQI)$_2$ is an alloyed crystal that contains a mixture of h$_8$ and d$_6$. Table 3.1 summarises the phase transitions that these three crystals have[24]. Florian Hüwe, the crystal grower, has repeated and confirmed the macroscopic findings of contraction and conductivity drop at the temperatures that have been reported in literature (see figure 3.2), meaning that the reported transitions are indeed present in our crystals.

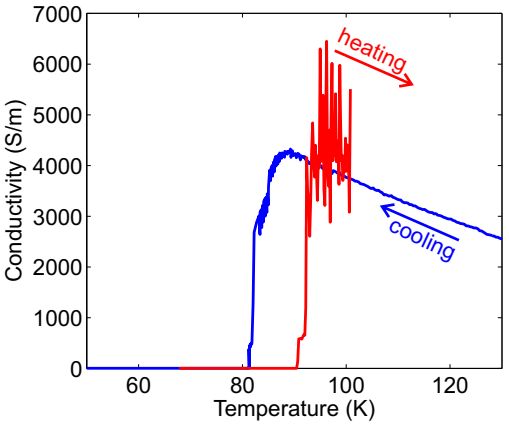

Figure 3.2: Conductivity measurement (by Florian Hüwe) on a d$_6$-Cu(DCNQI)$_2$ crystal showing a massive drop in conductivity upon cooling and a huge rise in conductivity upon heating, driven by charge density wave formation. Significant hysteresis is visible.

Table 3.1: DCNQI salts that we investigated, ordered per group with phases transition and re-entry phase transition shown for a cooling from 300 K to 4 K. Data taken from ref. [24].

Group	Abbreviation	Phases	T_c, T_r (K)
1	h$_8$-Cu(DCNQI)$_2$	Metal	- , -
2	d$_6$-Cu(DCNQI)$_2$	Metal, Insulator	78, -
3	h$_8$/d$_6$-Cu(DCNQI)$_2$	Metal, Insulator, Metal	60, 30

The findings of the photo-switched insulator-to-conductor transition measurements where conductivity changes have been temporally resolved are relevant to the FED experiments that we are yet to perform on this crystal[24]. During these optical measurements, the samples were excited with a 30 ps pulse and the resistivity during excitation was measured. For samples cooled down to the insulating phase, samples showed a short-lived (50 – 80 ps) minor conductivity rise upon photoexcitation. When samples were cooled down to a fraction below the transition temperature, pumping the samples resulted in them being fully excited to the conducting phase with long-lived decays (300 ns) back to the insulating phase. Pumping was done with an excitation wavelength of 533 nm, with fluences between 0.44 µJ/cm^2 and 15.3 µJ/cm^2, which are fluences that we would have available in our laboratory.

The short-lived rise in conductivity upon photoexcitation in the insulating phase of the crystal is assigned to photoexcitation of the electrons and not to structural changes, but a direct look at the atomic structure to confirm this is still missing. Much slower decays were observed in Li-salts, which is assigned to slower diffusion of heat from the surface into the volume. To verify these findings and in order to solve some of these mysteries, a high temporal resolution measurement with atomic precision would be desirable. An atomic view of these decays at different operation points will shed light on the different switching mechanisms.

In summary: different alloys show different phase transition temperatures, which — when in insulating phase — show different decay times back to insulating phase upon photoexcitation into the metallic phase. FED has the potential to resolve the structural changes that are involved in the long-lived switching at the phase temperature and the ultrashort processes happening in the insulating phase.

3.2 Electron Diffraction Patterns of Cu(DCNQI)$_2$

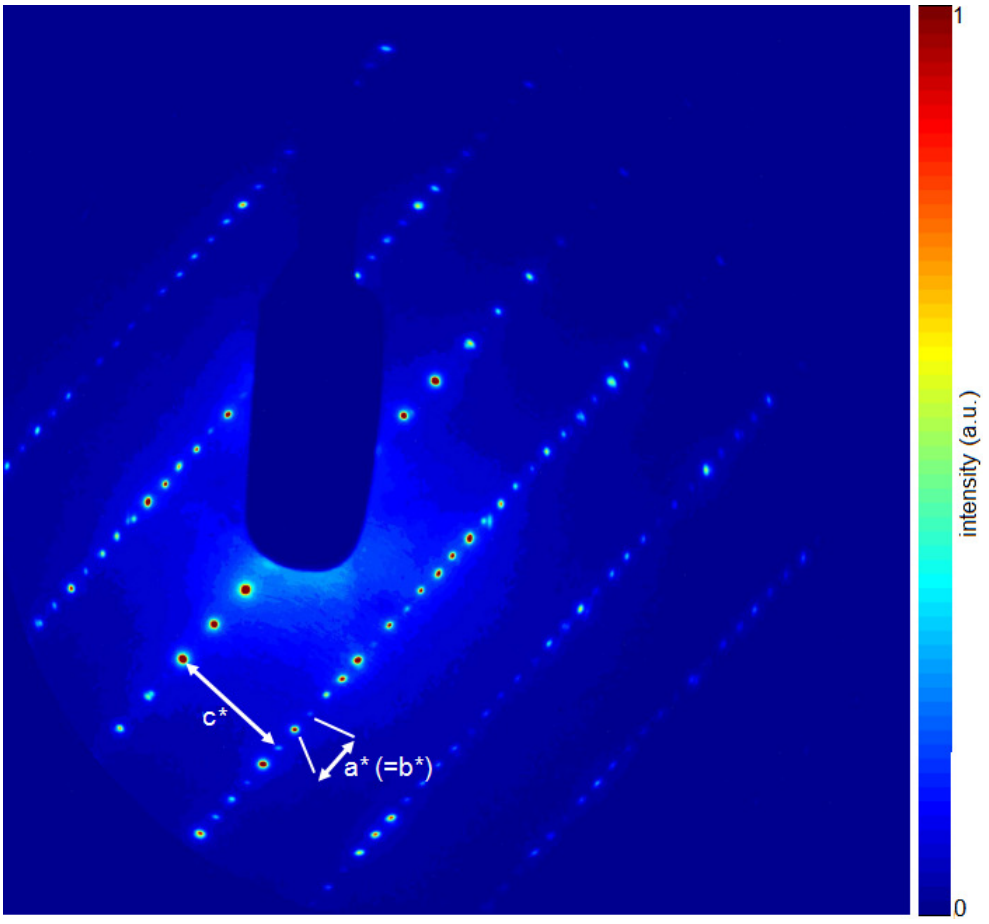

Figure 3.3: A room temperature electron diffraction pattern of Cu(DCNQI)$_2$, acquired with our old HV FED set-up. This image is averaged over 30 images of 60 s exposure time (1000 electrons/pulse, 1kHz repetition rate). A beam block prevents the high-intensity 0th order diffraction peak from damaging the imaging system.

Preliminary results of experiments on Cu(DCNQI)$_2$, have been acquired in our old HV FED set-up. Samples were cut in an ultramicrotome with a diamond knife. Slices with a thickness of around 30 – 50 nm rest on a regular TEM mesh. An aperture is glued onto the mesh, so that when the electron beam in our set-up is aligned through the aperture, an useful sample slice is exposed to the beam. Our samples are cut along the c-axis (which means that the electron beam 'sees' the stacking of the crystal planes, like in figure 3.1e). Such a diffraction pattern is shown in figure 3.3.

Individual diffraction peaks can't be assigned to individual positions of atoms as the diffraction pattern is the reciprocal space representation of the real space crystal structure. However, the ratio of a (= b, 21.613 Å) and c (3.883 Å), which equals 5.57, is identical to the ratio

between c^* and a^* in the diffraction pattern (note that high periodicities in real space correspond to low periodicities in reciprocal space). Most of our experiments were done on the d_6-Cu(DCNQI)$_2$ alloy. The trimerisation in the insulating phase has a periodicity of $3c$ that is superimposed in the c-axis. This periodicity is three times as low as the metallic phase periodicity. In reciprocal space, this results in two extra 'CDW'-peaks in between the usual Bragg diffraction peaks. These CDW-peaks are expected to have a $\frac{1}{3}c^*$ CDW-peak separation. This is confirmed by an X-ray diffraction pattern[26] (figure 3.4a) where two rows of extra CDW-peaks are claimed to be observed between the existing main diffraction peaks when the sample is below the transition temperature. Olufemi Oloaye, a Ph.D. student in our group who is specialised in electron diffraction simulations, confirmed the expectation that CDW peaks should appear by performing a simulation (fig. 3.4b).

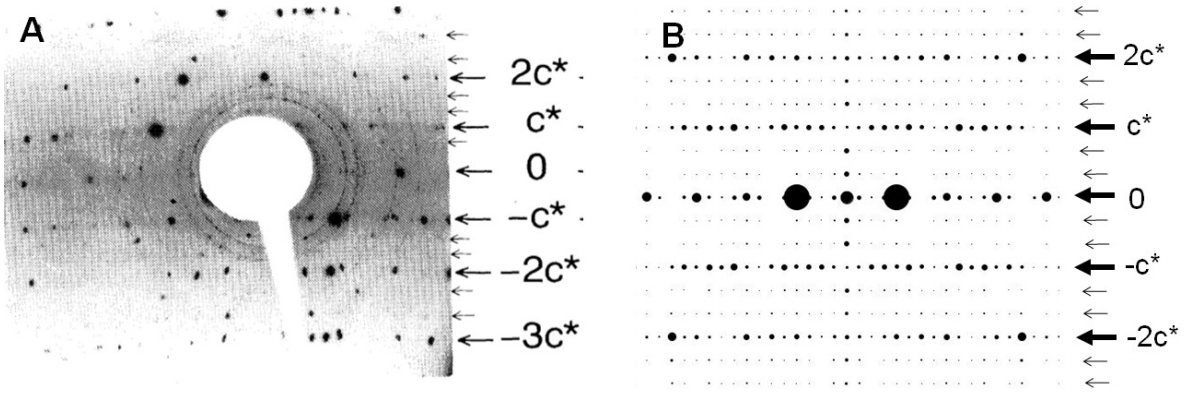

Figure 3.4: (a) An X-ray diffraction pattern of d_6-Cu(DCNQI)$_2$ taken at 20 K, where additional CDW-peaks are claimed to be observed (indicated by the small arrows, pattern taken from ref. [26]). (b) 20 K electron diffraction pattern simulation by Olufemi Oloaye where CDW peaks appear between the main Bragg peaks.

The first step in our FED experiment on Cu(DCNQI)$_2$ would be to cool down the sample and observe the CDW, after which the sample could be pumped and probed. In an attempt to access the insulating phase, several cooldowns were performed[2]. For the example covered in this chapter, the sample was cooled to 50 K with the cryostat. Figure 3.5a shows a single diffraction pattern of the sample at room temperature, whereas figure 3.5b shows an average of 39 images of the sample at 50 K. No CDW peaks are visible. We assign this to a point raised earlier: external pressure can induce the phase transition, but 'negative' pressure can also prevent the phase transition from happening. When the sample undergoes the phase transition, its volume suddenly contracts with 0.4%[24]. Our sample is attached to a TEM mesh which is 'pulling' the sample such that it stays in the metallic phase when it is 'trying' to go to the insulating phase. Note that low temperature conductivity measurements on our bulk samples confirmed that the samples are able to undergo a phase transition.

Another concern rises when comparing figure 3.5a with 3.5c. It seems that after cooling the sample, the quality of the sample deteriorated significantly. In fact, if we look at the Bragg signal of the 39 individual images of the scan taken at 50 K (fig. 3.5b), there is a signal decay of around 30% visible. This decay is plotted in figure 3.6. When looking at the individual images

[2]One example of a cool-down is shown in this chapter, an overview of all attempts to access the insulating phase is attached in Appendix A.1.

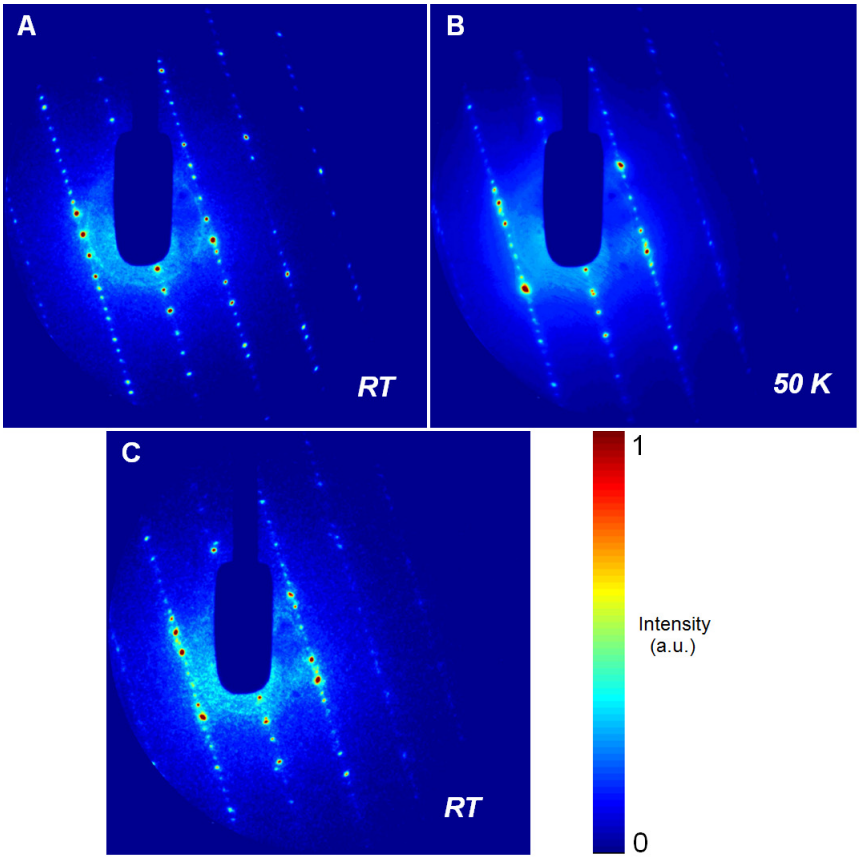

Figure 3.5: (a) A room temperature electron diffraction pattern of d_6-Cu(DCNQI)$_2$, obtained with 10^6 electrons/second and 60 s exposure time. (b) A $T = 50$ K pattern, averaged over $39 \cdot 60$ s exposure images, no CDW-peaks are observed. (c) A 60 s exposure room temperature pattern after the cool-down to 50 K.

of such a scan it becomes evident that the sample quality worsens over time as it sits at cold temperature. We assign this phenomenon to condensation of matter from our vacuum onto our sample that is on low temperature (this typically happens at temperatures <120 K and might be due to water, nitrogen or oxygen in the vacuum). Implementation of shields around the sample and a 'coldtrap' — a liquid nitrogen cooled finger sticking into the chamber to collect matter so that it can't condensate onto the sample — achieved minor improvements but didn't solve this problem. This is all covered extensively in appendix A.1. In other words: our HV chamber is not suitable for performing FED at temperatures as low as these. A lower pressure is required to prevent this condensation effect from happening, which serves as a justification for the UHV FED set-up that was developed and described in chapter 2. Now that the this new system has been developed, the attempt to access the insulating phase will be repeated.

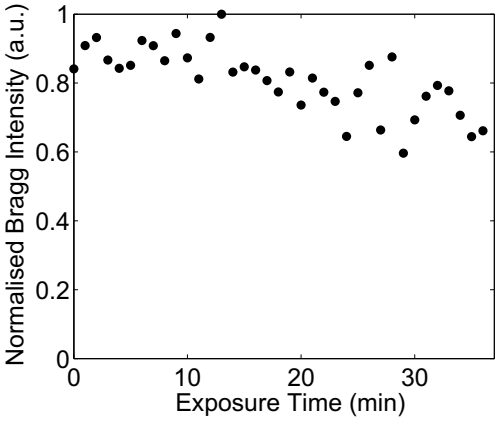

Figure 3.6: Graph displaying the decay in signal of the brightest diffraction peaks of the Cu(DCNQI)$_2$ patterns while the sample is at 50 K.

4. Numerical Electron Pulse Optimisation

To start this chapter off, let us go back to our bullet-apple analogy once more. Imagine having a stroboscope that emits long flashes to probe dynamics in the apple. Fast dynamics such as the fast flying bullet in such a photograph will be blurred out as time resolution is worsened. The undesired Coulomb repulsion effect within single electron probe pulses that was mentioned in chapter 2 has a similar effect: electron pulse broadening worsens both temporal and spatial resolution in our atomic movies and blurs out fast dynamics happening in our sample. It turns out that electron pulse broadening, conceptually sketched in figure 4.1, is such a severe effect that it's one of the biggest challenges and limitations in FED. Research about the physics behind these space charge effects, and ways to counteract them, are widely covered in literature. To understand, optimise and improve temporal and spatial parameters in our FED set-up, detailed knowledge of the evolution of electron pulses in all dimensions is crucial. In this chapter, the main findings of the work that was already done on space charge effects in ultrashort propagating electron pulses is summarised. This knowledge, combined with newly obtained simulation results, is used in an attempt to design the anode-cathode configuration discussed in section 2.3.2 in the most favourable way as possible in order to suppress electron pulse broadening.

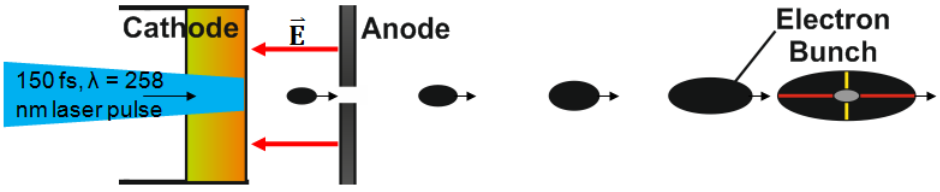

Figure 4.1: Sketch of electron pulse broadening during propagation. Grey oval in last electron pulse represents initial electron pulse dimensions. Yellow lines illustrate spatial broadening compared to initial pulse width and red lines illustrate temporal broadening compared to initial pulse duration.

4.1 Spatial and Temporal Broadening of Ultrashort Electron Pulses

Temporal broadening and spatial broadening due to space charge effect is more severe for higher electron densities, meaning that a trade-off must be made between temporal resolution and signal strength[20; 28; 29; 30]. Especially in single shot FED experiments, where around 10^7 electrons per pulse are required, maintaining temporal resolution as well as spatial coherence is challenging, as having such a high electron current from only a single shot can result in significant distortion of the electron diffraction patterns[31]. Attempts to reduce and improve on the setbacks of space charge effect include implementation of electron probe pulses that consist of only a single electron[32], the implementation of a cathode that emits femtosecond electron pulses from a metal nanotip [33; 34], employing relativistic electron energies in the MeV range[35; 36] and the acceleration of electrons by laser-driven plasma waves[37]:

- When using single electrons, the absence of Coulomb repulsion in a probe pulse eliminates Coulomb broadening effects[32]. Such a single electron probe pulse is still not jitter free due to the duration of the laser pulse that photo-electrically generates the single electron. The setback is obvious: signal collected is extremely weak and sensitive detectors, long integration times and high repetition rates are needed for data collection. This means that many shots have to be performed during a single experiment. Not all samples are suitable for this, as some samples undergo damages during continuous electron and photon radiation exposure. Samples also need sufficient time to recover after one shot, limiting the repetition rate on which an experiment can be performed.

- Nanotips emit electrons from a very localised tip area upon photoexcitation and the strong fields around this area enhance the ionisation and initial acceleration of the electrons[33; 34]. Strong fields in the initial acceleration are advantageous for suppression of Coulomb repulsion (as will be learned from calculations in this chapter as well as from literature). Big disadvantage of emission from nanotips is that the trajectories of the electrons can be widespread, resulting in a divergent beam with undesired temporal and spatial features. Furthermore, it has not been possible to accelerate electrons from a tip to kinetic energies in the kV regime even when post-acceleration is utilised.

- Having relativistic electrons with energies in the MeV regime suppresses Coulomb repulsion as a function of the travelling distance due to the relativistic effect[35; 36]. Furthermore, the effective propagation time of the electron pulse is reduced as the electrons takes shorter to reach a long distance. This gives space-charge induced broadening less time to act. Experimental challenges in operating under such high voltages are the small diffraction angles after interaction with samples, as well as possible sample damage due to increased radiation. Furthermore, achieving sufficient detection efficiency for relativistic electrons is a challenge.

- Relativistic electron bunches can be produced by electron acceleration in laser-driven plasma waves[37]. By focussing a laser pulse on a gas coming from a supersonic gas laser jet, a plasma is generated. Electrons in the plasma are accelerated to super-relativistic energies due to the high electric fields inside the plasma. This technique has the potential to generate few-fs electron pulses with electron number large enough to be suitable for single shot diffraction. However, these systems are complex, bulky and stability of the electron beam is a challenge.

Because of the experimental complications in these four alternative FED techniques mentioned above, we don't employ any of these possible solutions for improvement on broadening effects in our FED set-up but we rather rely on an electron compressor in the near future (as will be described in chapter 6). However, much literature about broadening of electron pulses that are generated in a way that is similar to ours, a back illuminated photocathode, is readily available. The results from literature presented in this chapter are mostly extracted from three publications. Relevant results from these publications are summarised and ordered in two subsections: a subsection focussing on transverse (spatial) characteristics and a subsection focussing on longitudinal (temporal) characteristics. The papers are:

- A publication from 2002 by Siwick et. al., where N-body simulation calculations are compared with analytical mean-field model results. Implications of the outcomes of these calculations for propagating electron pulses are presented[20]. This paper focusses on transverse (temporal) broadening effects where the beam radius is assumed to be constant (200 µm). The simulation and the analytical result — that are in perfect agreement — are compared with an experimental result. A pulse duration of 2.5 ps

is obtained after a propagation of 1.5 ns (or 0.45 m). This post-picosecond temporal duration result is compared with an experimental result, but techniques to accurately measure sub-picosecond temporal durations were not available at the time.

- A publication from 2005 by Collin et. al., extending the model from the previous paper for three dimensions, allowing them also to look at spatial (longitudinal) broadening effects[28]. Experimental spatial characterisation is much simpler to achieve compared to temporal characterisation because spotsize can be measured with a razorblade (with the technique described in chapter 5.2 of [22]), enabling to observe spotsize on the detector directly. This allowed the author of this paper to compare calculated electron spotsize directly as a function of distance with experimental results. Although this allows for comparison along the entire electron beamline, spotsize is a less crucial experimental parameter compared to temporal duration. Temporal duration is not measured in this paper at all.

- A publication from 2008 by Gahlmann et. al., where the analytical model is extended to allow to include fields of the electron gun and magnetic lens that are experimentally feasible[29]. For the first time, a wide range of pulse durations are measured by streaked experiments and compared with the calculations. These are relevant results, but again temporal resolution of the experimentally measured pulse duration is low[1].

4.1.1 Spatial Resolution

Spatial broadening in the acceleration (cathode-to-anode) region is suppressed when the electric field is high enough (> 5 MV/m)[39]. Calculations were compared to experiments for transverse broadening, revealing that broadening due to space charge effect can become neglectable when the initial pulse width is high enough (> 40 µm)[29]. Space charge effects become neglectable because of lowered electron density, and broadening is then mainly due to the initial kinetic energy spread. The initial energy spread can be reduced by producing photoelectrons with a narrow energy bandwidth ΔE and high mean kinetic energy. This is why the third harmonic of the fundamental laser beam is produced to serve as an input, as discussed in sections 2.3.1 and 2.3.2. For a given initial pulse width, the final pulse width after propagation reduces as a function of voltage, making it advantageous to perform experiments on high voltages. Introducing a magnetic lens in the simulations has shown that the beam waist at detector position can be reduced to a FWHM beam waist of around 0.35 mm. For each simulation, the current of the magnetic lens should be optimised to minimise beam waist at the detector. Having the ability to control beam waist by tuning the magnetic lens current makes the temporal broadening a more crucial limiting broadening effect than spatial broadening[28]. Hence, for all simulations performed for our set-up in this chapter, magnetic lens current is adjusted to minimise beam waist at detector position, and we mostly focus on temporal resolution results.

[1]Note that in the last paper, the pulse duration measurements technique presented doesn't allow for sub-picosecond pulse duration measurements[38]. This means that pulse durations with low electron number and short gun-to-interaction region distance with sub-picosecond pulse durations — conditions under which one would perform an actual FED experiment — have been calculated but not confirmed by pulse duration measurements along an entire beamline. This means that the pulse duration measurements with 150 fs accuracy that are presented in chapter 5 of this thesis are not only interesting for our set-up specifically but contributes to the general electron pulse propagation literature that has been published to date.

4.1.2 Temporal Resolution

The contributions of temporal broadening are due to two effects: the initial energy spread in the electron beam and the space charge effects due to Coulomb repulsion. These two have been simulated separately, and simulations including both initial energy spread and space charge effects combined have been performed. Suppressing temporal broadening due to initial energy spread can be achieved by having a low energy spread. Space charge effects can be suppressed by having high electric field in the electron gun (conditions that also apply to the suppression of spatial broadening). Pulse duration as a function of propagation time does not depend on electron energy. In other words: having high electron energies gives broadening effects less time to act, thereby reducing the pulse broadening as a function of distance.

Simulations have revealed that the space charge effect is the significant contributor and that broadening due to initial energy spread is much lower. For example, in a 60 kV gun with 3 mm gap separation (E = 20 MV/m), the increase in temporal duration (t_0 = 120 fs) after 645 mm of propagation is 0 – 50 fs for initial energy spreads of 0 – 1 eV respectively when space charge effects are neglected. When only space charge effects are taken into account (i.e. $\Delta E = 0$), the increase is 5 – 25 ps for 1.000-100.000 electrons per pulse respectively[29]. For simulations that are done in this chapter, both initial energy spread and space charge effects are taken into account as they both play a role in the pulse duration. Calculations show that pulse duration broadening can be small in the acceleration region, whereafter it follows an almost quadratic relationship in the drift region, flattened off by a close-to-linear relationship for propagation times longer than 2 ns (corresponding to $\sim$ 0.2 m in our case of a 50 kV electron gun). Electron pulses of an initial pulselength of 50 – 500 fs with 10.000 electrons per pulse are broadened to around 2 ps, which has been confirmed by a streaked experiment[20]. This clarifies the difficulty in doing FED experiments with sub-picosecond pulses, as performing experiments with such low electron currents obtains only little signal. The trivial solution is to keep the cathode-to-sample distance as small as possible to prevent broadening from happening: sub-ps time resolutions can be obtained for distances <5 cm.

An interesting finding from the N-body simulations is that when electron pulses broaden, they develop a nearly perfect linear chirp: slower electrons get decelerated and faster electrons get accelerated such that the z-position of an electron in the pulse vs the relative axial velocity is a linear relationship. This linear chirp opens the door for recompression of temporally broadened electron pulses, as will be discussed in chapter 6.

4.1.3 SuperFish and ASTRA Simulation Software

The aim is to perform simulations similar to the ones that were done in literature, but for our geometry specifically. Strong electric fields are generated in our gun when having a high voltage cathode close to a grounded anode. There is a desire to simulate the electric fields in the cathode-anode gap for the following two reasons:

- To make sure that the electric field in the gun stays under the physical limit of 10 MV/m. Surpassing this limit will ionise the metallic cathode surface, and arcing problems can be expected[40].
- To map out the electric field that the electrons will experience as they propagate through the gun, in order to predict their space charge behaviour (by using other simulation software).

Poisson Superfish is a collection of programs used to calculate static magnetic and electric fields and radio-frequency electromagnetic fields in either 2-D Cartesian coordinates or axially symmetric cylindrical coordinates. In its interface, metallic or dielectric shapes can be programmed and a voltage can be applied to it. The programs then generates a triangular mesh fitted to the boundaries of those different materials in the problem geometry that was defined by the user. Postprocessor codes can extract the results of the electric field generated by the programmed objects. One postprocessor allows to take a line in the simulation volume and plot the electric field strength along that line. This allows us to, for example, take a line through the volume exactly where we expect the electrons to travel so that the electric field that they experience can be mapped out.

Once the electric field is known, broadening effects of electron pulses in that field can be calculated. Unfortunately, making analytical derivations of beam expansion that are experiencing external electric and magnetic fields (that of the gun and that of the magnetic field) as presented in the above-mentioned literature, is an extensive exercise and not practical for gun design purposes. Therefore, we resort to numerical calculations. In the literature discussed above, N-body Monte Carlo simulations[29] and Barnes- hut leapfrog algorithm[20] were used for numerical calculations. For this study, it was chosen to use ASTRA — abbreviation for 'A Space TRacking Algorithm' — simulation software. It is freely available and well suited for simulations of propagating electron pulses that are emitted from a photocathode. ASTRA is a code that can track (charged) particles as they propagate. This simulation software allows to import external electric fields, such as the field of the gun, magnetic lens or a compressor, that are simulated with Superfish/Poisson. The complete collection of inputs that ASTRA needs for it to track the space charge in an electron pulse as a function of time is:

- The electromagnetic fields that the electrons experience as they propagate, extracted from SuperFish calculations (in our case the gun and the magnetic lens),
- The number of electrons within one bunch[2] which is measured with a Faraday cup,
- The initial pulse duration of the electron pulse, which can be assumed to be the same as the UV laser pulse duration (section 2.3.2),
- The spotsize of the electron pulse at the cathode, measured with the knife-edge method (which will be explained in section 5.2).
- The Fermi energy (5.5 eV for gold[40]) and effective work function of the photocathode (4.2 eV for gold[40]) and photon energy of incoming UV beam (4.8 eV corresponding to $\lambda = 258$ nm).

[2]Electron number per pulse can be varied by varying the UV intensity that's rear-illuminating the cathode (labelled 'attenuator' in figure 2.1).

4.2 Numerical Results of Operational FED-guns

4.2.1 Current 50 kV Electron Gun

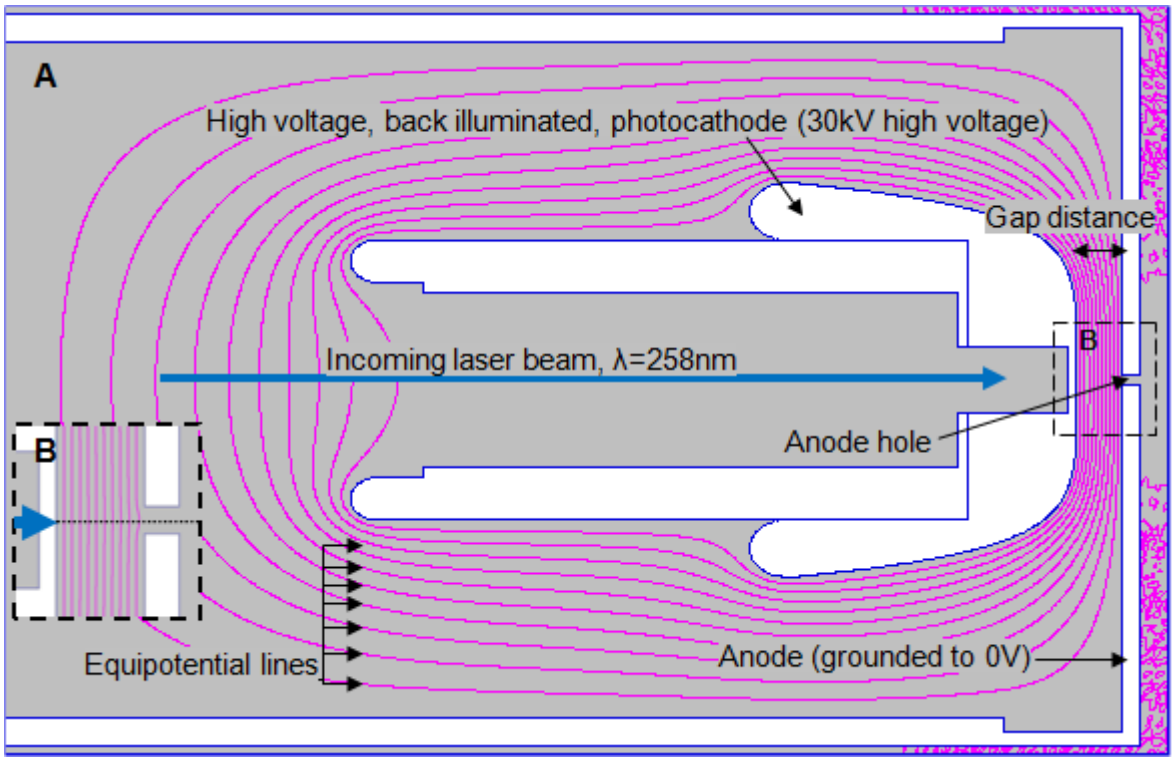

Figure 4.2: (a) Superfish electrostatic field simulation of the electric field of the old HV electron gun with a Rogowski profile cathode (cylindrical symmetry around the central axis). Electrons are generated on the cathode at the laser incidence, and accelerated through the anode hole in the strong electric field that is displayed. (b) Dotted inset: zoom-in of where electrons are generated. Dotted line displays trajectory that electrons will travel in the strong field.

The SuperFish simulation output of the old HV gun design is shown in figure 4.2. The dotted line in the inset (fig. 4.2b) shows the trajectory that the electrons will travel in the strong field. The electron pulse spotsize as it travels inside the gun remains around 35 µm. This is a very small distance compared to the dimensions of the gun. Therefore, it can be reasonably assumed that the field is homogeneous in the transverse direction and that a line-out of the electric field through the centre is a good assumption for the electric field that every electron in the pulse experiences inside the electron gun. The cathode holder in this case has a Rogowski profile: it starts with a subtle curvature, and the curvature is increased as the cathode-anode gap separation

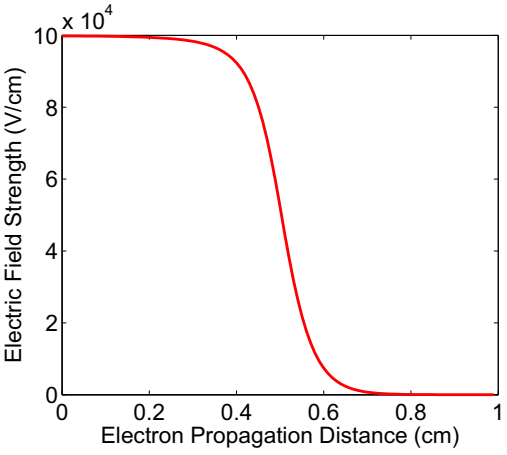

Figure 4.3: Plot of electric field strength along travelling axis of electrons(dotted line in fig. 4.2b) for the Rogowski profile gun on 50 kV.

increases. This profile was chosen because it produces an uniform field between the cathode and anode cap and due to the specialised curvature there are no strong fields generated inside the gun. In this way, arcing is suppressed. With a postprocessor, the electric field strength along the dotted line in figure 4.2b was extracted and plotted. The electric field strength, which serves as an input for ASTRA, is plotted in figure 4.3. The maximum field strength in this plot is 10 MV/m, which is an acceptable conclusion seeing that the field is approximately uniform at the surface, and for uniform electric fields the equation $E = \frac{U}{d}$ holds (U for applied voltage to cathode, d for cathode-anode gap distance). For a voltage of 50 kV with a gap of 5 mm, this indeed yields a field strength of 10 MV/m.

This electric field serves as an input for the ASTRA simulation, together with the magnetic field of the magnetic lens. Kerstin Haupt designed the magnetic lens, and Superfish simulations of the magnetic field have been performed by her and Günther Kassier. The magnetic field that was used as an input for ASTRA is taken from chapter 4.3.2 of ref. [23]. Simulations show that implementation of the magnetic lens has little influence on pulse duration. For the simulations, the following standard conditions were chosen:

- An electric field strength of 10 MV/m (the field strength for an anode-cathode gap of 5 mm).
- An electron number of 1000 electrons per pulse, which is a typical electron current for FED experiments.
- An initial pulse duration of 150 fs (FWHM, Gaussian shape), which is the pulse duration of the incident UV pulse.
- Standard spotsize was chosen to be 35 µm (FWHM, Gaussian shape), which is the experimentally measured spotsize for the 300 mm focussing lens that is used to focus the UV light on the cathode (as will be discussed in section 5.2).

The ASTRA simulation results are shown in figure 4.4. As starting conditions, the above-mentioned values were used, but the electric field strength (by increasing cathode-anode gap), electron number, initial pulse duration and initial spotsize are varied individually.

The electron pulse duration expansion is plotted until a propagation distance of 10 cm; a typical cathode-to-sample distance is 6 – 7 cm. In each of these simulations, the magnetic lens current was optimised so that the electron beam waist at the detector is the smallest. A few conclusions can be drawn from this figure:

- From fig. 4.4a it is deducted that when the electric field strength is too low, temporal durations at the sample position worsens significantly (225 fs for $E = 10$ MV/m as opposed to 275 fs for $E = 4$ MV/m at 6 cm propagation distance). However, it is not critical to have a gap size below 8 mm (corresponding to a field strength of 6 MV/m) as for anything below that, the temporal resolution remains around 225 fs at sample distance. Having electric fields as high as possible to limit initial broadening is confirmed by literature[39] and the finding that it is not critical for field strengths above 5 MV/m corresponds to other published simulation data[29].
- Controlling broadening in the drift region is not as trivial as it is inside the gun. From figure 4.4b, it is clear that the electron number per pulse has a severe influence on the pulse duration, numerically proving temporal resolution loss for ultrabright electron bunches, a major limitation that was mentioned earlier. For electron pulses with 8000 electrons each — corresponding to an electron current of only 1.3 pA — the temporal duration after 10 cm propagation is 1.0 ps whereas for a pulse with 1000 electrons this is only 300 fs.

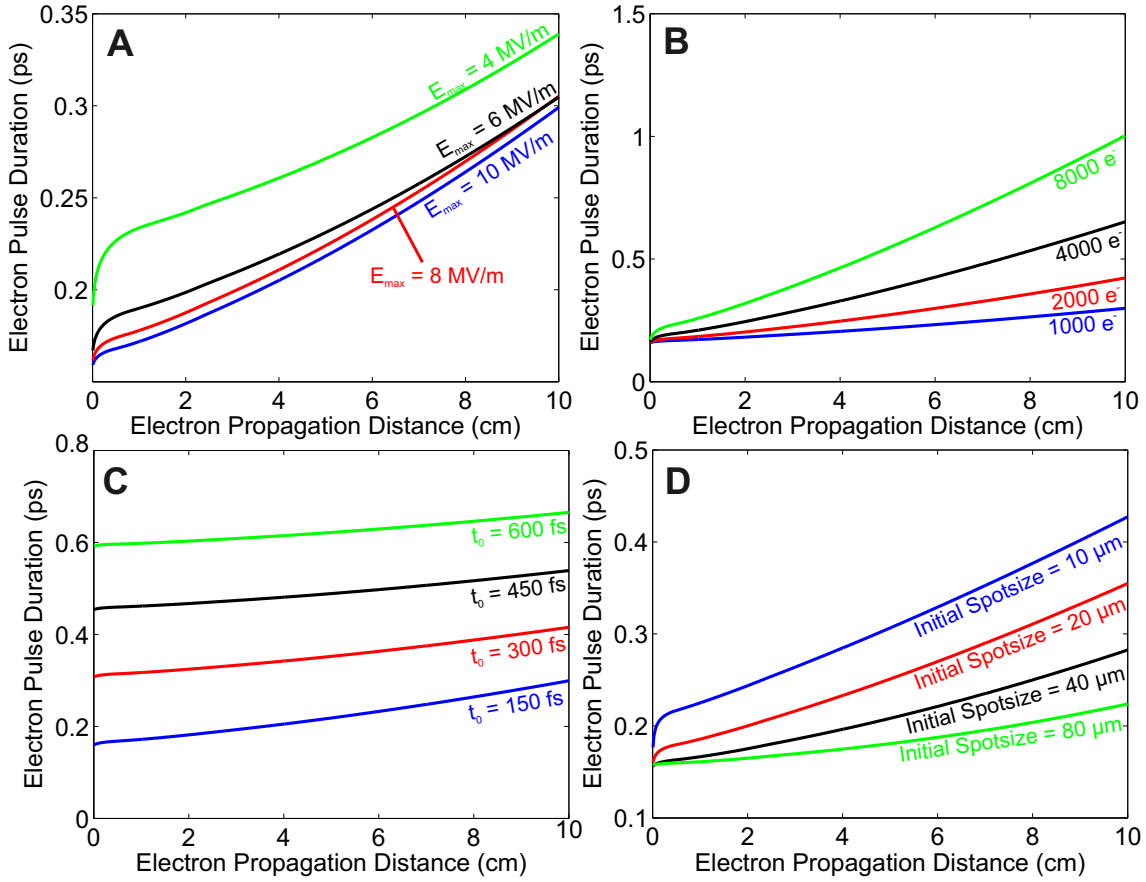

Figure 4.4: (a) Electron pulse durations as a function of propagation distance for different electric field strengths, (b) electron current, (c) initial pulse duration and (d) initial spotsize, illustrating the temporal broadening effect for different initial conditions. Standard initial conditions: $E_{max} = 10MV/m$, $t_0 = 150fs$, 1000 electrons/pulse, 35 µm initial spotsize.

- Longer initial electron pulse durations (which in practice means longer incoming UV laser pulses) results in what is almost a linear shift (as visible in fig. 4.4c), making it obvious that using short laser pulses is advantageous for high temporal resolution. Although, according to ref. [29], having initial pulse durations < 50 fs results in expansion becoming so much stronger that there is a cross-over point where temporal duration becomes longer due to increased electron density.

- Lastly, from figure 4.4d, it becomes apparent that having a bigger initial spotsize (which in practice means having the cathode out of focus of the incident UV beam, or using a long focal length UV lens to focus the incident UV beam onto the cathode) seems to improve temporal resolution. A spotsize of 80 µm results in a temporal resolution of around 200 fs at sample position whereas for a spotsize as small as 10 µm, a temporal resolution of around 330 fs is achieved. Small spotsize on the detector, and thus improved spatial resolution, is achieved by having smaller initial spotsizes (as will be proven in section 5.2), meaning that there is a trade-off between temporal and spatial resolution.

4.2.2 A 100kV Cathode Design

A new photocathode design is investigated to see if any improvements can be achieved in either pulse radius or duration by altering size and shape of the cathode surface and/or anode hole. In this section, the 100 kV electron gun design made by Prof. Dr. B.J. Siwick, a pioneer

in the field of FED, will be compared with our 50 kV HV gun for which simulations were presented in the previous section. Siwicks gun is designed for front-illumination as opposed to rear-illumination in our case. A Superfish simulation of the static electric field generated by this design is demonstrated in figure 4.5.

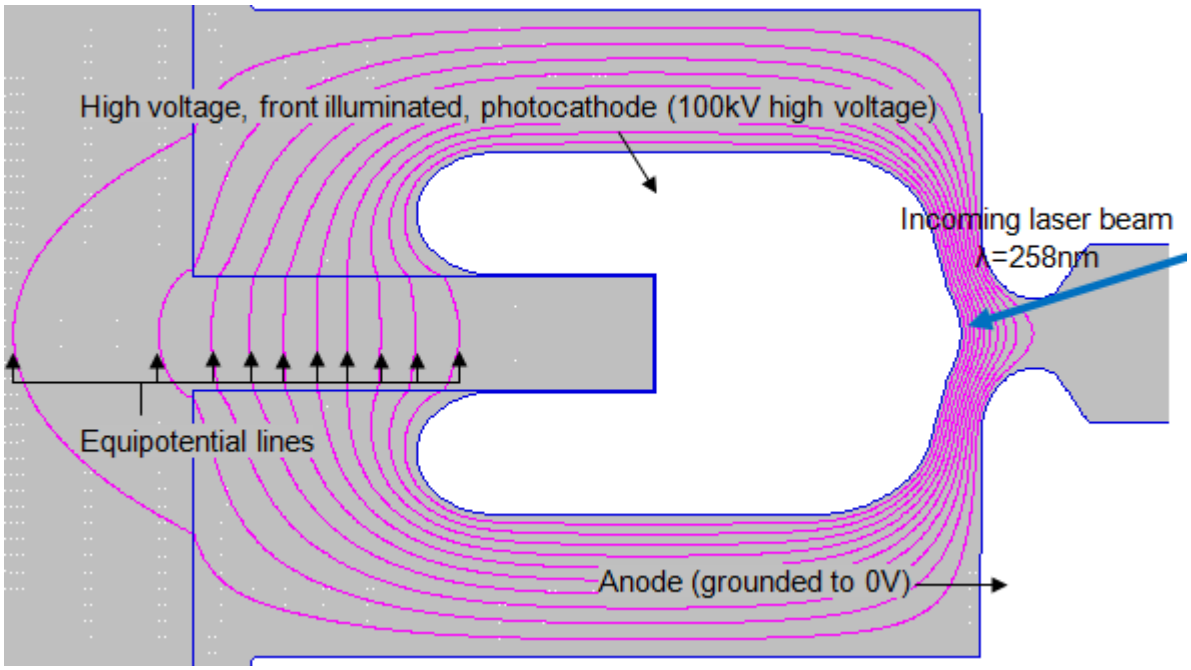

Figure 4.5: SuperFish simulation of electric field strength in the 100kV electron gun as implemented in the FED set-up in Prof. dr. B.J. Siwicks research group.

Biggest difference with this gun compared to the gun in figure 4.2 is that the gun has a bigger anode hole to accommodate for the laser beam coming in from the front: this gun is front illuminated with the UV light being focussed on a (bulk) copper cathode. Because of the increased anode hole size, the electric field along the beam line is decreased. To compensate for this, an extra 'bump' present on the cathode enhances field strength at the centre of the gun. There are certain advantages to front illumination. We have found that it is difficult to let the electron gun operate stably for front illumination (despite the femtosecond laser having a stability of within 1% within 27 hours[41]). Prolonged UV exposure of the cathode results in serious damages where 'burned' spots on the cathode result in a decay of electron number of up to 50% during an experiment of 10 hours[41]. By having a bulk photocathode, these instabilities are eliminated. On the other hand, alignment endeavours are complicated because the incoming UV-beam and the outgoing electron beam are no longer aligned onto the same beamline.

Seeing that the design in figure 4.5 performs on a higher voltage, Coulomb repulsion as a function of the travelling distance is suppressed as has been discussed previously. Therefore, it is expected that this 100kV gun design performs better than our old 50 kV gun design. To make a fair comparison between the two gun designs, the HV gun simulations are adjusted so that it can numerically operate on 100 kV. The only thing that needs to be monitored in the simulation results is that the electric field is kept below the maximum limit of 10 MV/m. Keeping the electric field under that limit can be done by simply increasing anode-cathode gap in Superfish. The simulation gapsize is increased to 10 mm. The electric field line along

electron propagation axis is extracted from the simulation and compared with the electric field of the design in figure 4.6a. ASTRA simulations of electron pulses experiencing these electric fields are shown in figure 4.6b. For the ASTRA simulations, the standard 150 fs initial pulse duration, 35 µm initial spotsize and 1000 electrons per pulse initial conditions were used, as well as the implementation of the magnetic lens (which has little influence on the pulse duration anyway).

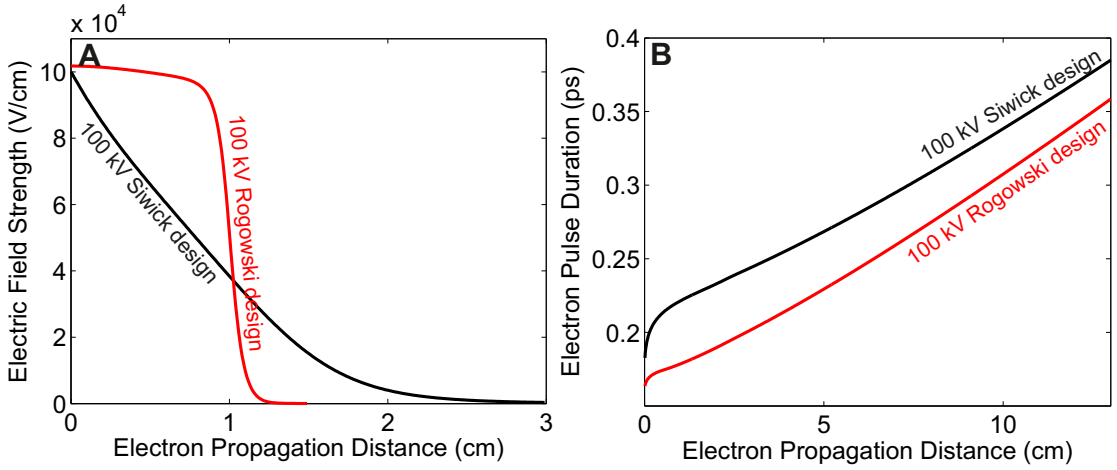

Figure 4.6: (a) Electric field strength along electron propagation axis for Prof. Dr. Siwicks 100 kV gun design, compared with our gun adjusted for 100 kV. (b) ASTRA simulations with electric field input as in (a), displaying temporal broadening as a function of the travelling distance.

From these calculations, it becomes apparent that although the 100 kV design is much easier in terms of aligning optics for front illumination — which was the purpose of this design — its shape does not necessarily contribute to minimising the pulse duration broadening. From figure 4.6 it becomes clear that at a distance of 6 cm Siwicks gun achieves a pulse duration of 280 fs, as opposed to 240 fs for our old gun if it were to perform on 100 kV. This confirms the finding that homogeneous fields are better[28; 29] and that in our case of back illumination there is not necessarily anything to gain in terms of temporal resolution by increasing the anode hole or cathode curvature. The difference between the two guns were further investigated by varying the two main differences in simulation: the anode hole size (which is bigger in Siwicks design) and the curvature at the point of electron generation (which is higher in Siwicks design). In order to do so, SuperFish simulations of our gun varying both the gap size (fig 4.7a) and the curvature (fig 4.7b) are performed. The latter is done by introducing a small Gaussian 'bump' on the centre of the cathode, of which the amplitude is increased, which in turn increases the curvature. The anode-cathode gap was increased for each simulation for a certain curvature so that the maximum electric field strength does not exceed 10 MV/m. Electric field strength along the line of propagation of a wide variety of anode holes (fig 4.7c) and curvatures of the cathode (fig 4.7d) were extracted from these simulations. This electric field strength served as an input for ASTRA simulations, where the initial conditions were as usual. ASTRA simulation results are displayed in figure 4.7e;f.

These results support our previous findings. Increasing the anode hole and/or curvature on cathode makes the electric field less homogeneous (fig. 4.7c;d), which ultimately results in longer electron pulse durations (fig. 4.7e;f). This brings the optimised design back to the

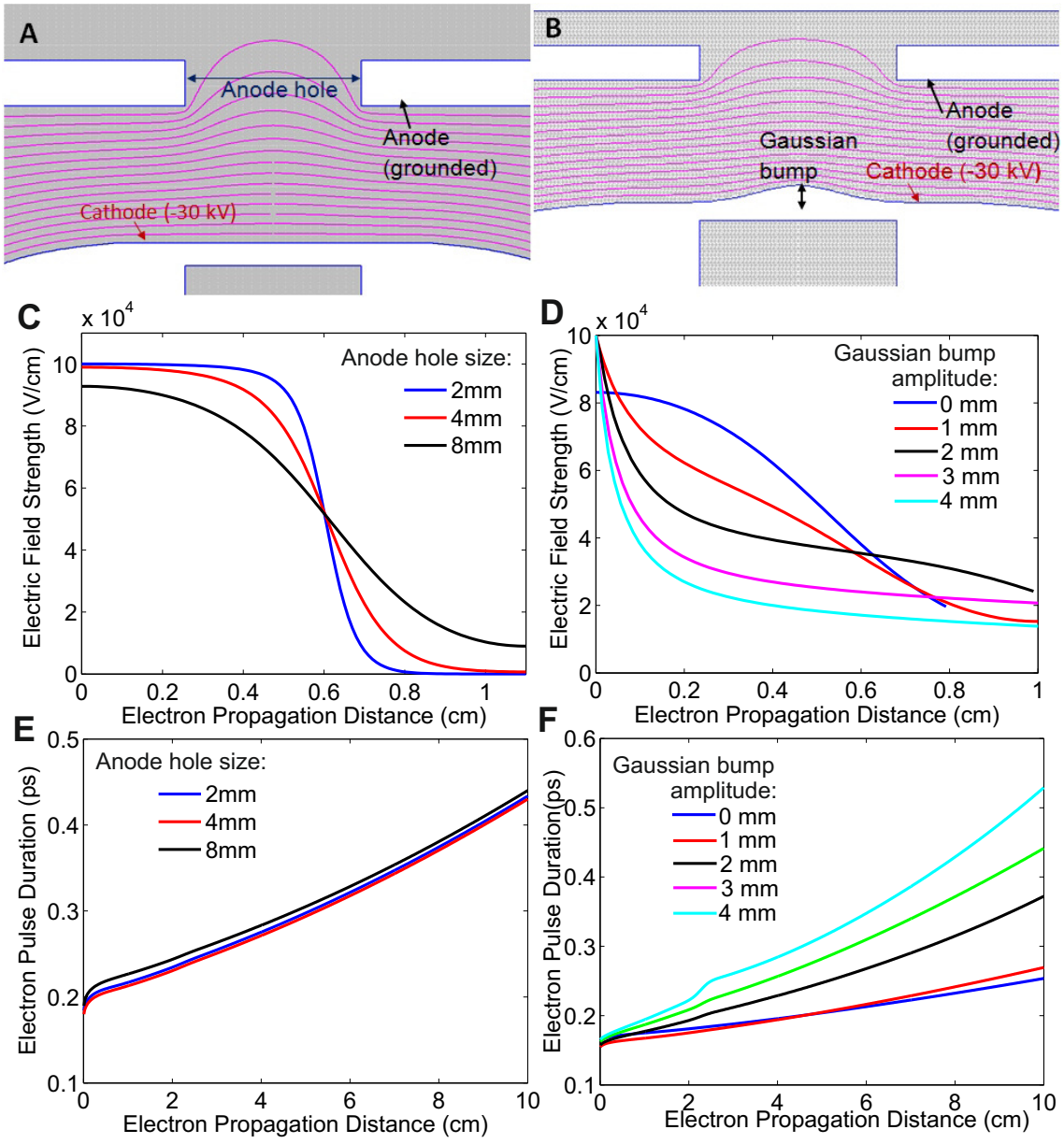

Figure 4.7: (a) Superfish simulation of an electron gun displaying the increase in anode hole size for several simulations. (b) Superfish simulation of an electron gun displaying the increase of the amplitude of a Gaussian 'bump' for several simulations. (c) Electric field strength along the electron beam propagation axis for several anode hole sizes. (d) Electric field strength along the electron beam propagation axis for several Gaussian bump amplitudes on the cathode. (e) ASTRA simulation displaying the electron broadening effect for several anode hole sizes by imported data from (c). (f) ASTRA simulation displaying the electron broadening effect for several amplitudes of Gaussian bumps on cathode by imported data from (d).

design that was presented in section 4.2.1: a flat cathode surface with a small (1 mm) anode hole.

4.3 New UHV Electron Gun Design

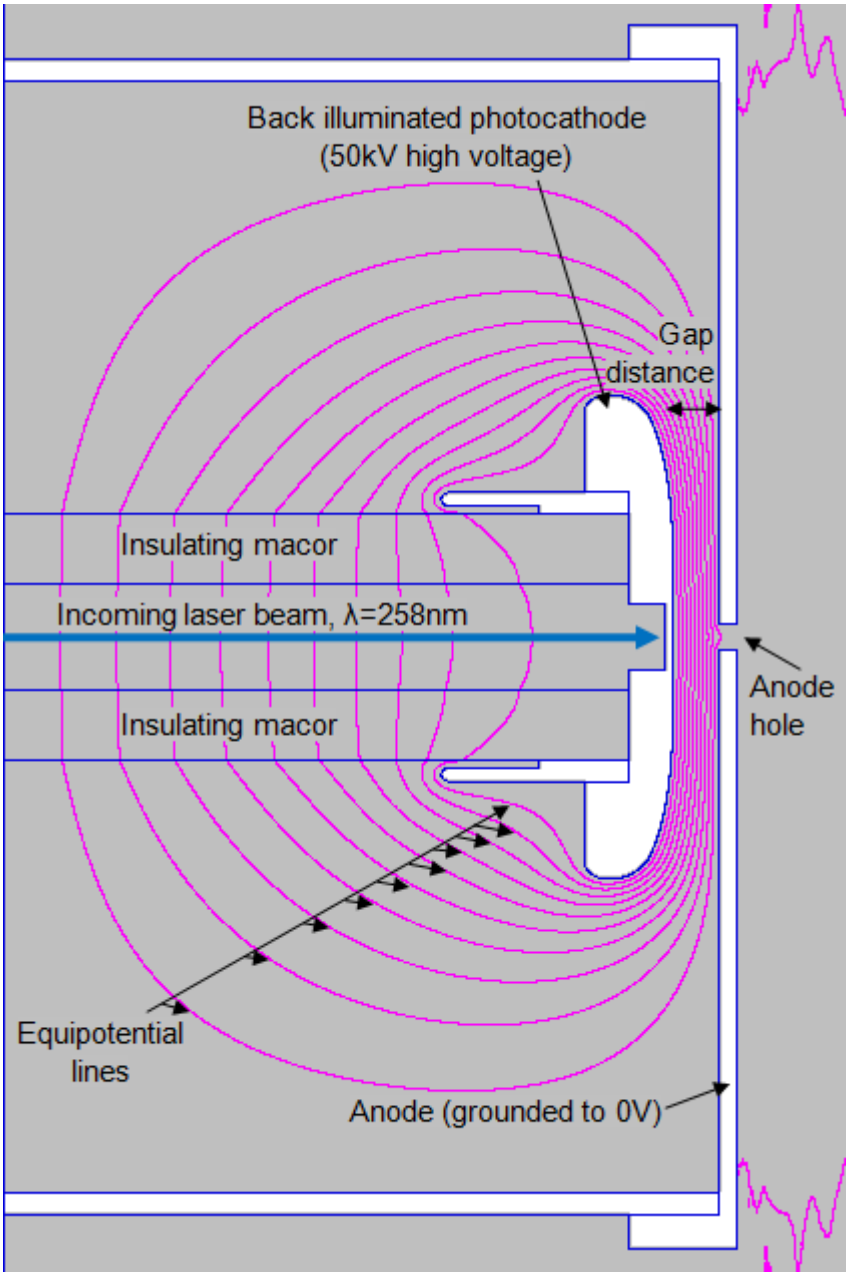

Figure 4.8: SuperFish simulation of the electric field in the new UHV electron gun (cylindrical symmetry around central axis).

Presented in figure 4.8 is the Superfish simulation of the new gun as implemented in the new UHV chamber. Electric field strength along axis of propagation is identical to the old HV gun (fig. 4.3). The only two minor adjustments are:

- The flat area is bigger, and the Rogowski curvature is stretched to twice its size, making fields around that curvature slightly weaker.
- From simulations it was learned that the 'wings' at the side of the old gun (fig. 4.2) are not necessary for staying under the 10MV/m limit, so they are removed.
- The anode cap area is much bigger to accommodate for having the high voltage feedthrough on the front flange.

In figure 4.9, close-up photographs of the physical implementation of the cathode holder with its cathode window are displayed[3].

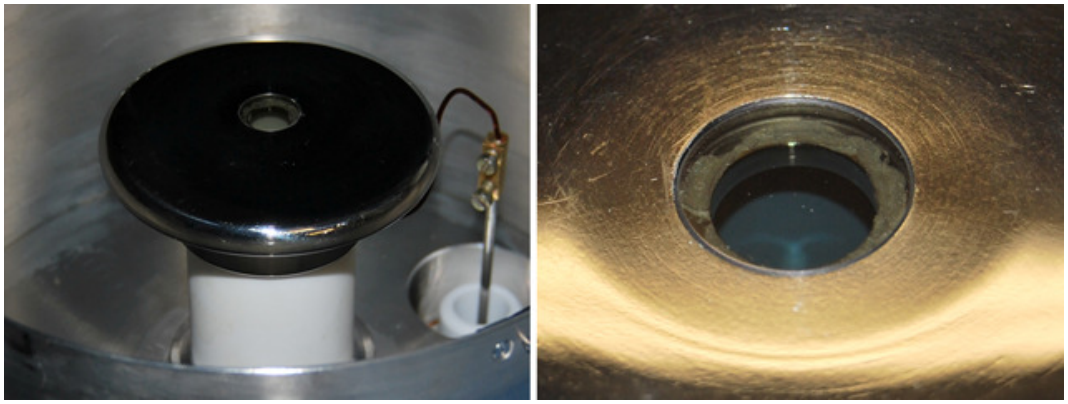

Figure 4.9: Photograph of the physical copy of the simulated gun of figure 4.8 (left) with a zoom-in of the cathode window (right), which is glued into the cathode holder with silver paste such that good electric conduction between the cathode and holder is achieved.

[3]Thanks to Chris Muller from MKH Concept Engineering for producing the stainless steel cathode.

5. Experimental Electron Pulse Characterisation

In this chapter, the electron guns are characterised. With the simulations from chapter 4, numerical values for the electron spotsize (at both sample and detector position) and electron pulse duration can be easily extracted for a whole range of initial conditions such as initial spotsize, electron number and initial pulse duration. In this chapter, we propose how the electron number, spotsize and pulse duration can be experimentally determined and the values for these variables of both the old HV electron gun and new HV electron gun are presented and compared with numerical results. The transverse coherence length of the guns is also calculated from experimental raw data.

5.1 Number of Electrons Per Pulse

In chapter 4 it was established that the number of electrons in a single pulse has a major influence on the characteristics of the pulsed electron beam. So in order to compare numerical and experimental pulse duration results, the electron number per pulse needs to be known. This is achieved by aligning a Faraday cup — which is connected to a pico-ampere meter (*Keithley 6487*) — onto the electron beam. This pico-ampere meter is specified to measure a minimum current of 10 fA. At this resolution, the accuracy is specified to be 0.3% with an offset of 400 fA. The electron number per pulse can be easily calculated from the electron current obtained by the Faraday cup:

$$I_{avg} = PRR \times n \times e \tag{5.1.1}$$

Where I_{avg} is the average current (measured by the pico-ampere meter), PRR the pulse repetition rate (1 kHz for our laser), n the electron number per pulse and e the elementary charge (1.602×10^{-19} C). Typically, FED experiments are performed at 500 – 10.000 electrons in a singe pulse, which corresponds to an electron current of 80 – 1.6 pA. The lower limit is very close to what the ampere meter is specified for. The specified offset of 400 fA (which corresponds to 2.500 electrons) makes our electron current measurements less reliable at low electron number, but the current still measurable. In both the old HV and new UHV chamber, a Faraday cup can be connected to the pico-ampere meter for electron current measurements.

5.2 Spotsize

5.2.1 Initial Spotsize Measurement

One of the inputs for ASTRA is the initial spotsize, which is assumed to be the same as the spotsize of the UV light onto the cathode: only gold that is under illumination of the incoming UV light will generate electrons. For the old chamber, a 300 mm focal length lens is employed to focus the light onto the cathode. Spotsize of the UV focus of the old HV chamber was measured by focusing the UV light onto a phosphor screen[16]. Fluorescence in the phosphor makes the beam visible to the eye. By simply taking a photograph of the fluorescence with a microscope lens, the spotsize of the focused UV light in the old HV gun was determined to be 35 µm[22].

For the new chamber, the gun design is much smaller so a lens with a shorter focal length (and thus smaller spotsize at focus) can be used to focus the light onto the photocathode. In chapter 4 it was determined that smaller initial spotsizes result in higher temporal duration at sample position (figure 4.4d). For a temporal resolved experiment it can therefore be decided to not have the cathode in focus with the UV beam, but it is advantegeous to be able to switch between optimal spatial resolution and temporal resolution.

The spotsize for the shorter focal length lens can easily be calculated with the ideal Gaussian beam waist equations (equations 2.2.2, 2.2.3 and 2.2.4). The validity of these equations needs to be investigated to confirm that the frequency tripled light can still be approximated with a perfect Gaussian beam.

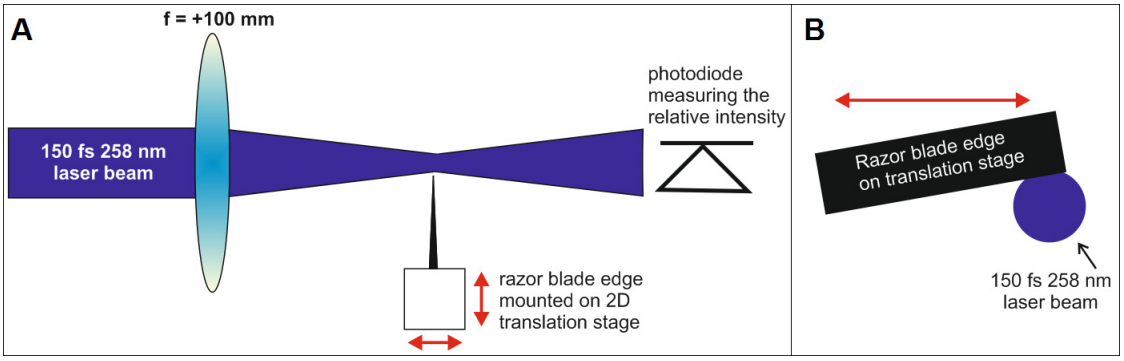

Figure 5.1: (a) Side view and front view (b) of the knife-edge test set-up for measuring focal spotsize of the frequency tripled beam.

The incoming beam spotsize of the UV light hitting lens 'L3' in figure 2.1 is 10 ±2 mm. When employing a 100 mm lens, this corresponds to an angular spread of $\tan^{-1}[(5\text{ mm})/(100\text{ mm})] = 0.05$ rad. For $\lambda = 258$ nm, this corresponds to a beam waist of $w_0 = (258{\cdot}10^{-9})/(\pi{\cdot}0.05rad) = 1.65$ µm (equation 2.2.2), which means a FWHM spotsize of 3.3 µm. The Rayleigh length (equation 2.2.3) is calculated to be $z_R = (258 \cdot 10^{-9})/(\pi \cdot 0.05^2) = 32.8$ µm. To measure the spotsize for a 100 mm focussing lens with $\lambda = 258$ nm, the experimental set-up sketched in figure 5.1 was used. A knife edge was moved into the beam with steps of 0.010 mm. The knife edge is mounted under an angle of 10° (fig. 5.1b) to increase sensitivity: every step of 0.010mm of the translation stage corresponds to an effective step of $\sin 10° \cdot 0.010$ mm $\approx$ 1.7 µm of the razor blade edge. As the beam is stepwise partly covered by the knife edge, a photodiode is monitoring the intensity. The data for the intensity as a function of effective

razor blade edge displacement is shown in figure 5.2a. This data is fitted with the integral of a Lorentzian (equation 5.2.1, because it is easier to obtain than the integral of a Gaussian) and the beam profile of the beam at the position where the measurement was taken is revealed by the derivative of the fit (equation 5.2.2, which in turn results in a Lorentzian).

$$I = \frac{1}{3} \cdot \arctan a \cdot (x - b) + 0.5 \tag{5.2.1}$$

$$\frac{dI}{dt} = \frac{1}{a^2 \cdot (x - b)^2 - 1} \tag{5.2.2}$$

Here, I is the relative intensity (a.u.), x the effective knife edge displacement (mm), a the fitting parameter to adjust the slope and b the fitting parameters to shift the function along the x-axis.

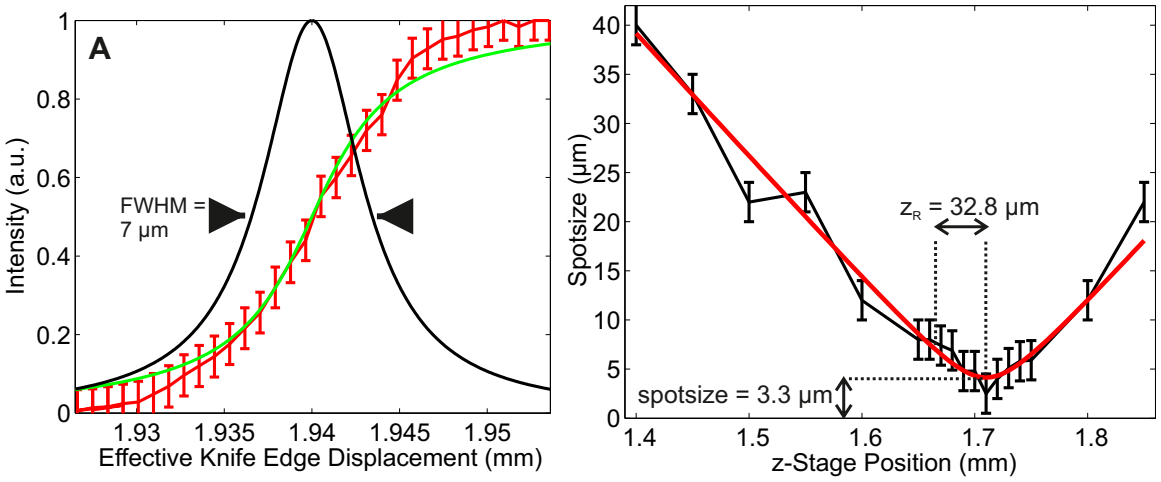

Figure 5.2: (a) Data of the knife-edge test (red) fitted with the integral of a Lorentzian function (green). Beam profile (Lorentzian function) is plotted in black. (b) Spotsize of the UV focus (f = 100 mm) measured with the knife-edge test (black), and a Gaussian spotsize profile fit (red) for the analytically calculated values for w_0 and z_R (w_0 = 3.3 µm and z_R = 32.8 µm).

Beam profiles, like the one plotted in 5.2a were acquired for a whole range of positions close to the focus. Plotting the collection of FWHM spotsizes as a function of z-position that were retrieved from the Lorentzians reveals the beam waist profile, as plotted in figure 5.2b. This method is called the knife-edge test and is commonly used to measure beam profiles. In the same figure (5.2b), the Gaussian beam profile (equation 2.2.4) is plotted with the calculated spotsize of 3.3 µm and Rayleigh length of 32.8 µm. The measurement is in good agreement with the beam profile equation. This means that for the ASTRA simulatons, a value of 3.3 µm for the initial electron beam spotsize could be chosen for a lens of 100 mm.

However, it was chosen to use a 150 mm UV lens instead of the 100 mm for which the measurements from figures 5.2 were performed. Now that the validity of the perfect Gaussion beam profile equation is confirmed, the spotsize of the focus is calculated. The angular spread for a 150 mm lens with an initial beam waist of 5 mm equals $\tan^{-1}[(5\text{ mm})/(150\text{ mm})] = 0.033$ rad. By using equation 2.2.2, the beam waist in case of 150 mm is calculated to be $(258\text{ nm})/(\pi \cdot (0.033\text{ rad})^2) = 2.5$ µm (corresponding to a spotsize of 5 µm). This is the initial spotsize that will be inserted in the ASTRA simulation.

5.2.2 Electron Beam Spotsize at Sample and Detector

Shown in figure 5.3 are two ASTRA simulations for electron beam spotsize as a function of propagation distance for a pulse with 1000 electrons. Both simulations were performed for a voltage of 30 kV on the cathode and a cathode-to-anode gap of 5 mm, which currently is the situation for both guns. For the old gun, an initial spotsize of 35 µm was used and in case of the new gun a spotsize of 5 µm was used. From the figure, a strong initial expansion of the electron beam spotsize in the gun is visible. After having travelled 2 cm, a decrease in spotsize due to the refocussing by the magnetic lens is clearly visible. In the old HV chamber, the travelling distance from gun to detector is roughly 40 cm. This corresponds to an electron spotsize of 0.35 mm at the detector (see dotted lines in figure 5.3). An initial spotsize of 5 µm, which is believed to be the case for the new UHV electron gun, can be focussed tighter. However, the new chamber is bigger. With a gun to detector travelling distance of roughly 55 cm, simulations predict an electron spotsize of 0.33 mm at the detector. The price paid for the small initial spotsize in the UHV chamber is that temporal resolution is expected to be worse. Fortunately we can tune between optimum spotsize and optimum pulse duration by putting the cathode in and out of focus. The electron spotsize at the sample, which sits at approximately 6 – 7 cm from the magnetic lens, is around 200 µm. With a typical aperture diameter of 100 µm glued onto the sample this means that some of the electrons are lost before they hit the detector.

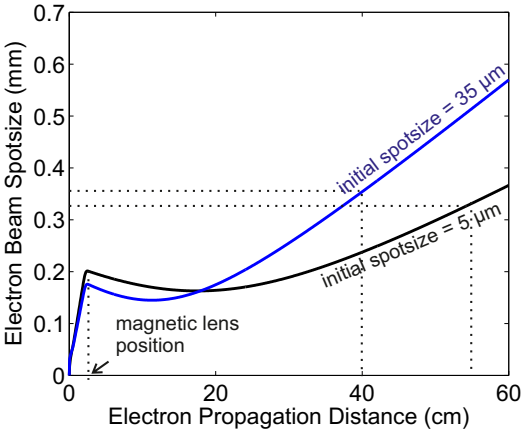

Figure 5.3: ASTRA simulation results for the spotsize of the electron beam as a function of propagation distance for a pulse with 1000 electrons, 5 µm initial spotsize (new UHV electron gun) and a 35 µm initial spotsize (old HV electron gun).

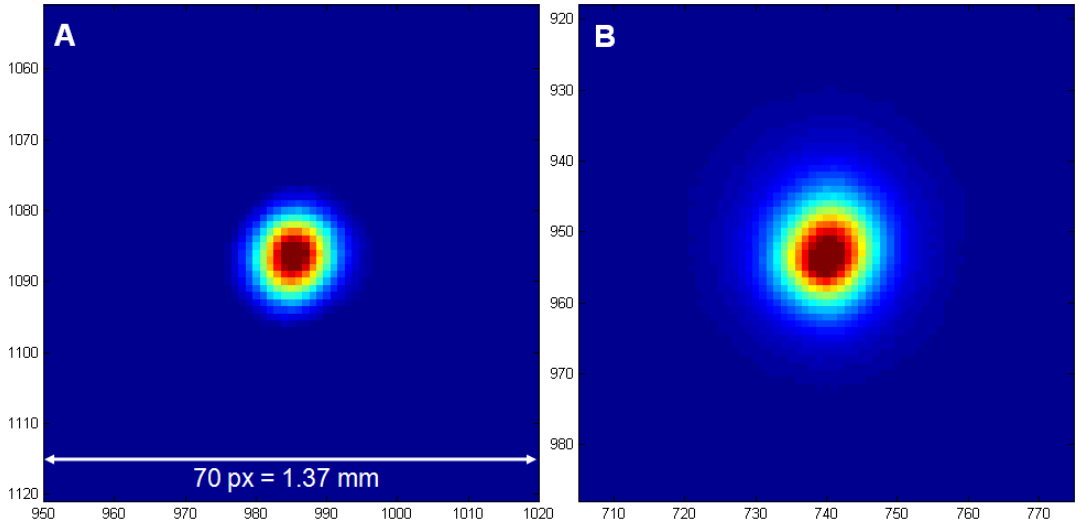

Figure 5.4: (a) Detected electron beam spot in the new UHV chamber. (b) Detected electron beam spot in the old UHV chamber.

Depicted in figure 5.4 are the electron beam spots at the detector when the UV light is

focused on the cathode for both the new UHV (fig. 5.4a, unknown electron current) and the old HV gun (fig. 5.4b, 1000 electrons per pulse). In both cases, the spotsize was minimised by adjusting the magnetic lens. In figure 5.5, a lineout through the center along the smallest spotsize axis (red curve) and the longest spotsize axis (blue curve) are shown for both the new UHV (fig. 5.5a) and the old HV gun (5.5b) revealing the beam spot profiles for both beams. For the new UHV gun, a spotsize of 0.13 mm is measured. The spotsize of the old HV gun is measured to be 0.18 – 0.23 mm. Surprisingly, the detected electron beams are smaller than what the simulations predicted, but as expected the new electron gun produces a smaller electron spotsize due to reduced UV-beam spotsize on the cathode.

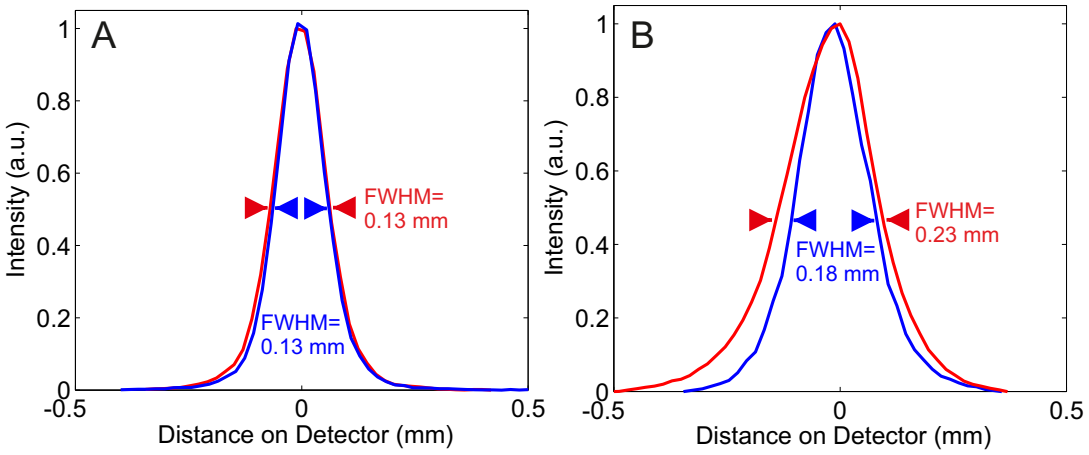

Figure 5.5: Detected electron beam spot profile along shortest (blue curve) and longest (red curve) axis for the (a) new UHV chamber and the (b) old HV chamber.

The disagreement between simulation and experiment (a factor of 1.5 - 2.5) can be due to the simulation of the magnetic lens or probably an overestimation of initial spotsize and an underestimation of the electron number, as will be pointed out in the next section. However, temporal resolution is the more crucial variable for FED and spotsize has shown to not have a big effect on temporal resolution in any case[1]. For example, in the calculations in [20] the spotsize was assumed to be constant. Reducing or increasing the magnetic lens current only has minor effects on the temporal duration of the electron pulses. The minor discrepancy between experiments and simulations does thus not invalidate the results for electron pulse duration.

5.3 Electron Pulse Duration

In chapter 4 the undesirable effect of initial energy spread and space charge effects on the temporal resolution of our experiments was discussed. Having shown literature and simulation results it was pointed out that a technique to directly measure such pulse durations is advantageous to experimentally characterise time resolution of the FED set-up. In practise the upper limit for the temporal duration during an FED experiment is determined by the fastest dynamics observable. However, a flexible technique to look at the temporal duration along the entire electron beam line for different electron currents would allow one to compare experimental results with analytical models in literature or with simulations such as the one in figure 4.4.

[1]Spotsize of the beam once it has left the gun does not have a significant effect on pulse duration. As discussed, *initial* spotsize does have an effect on temporal duration.

An accurate (sub-100 fs) and relatively simple experimental technique that was used to make this comparison is a crosscorrelation of electron pulses with short laser pulses[42]. When a laser pulse interacts with an electron pulse, the ponderomotive force exerted on the electrons distort the electron beam shape. The electrons are then pushed away from intense field and driven towards lower fields. Higher local electron charge density results in stronger scattering when being exposed to a strong laser field. In this manner, deformations in the electron beam upon laser impact reveal the electron density. By controlling the arrival time of laser pulse impact on the electron pulse with a mechanical delay stage in the optical path, the electron spot distortion can be measured as a function of time and the pulse duration can be determined with around 100 fs accuracy[43]. Two counterpropagating laser pulses that meet the electron beam at the same time has increased sensitivity significantly. Electron pulses in such a standing wave field generate strong streaks instead of minor deformations[44]. This implementation is more complicated as the moment of impact must now be controlled by two delay stages such that they meet the electron pulse at the same time. By using this method, a recompressed electron pulse of 334 fs was measured for $6.24{\cdot}10^5$ electrons/pulse[44]. Despite this technique having shown to be very effective, it is highly impractical to measure the electron pulse durations at many positions to map out the electron dynamics along the electron beam line for comparison with theory. Furthermore, it is not possible to measure pulse durations before or during measurement without major disruption of the experiment.

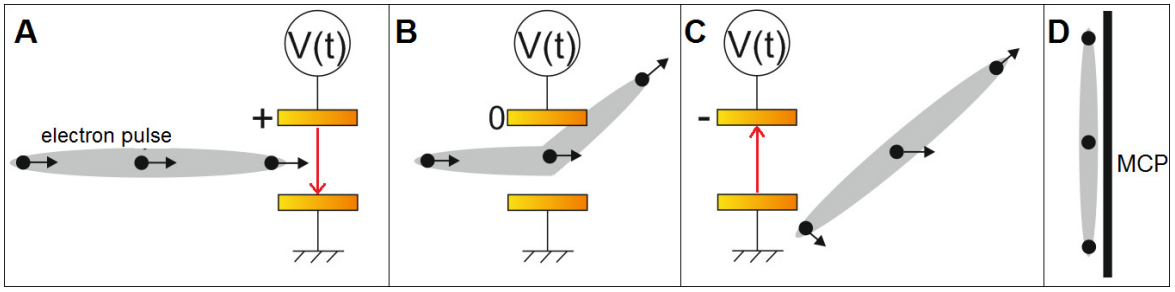

Figure 5.6: Conceptual sketch displaying an electron pulse travelling through a streak camera. Three electrons per pulse are highlighted for reference. Direction of those electrons are indicated with a black arrow, and the direction of the electric field in the cavity is indicated with a red arrow. The fast changing electric field spatially streaks temporal electron pulse features.

A second experimental technique that has shown to be effective in measuring electron pulse durations is a streak camera. The concept of a streak camera is explained in figure 5.6. The electron beam is aligned through two cavity plates that are positioned parallel to the beam. The plates are subjected to a fast oscillating voltage (around 5 GHz) generating an oscillating electric field in between the cavity plates. The applied voltage changes so fast that when an electron pulse travels through the cavity, electrons at different positions in the pulse experience different electric fields, resulting in dispersion of the picosecond pulse. If this oscillation is synchronised with the electron pulse, the following scenario can happen: as the first electron travels through the cavity, it experiences a force upwards (fig. 5.6a). As the pulse is traveling through the streak plates, the polarity switches such that the electrons in the center of the electron pulse do not experience an electric field (fig 5.6b) and the electrons in the tail of the pulse experience a force downwards (fig 5.6c). This results in temporal information being spatially streaked on the detector (fig. 5.6d). Big advantages of this technique compared to the crosscorrelation are that it is experimentally easier to measure pulse durations along the beam line, and the generated streak contains temporal electron densities allowing for more

exploratory data analysis[10]. Furthermore, due to the oscillating field being photo-initiated, the jitter is better. The physical realisation of a streak camera is shown in figure 5.7.

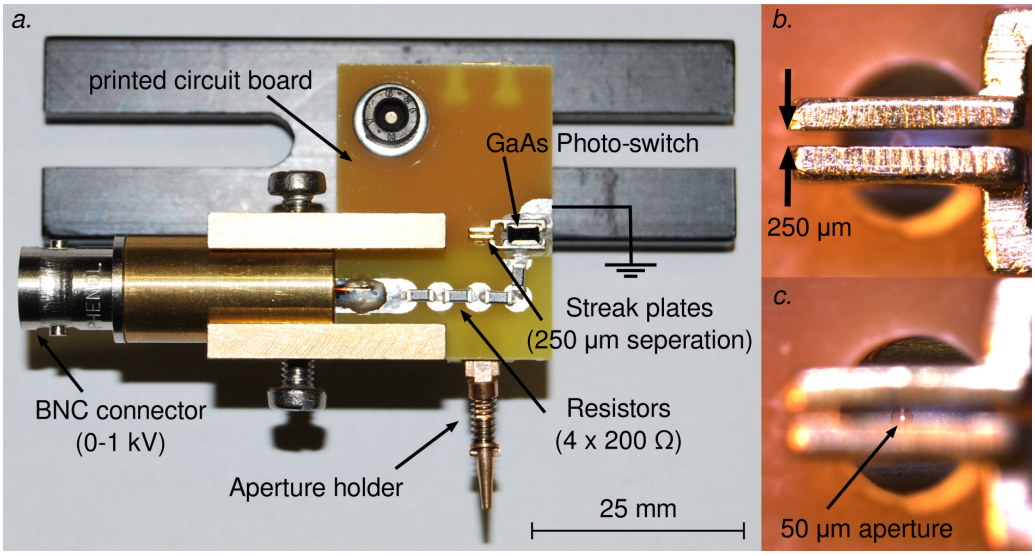

Figure 5.7: (a) Photograph of the streak camera. (b) Close-up of front view of the streak camera. Electrons travel out of the page after having passed through an aperture behind the streak plates (c).

The electron pulse should be synchronised with the oscillating field in such a way that the voltage gradient $\frac{dE}{dt}$ is maximum when the pulse passes so that maximum dispersion and thus highest streak sensitivity is achieved. This is achieved by initiating the voltage oscillation (driven by an RLC circuit) optically: a Gallium Asenide photoswitch becomes conductive upon photoexcitation by a femtosecond pulse (with pulse energy of 50 µJ). Synchronisation is accomplished by using the laser pump beam to close the RLC electronic circuit by means of the photo-switch to start the oscillation of the electric field between the two streak plates. Depending on where in the oscillation the electrons pass the cavity, the beam shows a deflection on the detector. By monitoring the deflection as a function of pump pulse delay, the entire electric field oscillation can be mapped out. This oscillation is shown in figure 5.8. During an experiment on a sample, observing this oscillation also serves to find $t = t_0$ (time of pump impact). The position in the oscillation at which the streaks are acquired is indicated with $(\frac{dE}{dt})_{max}$. At this position, the dispersion is maximum and thus the resolution of the streak camera is optimal.

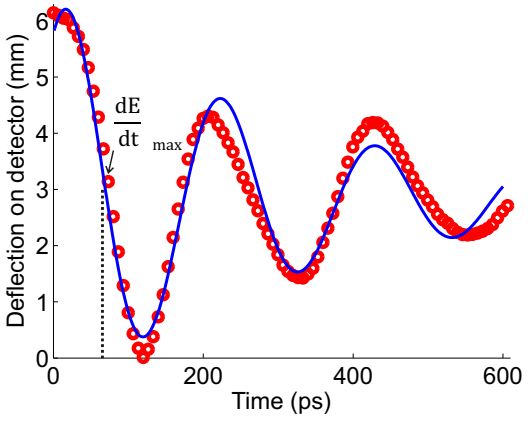

Figure 5.8: The measured deflection of the electron beam that travels through the streak cavity plates as a function of photo-switch pump delay time (red circles) plotted with a fit for the damped oscillator model (blue line).

Streak cameras have been employed to measure pulse durations[45], and these streak measurements have been compared to theory. In fact, the paper cited in chapter 4 which compared

experimental pulse durations with theory used a streak camera[29]. Its appeal lies in it being compact and flexible. Biggest limitation of those streak cameras used is their low streak sensitivity. Streak sensitivities of 250 fs/pixel for a 5.5 kV/ns voltage ramp across the streak plates has resulted in a 500 ps long error bar. With temporal resolutions of 300 – 500 fs at sample position, improvement of temporal resolution is needed. The streak camera shown in figure 5.7 is this improved model. Higher voltages (800 V) can be ramped across the streak plates that are placed closer together (streak plate separation of 250 µm), increasing its sensitivity[46]. The higher electric fields generated between the plates is possible because of the absence of a constant voltage applied to the streak plates. Only a short 30 ns high voltage pulse that is synchronised to the repetition rate of the laser is applied to the cavity plates. It is on this high voltage pulse that the damped oscillation is initiated. Introducing these pulses instead of a DC voltage on the streak plates reduces the probability of arcing across the photoswitch as well as instabilities due to charching of the streak plates under a constant voltage. Our ramp is around 8 kV/ns as opposed to the 5 kV/ns that was reported for the DC version of the streak camera. However, due to the reduced streak separation the streak camera has an improved temporal resolution of 150 fs (2.1mm/ps corresponding to around 10 fs/px as opposed to 250 fs/px)[46; 29].

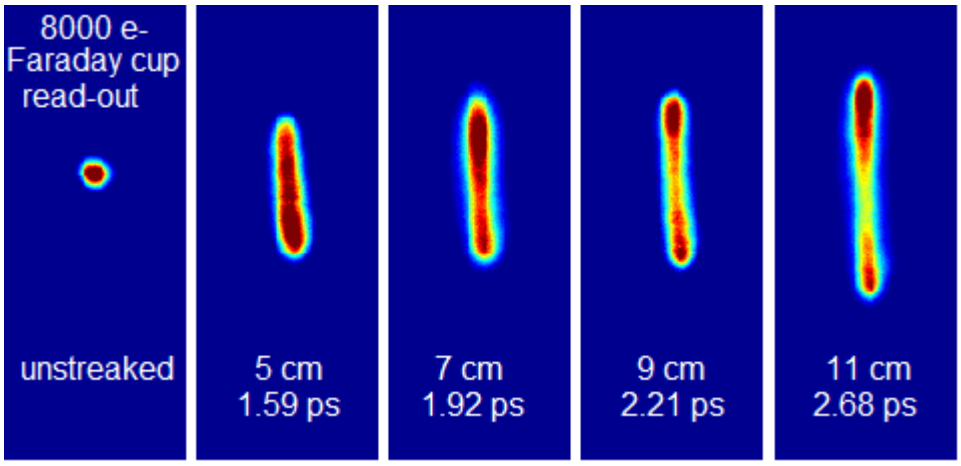

Figure 5.9: An electron beam with a Faraday cup read-out of 8000 electrons per pulse shown both unstreaked and streaked by the streak camera for four different distances from the electron gun.

Figure 5.9 shows streaks at four different streak camera positions along the electron beam axis for a single electron number, showing the flexibility and mobility while performing streak measurements. Streak velocities can be easily calculated from oscillations like the one in figure 5.8. The length of the streaks can be related to the electron pulse duration using the obtained streak velocity, which ultimately resulted in the experimental pulse durations mentioned in figure 5.9.

5.3.1 Temporal Resolution in the Old HV Chamber

Depicted in figure 5.10a are simulation and experimental results for pulse duration as a function of propagation distance. For the simulations, initial conditions were chosen as they were measured for the old chamber: 35 µm initial spotsize, 150 fs initial pulse duration and a 30 kV voltage on the cathode with a 5 mm anode-cathode gap. Streak measurement with the streak camera at 5 cm, 7 cm, 9 cm and 11 cm distance from the electron gun were performed with a

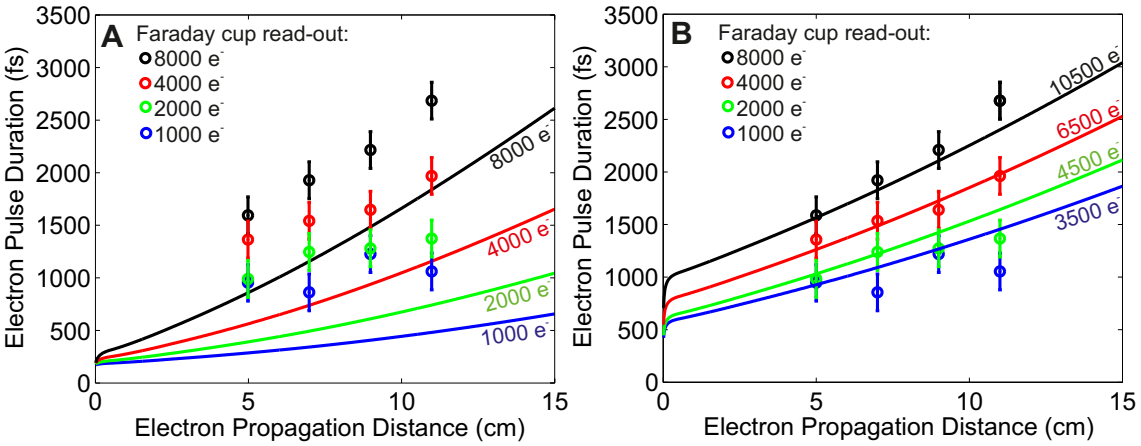

Figure 5.10: (a) Experimental pulse durations with simulations for initial spotsize = 35 µm, t_0 = 150 fs, and electron number = 1000, 2000, 4000 and 8000. (b) Experimental pulse durations with simulations for initial spotsize = 10 µm, initial pulse duration = 220 fs, electron number = 3500, 4500, 6500 and 10500.

Faraday cup electron current reading that corresponds to 1000, 2000, 4000 and 8000 electrons per pulse. The simulated pulse durations are significantly shorter than the measured pulse duration in figure 5.10a. For a sample that would typically sit at a distance of 7 cm behind the gun, a temporal duration of 0.95 ps was measured for 1000 electrons per pulse. From the simulation, a value of 0.34 ps was obtained. We assign the discrepancy between measurement and simulation to the following three reasons:

- In section 5.1 it was explained that the pico-ampere meter has an offset of 400 fA at the low electron currents that we measure. By using equation 5.1.1 this corresponds to an offset of 2500 electrons per pulse.
- A spotsize at focus of 35 µm was measured, but by using equations 2.2.2 and 2.2.3 the analytical spotsize of a 258 nm wavelength UV beam with incoming spotsize of 10 mm for a 300 mm lens corresponds to 10 µm for a perfect Gaussian beam.
- Our laser is specified to emit pulses of 150 fs temporal duration which was chosen to be the initial pulse duration used for our simulations. In reference [46], the evolution of the pulse duration of the frequency tripled light at the cathode after having travelled through the various optics (crystals and dispersive media) was simulated to be around 220 fs.

The simulations plotted in figure 5.10b are for the initial conditions that compensate for the three points mentioned. An initial spotsize of 10 µm, initial pulse duration of 220 fs and an offset of 2500 electrons per pulse were used as conditions for these simulations. These new initial conditions are experimentally reasonable assumptions and show a good overlap with the experimental data.

5.3.2 Temporal Resolution in the New UHV Chamber

Shown in figure 5.11 are the initial experimental temporal characterisation results that were obtained with a streak camera for the new UHV gun that was presented in chapter 4. For the ASTRA simulations, the following initial conditions were used. Again, the cathode is at 30 kV (in the near future this high voltage source will be replaced allowing us to go up to 50 kV which will improve temporal resolution) with a cathode-anode gapsize of 5 mm. The

calculated initial spotsize is 5 µm and the initial pulse duration is 220 fs. The simulations were performed for 3500, 4500, 65000 and 10500 electrons. Assuming the specified offset of 400fA in the pico-ampere meter, this corresponds to a 1000, 2000, 4000 and 8000 electrons experimental read-out of the Faraday cup. This temporal characterisation is expected to improve significantly when a bigger initial spotsize is chosen and when a higher voltage is applied to the cathode.

5.4 Transverse Coherence Length

The spatial resolution that our electron beam can resolve must be better than the atomic structure in order to observe atomic displacements. In other words: the transverse coherence length must be larger than the lattice constants that we want to measure. The $Cu(DCNQI)_2$ crystals, for which the new FED set-up will be used, have a lattice constant of $c = 3.8$ Å[25]. In the proposed experiments of chapter 3, a trimerisation in along the c-axis must be measurable, which corresponds to a period of $3 \cdot 3.8 = 11.4$ Å. Longest period that needs to be measured is $a = b = 22.4$ Å, which sets the requirement for the transverse coherence to be more than that. The lower limit of coherence length can be estimated by measuring the distance d between Bragg diffraction spots in a diffraction pattern as well as its FWHM Bragg spotsize Δd. Because of the diffraction patterns being in reciprocal space, the distances d are related to the inverse of the real space lattice constants a and c. Similarly, the width of the diffraction peaks is related to the inverse of the lower limit of the coherence length $L_\perp$[32]:

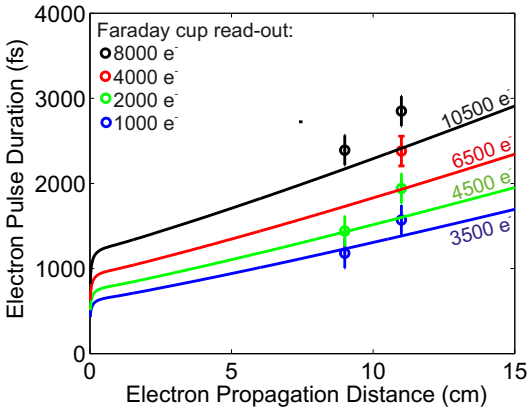

Figure 5.11: Measurements of pulse duration for the new UHV electron gun for different electron numbers, plotted with simulation for electron pulse duration with the appropriate initial conditions: initial spotsize = 5 µm and $t_0 = 220$ fs.

$$L_\perp = a \cdot \frac{d_{a^*}}{\Delta d} = b \cdot \frac{d_{b^*}}{\Delta d} \tag{5.4.1}$$

$$L_\perp = c \cdot \frac{d_{c^*}}{\Delta d} \tag{5.4.2}$$

Plotted in figure 5.12 are the line-outs across the diffraction peaks as indicated in in the diffraction pattern. This is the same diffraction pattern shown in figure 3.3. By looking at the lattice constant c, a lower limit for the coherence length $L_\perp = 3.8\text{Å} \cdot (5.84mm/0.25mm) = 8.9$ nm is obtained. Similarly, By looking at the lattice constant $a = b$ (fig. 5.12c), a lower limit for the coherence length $L_\perp = 22.4\text{Å} \cdot (1.07mm/0.25mm) = 9.6$ nm is obtained for the old HV chamber. This coherence length is significantly longer than the longest atomic period of 2.24 nm and thus good enough to resolve this periodicity.

Shown in figure 5.13 is a diffraction pattern of a $Cu(DCNQI)_2$ sample in the new UHV chamber. Of course, this pattern doesn't look as good as the pattern from the old HV chamber in figure 3.3 which is a highly averaged pattern of the best sample that was achieved ever during two years of sample growing, cutting and taking diffraction patterns. The pattern shown in 5.13 is the first diffraction pattern taken ever in the new UHV vacuum which happens to be of poor sample quality. Therefore, the diffraction pattern quality does not necessarily say

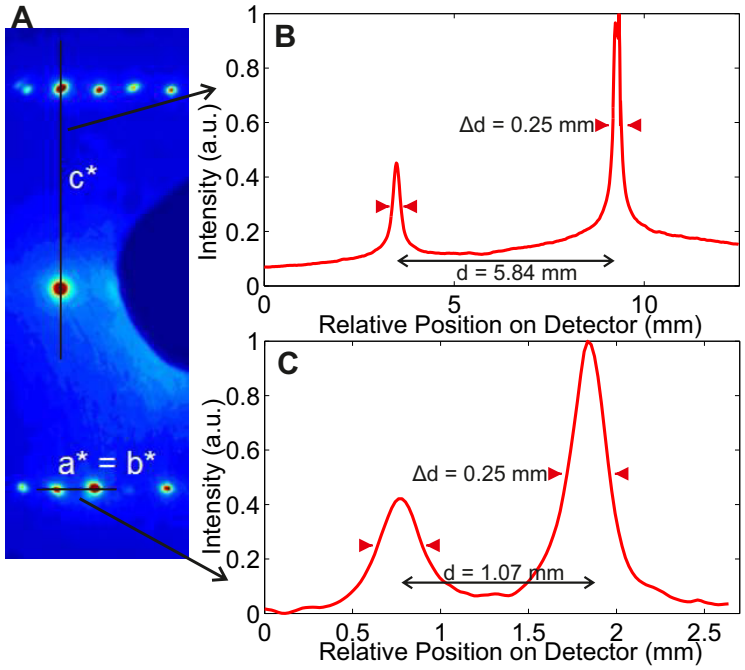

Figure 5.12: (a) A room temperature $Cu(DCNQI)_2$ pattern displaying the intensity line-outs along c^*-axis and $a^* = b^*$-axis that are plotted in (b) and (c) respectively.

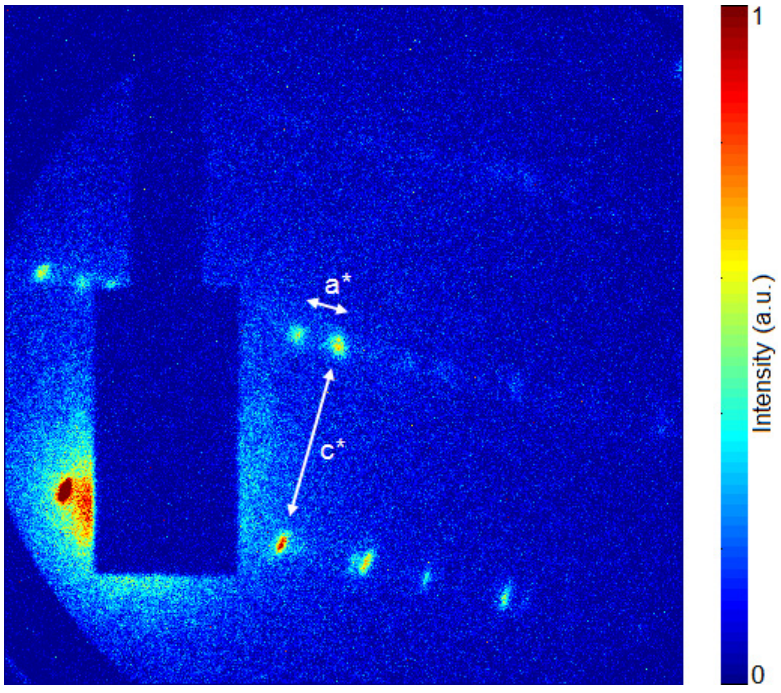

Figure 5.13: A room temperature $Cu(DCNQI)_2$ electron diffraction pattern acquired with the new UHV FED set-up. Single pattern (60 s exposure time), unknown electron number.

anything about the functioning of the gun. What it does show however is that the gun in principle works and that it can take diffraction patterns of $Cu(DCNQI)_2$ samples. Note that the diffraction peak separation in figure 5.13 is bigger than in figure 3.3. This is due to the larger sample-to-detector distance in the new chamber (around 50 cm as opposed to around 35 cm in the old chamber). Both guns currently operate at 30 kV meaning that the diffraction angles are identical, explaining the bigger diffraction peak separations. Once a 50 kV high voltage source is available for the new chamber (which is the voltage on which the gun will operate) more diffraction peaks will be visible on the detector due to reduced Bragg peak spacing.

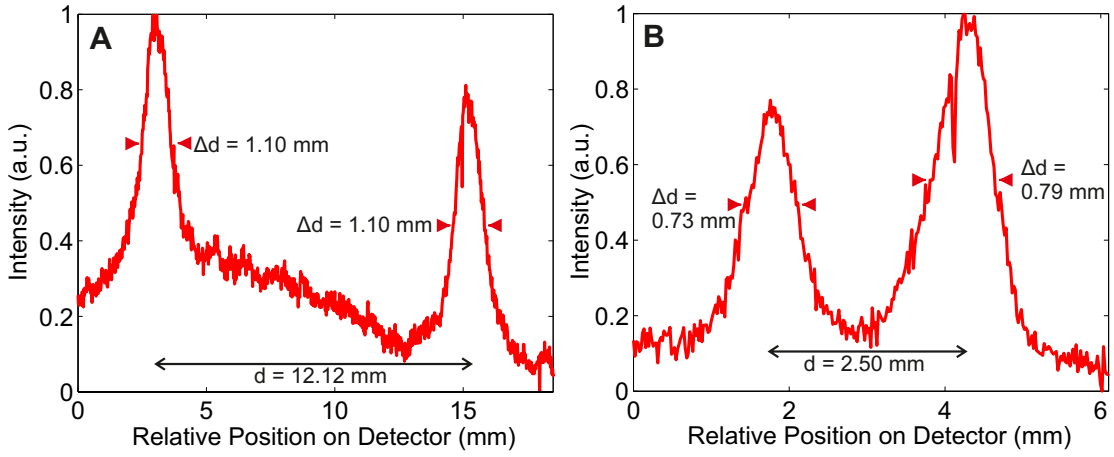

Figure 5.14: Spotsize and separation of Bragg peaks from new UHV gun acquired diffraction pattern taken along (a) c^*-axis and (c) $a^* = b^*$-axis

Shown in figure 5.14 are the line-outs as indicated in figure 5.13. By looking at the lattice constant c^* (fig. 5.14a), a lower limit for the coherence length $L_\perp = 3.8$ Å$\cdot(12.12mm/1.10mm) =$ 4.2 nm is obtained. Similarly, By looking at the lattice constant $a = b$ (fig. 5.14b), a lower limit for the coherence length $L_\perp$ =22.5 Å$\cdot(2.50mm/0.76mm) = 7.4$ nm is obtained for the new UHV chamber. This coherence length is also significantly longer than the longest atomic period of 2.24 nm and thus good enough to resolve atomic structure.

This first result for the lower limit of the coherence length (7.4 nm) for the new UHV electron gun is very promising as it is already very close to the lower limit of 9.6 nm that was obtained for the old HV electron gun. Diffraction peaks in figure 5.4a have a deformed shape due to a 'scew' electron spotsize caused by damages on the cathode. Also, diffraction pattern quality (and spotsize of the diffraction spots) differs greatly from sample to sample depending on its quality (see appendix A.1 for examples of diffraction patterns with 'bad' Bragg spots). The effect of polycrystallinity within a sample, as well as the sample not having a smooth, but rather 'wavy' surface results in diffraction spots to be 'smeared out'. The newly acquired diffraction image of figure 5.14 is an example of this. Besides, simulations of the electron spotsize in section 5.2 have shown that in fact the electron spotsize at the detector in the new chamber can expected to be smaller because of the shorter UV lens, which will improve the coherence length (but worsen temporal resolution). By using a shorter focal length UV lens in the new gun, we are more flexible to choose between optimum transverse coherence length (spotsize) or optimum temporal duration. This flexibility in the old gun is limited due to its big design whereby employing a UV lens of a focal length of shorter than 300 mm is

not possible.

The statement of improved spatial resolution is confirmed by a second diffraction pattern shown in figure 5.15. This is a pattern of a $TiSe_2$ slice (thicknes of a few tens of nanometers). The lattice constant of this hexagonal crystal structure is 3.54 Å[47]. By inserting the information for FWHM and diffraction peak seperation from figure 5.15 into equation 5.4.2, a transverse coherence length of $L_\perp = 3.54$ Å$\cdot(9.3mm/0.30mm) = 11.0$ nm is obtained. This is an improvement compared to the old system.

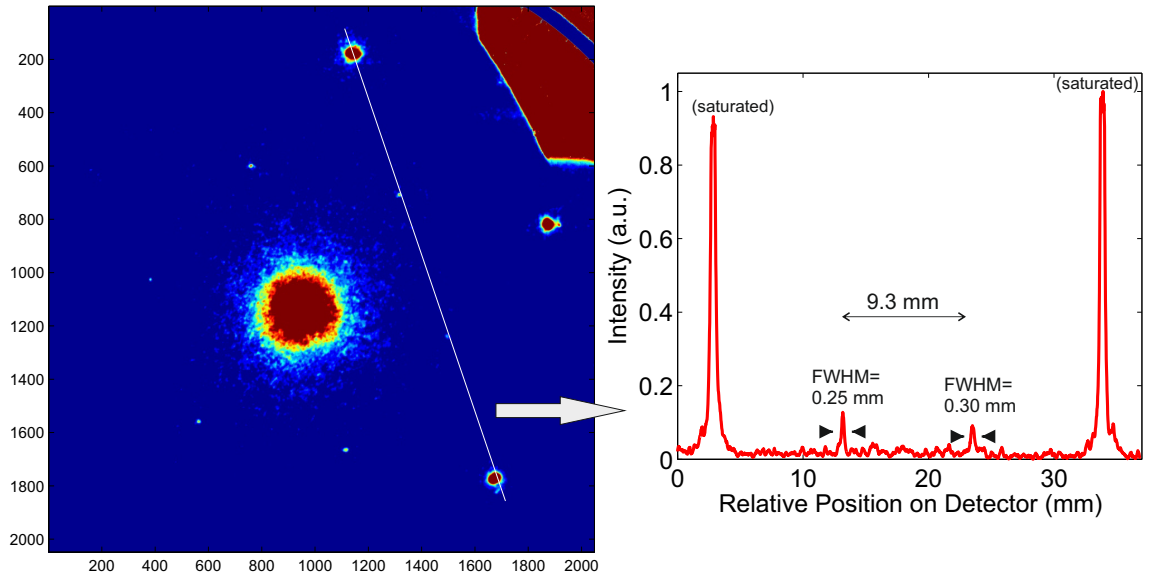

Figure 5.15: Single electron diffraction pattern of $TiSe_2$ (60 s exposure time), acquired with the new UHV FED set-up (zero-order diffracted beam unblocked). The electron intensity along the white line in the pattern is plotted on the right, with FWHM diffracted Bragg spotsizes and spotsize seperation indicated.

6. Recompression of Temporally Broadened Electron Pulses

In section 4.1, three alternative FED techniques were outlined to get around the limiting electron debunching effect. It was also pointed out that these methods have complications. Fortunately, post-manipulation of electron bunches in the 'conventional' way of performing FED is possible. Potential techniques for post-electron generation compression are highlighted in this chapter. Numerical results for a simple and compact compressor are presented, showing the potential for improvements in temporal resolution in our set-up. The chapter is concluded with a preliminary experimental result.

6.1 Electron Pulse Compressors

For recompression of high energy electron pulses (100 keV – 1 MeV) an achromatic bending magnetic system can be employed[48]. Magnetic pulse compression and energy selection of electrons are accomplished by aligning the electron beam through two permanent dipole magnets which give the beam a total bending angle of 360°. The circular path of electrons with high energy have a larger radius, resulting in the slower electrons with a lower electron energy (and thus smaller travelling radius) to 'catch up'. Desired electron energies can be selected by placing a slit at the magnetic compressor output. By employing this technique, a pulse duration of around 500 fs was measured (determined by utilising ponderomotive scattering upon laser beam interference) for a pulse of 6 fC (corresponding to 35.000 electrons). The electron number was enough to resolve an Au diffraction pattern in a single shot. Advantages are that magnetic compression only employs static fields which might make its implementation and stability easier than radio frequency compression that will be discussed.

Dr. Günther Kassier, a former group member, has published a paper that numerically describes a similar system where an electric reflectron bends electrons with an angle of almost 180°[49]. The reflectron generates an uniform electrostatic field acting as a dispersive electron mirror. The same self-compression principal due to faster electrons travelling with a higher radius applies. A theoretical recompression of a pulse with 200.000 electrons to a 130 fs pulse duration with a rms pulse radius of 140 µm is demonstrated by using SuperFish and ASTRA simulation software. However, this approach has never been experimentally implemented.

An alternative method is to, rather than recompressing broadened electron pulses, have a detection system that is only sensitive to a narrow bandwidth from the entire electron energy spectrum[50]. As pointed out, debunched electron pulses have a linear chirp, meaning that short temporal slices in an electron beam have narrowband electron energies. By employing an energy analyser, 30 fs domain of resolution temporal slices could be selected. This has not been achieved experimentally yet.

The most commonly used method for compression is a radio frequency (RF) cavity[51]. The principle behind these RF compressors are similar to the streak camera principle that was sketched in figure 5.6, but now the cavity is placed perpendicular to the incoming electron beam, with an entrance and exit hole (figure 6.1a). In this case, with the appropriate phase, electrons at the front of the bunch get decelerated, and electrons at the back of the bunch get accelerated. Such a compressor that effectively reverses the kinetic energy distribution acts

like a 'temporal lens' and has a certain focal length. The kinetic energy distribution reverse in the electron pulse should not be too strong as it will give the electron pulse a higher energy distribution. Having such a 'polychromatic' electron beam results in a high standard deviation of de Broglie wavelength, ultimately leading to diffraction peaks to be less well resolvable. The temporal focussing can be mapped by moving a streak camera along the beam line, as sketched in figure 6.1b.

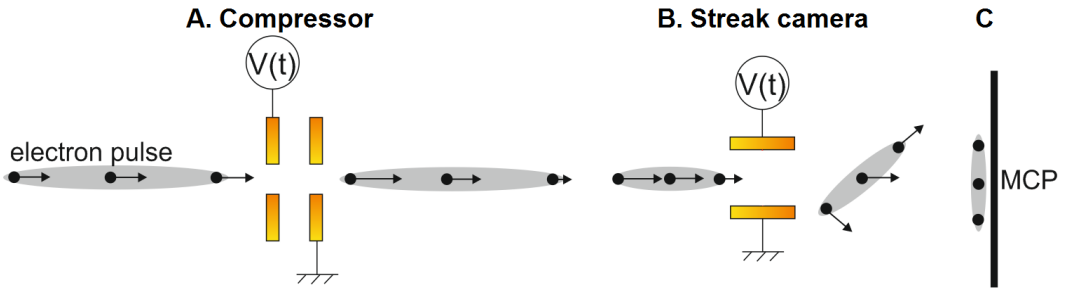

Figure 6.1: Sketch of an electron beam being compressed by a compressor (a) and streaked by a streak camera (b) onto the detector (c). Three electrons are highlighted for reference. Black arrows illustrate velocity of the highlighted electrons.

Most tricky experimental challenge for an RF compressor is the synchronisation of the phase of the RF oscillation in the cavity with the electron pulse. Maximum compression is achieved for highest $\frac{dE}{dt}$ and this synchronisation must be stable to prevent jitter from worsening the temporal resolution. The arrival time of the electrons is extremely sensitive to the phase of the RF oscillation that works at a frequency of 3 GHz[52]. Synchronisation is achieved by locking this oscillation to a high harmonic coming from the laser oscillator to the voltage controlled oscillator. The amplified voltage from this oscillator drives the RF cavity. Crucial is that the phase is tuned such that the central electron in a pulse is at the centre of the cavity when the phase of the oscillation is zero which results in inherent difficulty. Nevertheless, great successes have been booked with this RF compression system: 200 fC charge with 95 keV kinetic energy (around $1.2{\cdot}10^6$ electrons) have been compressed to 430 fs temporal duration[52]. Furthermore, a 100 fs duration for 200 fC charge ($1.2{\cdot}10^6$ electrons) with around 80 fs jitter has been measured [51] and 100 pC – 600 pC charge ($6.25{\cdot}10^5$ electrons – $3.6{\cdot}10^6$ electrons) with temporal durations in the range of 334 fs – 500 fs have been measured[44]. Despite the RF-compressor making FED experiments far from straightforward, it seems that this technique has sorted out the electron debunching limitation. Some of the most recent outstanding FED results (that were already mentioned in the introduction) on the opening and closing of a cyclisation-ring in diarylethene[11] and the molecular sliding, bending and movement in EDO-TTF[12] have been performed with RF-compressed pulses.

In our group, an alternative method for achieving synchronisation between the electric field in the compressor cavity and the electron pulse was developed by Dr. Günther Kassier[53]. This principle is based on the streak camera that was shown in figure 5.7. Again an oscillation driven by an RLC circuit supplied by a 30 ns high voltage pulse is photo-triggered by a laser pulse by means of a GaAs photoswitch, generating a fast changing electric field between two streak plates. In the case of the compressor, these compressor plates are mounted perpendicularly to the beam as depicted in figure 6.1a. Employing the pump-pulse to photo-trigger the oscillation for synchronisation is easier and cheaper to achieve as no complicated high accuracy electronic machines are required. In a proof-of-principle paper, an electron pulse of

260.000 electrons (20 keV electron energy) was recompressed to 750 fs and a pulse with 15.000 electron pulses was recompressed to 200 fs (stable over 24 hours).

This simplified approach of a compressing cavity is promising, but we haven't performed a recompressed time resolved measurement yet. The first prototype is big, bulky, and has two GaAs photoswitches requiring two pump paths to trigger both switches with zero delay. Combining electron pulse compression experiments with a time resolved FED measurement is a mission: a total of three pump arms are needed (two for the compressor, one for the sample) which all need to enter the vacuum chamber and be aligned onto their target (sample and photoswitches). On top of that, the timing of all three pulses needs to be carefully controlled. To accommodate for the experimentally needed simplicity, Dr. Nicolas Erasmus designed the compact compressor shown in figure 6.2. This design is close-to identical to the streak camera except for the orientation of the streak plates. Only a single photoswitch is employed.

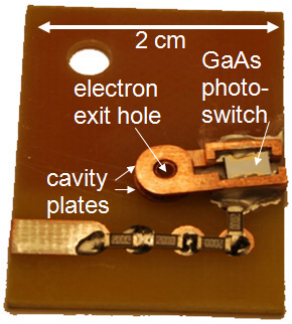

Figure 6.2: An attempt for a small compressor (design by Dr. Nicolas Erasmus).

6.2 Numerical Results for a Compact Compressor Design

The electrostatic field generated by the two cavity plates of the compressor in figure 6.2 are simulated in SuperFish. A plot of the equipotential lines of this simulation is shown in figure 6.3a. A line-out of the electric field strength at the center along the electron beam line is plotted in figure 6.3b. Again, this electric field strength as a function of distance serves as an input for ASTRA. But unlike the electron gun, the compressor is not subjected to a DC voltage but an oscillating voltage. In ASTRA, the static imported field can be programmed to oscillate, and the phase relation with respect to the electron pulse can be chosen. The oscillation frequency was set to 4.5 GHz.

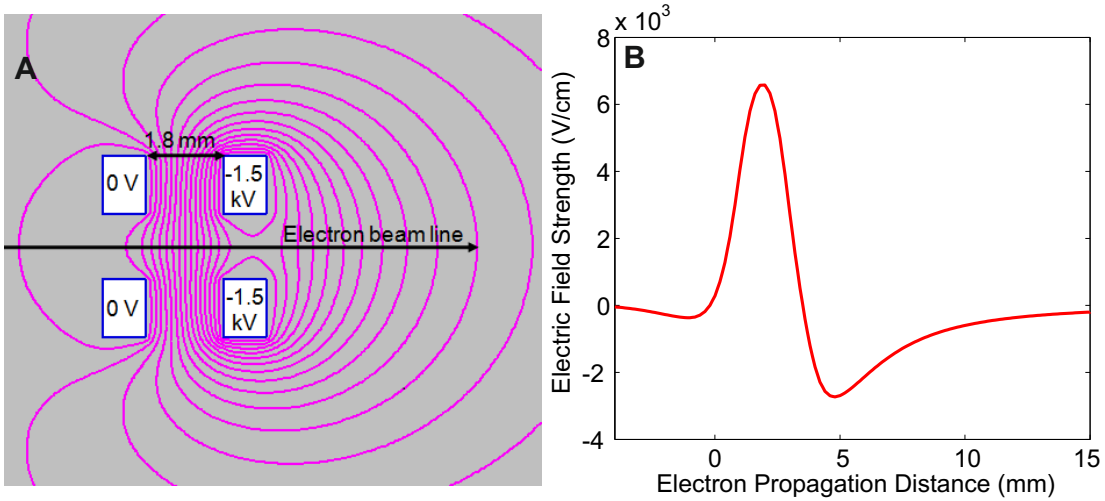

Figure 6.3: (a) Plot of the equipotential lines in the compressor cavity. (b) Electric field strength along electron beam line through cavity.

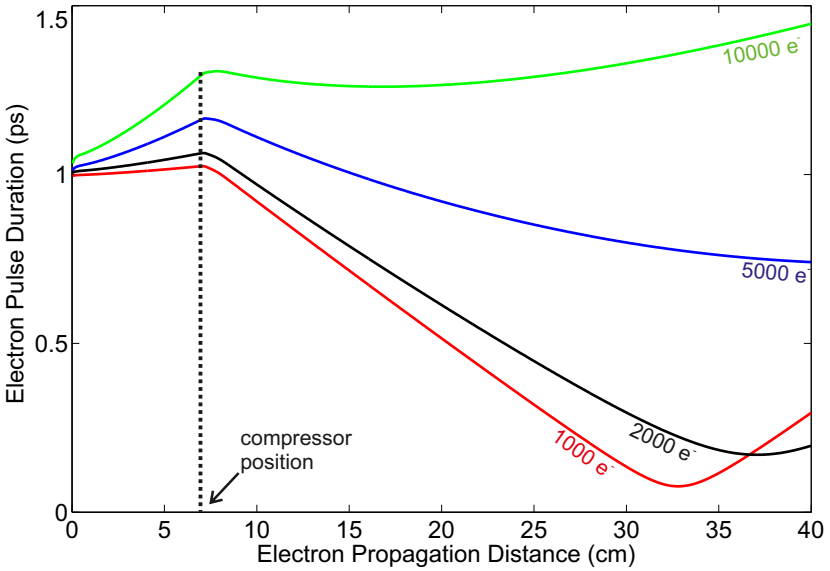

Figure 6.4: Simulated electron pulse duration as a function of the travelling distance when the compressor cavity is placed at 7 cm in the electron beam line for 1000, 2000, 5000 and 10000 electrons per pulse.

The ASTRA results displayed in figure 6.4 are for an electron beam with 50 kV energy, an initial spotsize of 35 µm and an initial pulse duration of 1 ps. It was chosen to have a long initial pulse duration as this makes compression of the pulse easier. Experimentally, the beam can be stretched by employing a UV-stretcher based on two reflective gratings by which the initial pulse duration of the electron beam can be chosen. From the ASTRA results in figure 6.4 it is determined that an electron pulse of 1000 electrons can be numerically compressed to 77 fs, and an electron pulse of 2000 electrons can be compressed to 170 fs. For a pulse of 5000 electrons per pulse it already becomes tough: a pulse duration of 740 fs is achieved which is already worse than the simulations for electron pulses that are not pre-stretched and compressed. In case of 10.000 electrons per pulse, compression in the temporally pre-stretched electron pulse is not achievable as the compressor is only able to temporally 'collimate' the electron beam. The ability of the compressor realised by Dr. Kassier to compress 15.000 electrons to 200 fs is mostly due to the lowered electron energy of 20 keV as opposed to 50 keV in our simulations. Compression is easier for an electron pulse with low electron energy. Figure 6.5 shows an ASTRA simulation under the experimental conditions of his result. As discussed in section 5.3 an initial pulse duration of 220 fs and initial spotsize of 10 µm is assumed for the 20 keV electron beam. The numerical result shows excellent agreement with the experiment: a pulse duration of 200 fs is obtained for 15.000 electrons both experimentally and numerically.

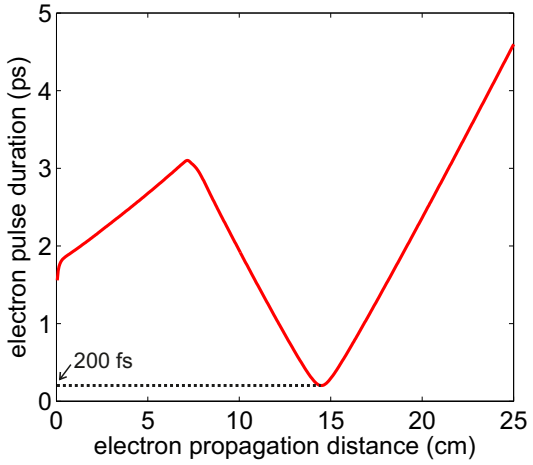

Figure 6.5: Compression of a beam under the experimental conditions in [53].

6.3 Preliminary Experimental Results

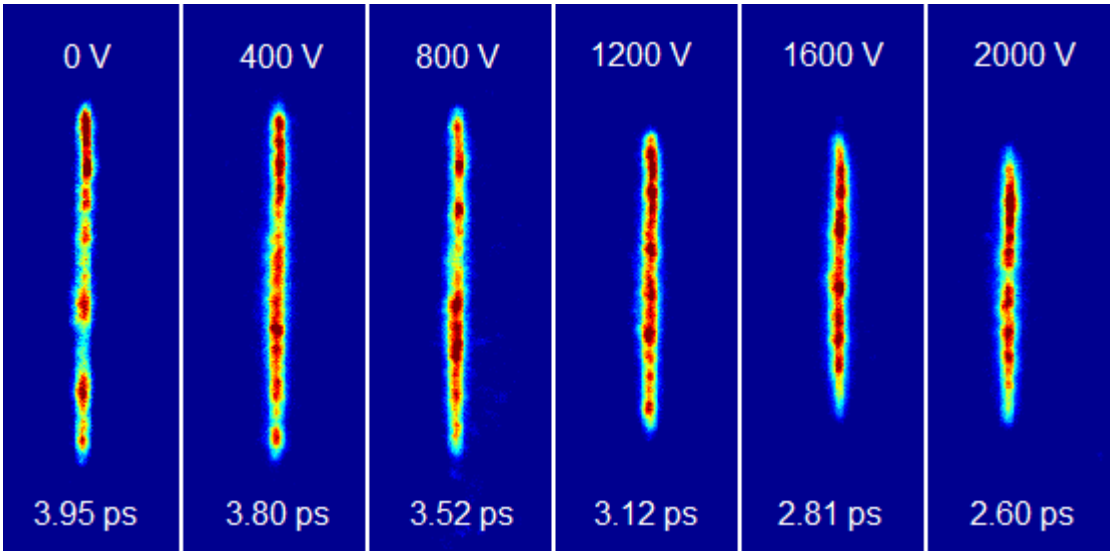

Figure 6.6: Streaked pulse duration measurements, measured at 6 – 7 cm behind the compressor with a streak camera (30 keV kinetic energy electron pulses with a 3000 electrons/pulse Faraday cup read-out).

Compression experiments with the compact compressor from figure 6.2 were performed. Temporal durations of the compressed pulses were measured with the streak camera from figure 5.7 in the configuration as in figure 6.1. The pulse duration of the pulse was measured at a distance of 6 – 7 cm behind the compressor for different oscillating voltages applied to the cavity plates. This was done for a pulse with 3.000 electrons/pulse read-out of the Faraday cup (which, as established in chapter 5, we believe corresponds to 5.500 electrons/pulse) with

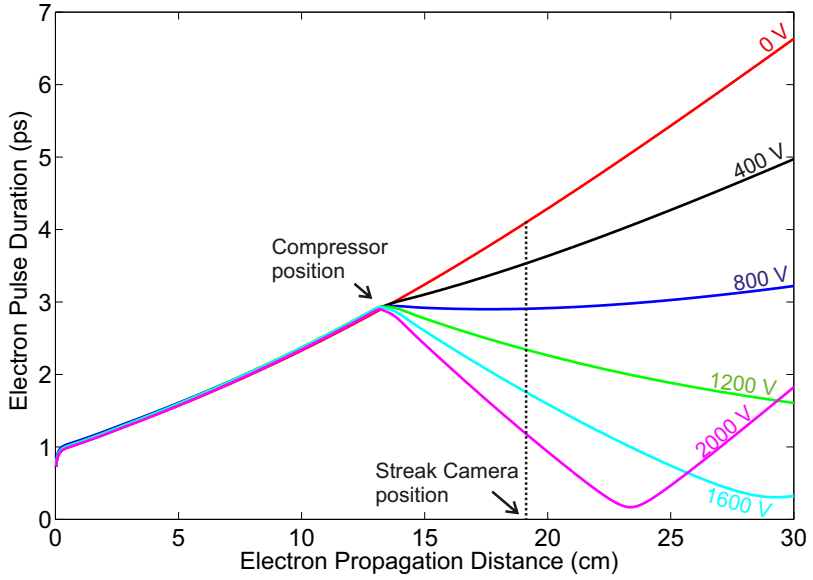

Figure 6.7: Numerical ASTRA simulation for electron pulse recompression under the experimental conditions of figure 6.6: 220 fs initial pulse duration, 5500 electrons per pulse, 20 keV electron energy and a 10 µm spotsize.

a kinetic energy of 20 keV. The streaks for different voltages on the compressor are shown in figure 6.6 and the measured pulse durations are indicated.

Shown in figure 6.7 are numerical electron compression results from ASTRA. The electric field in the compressor that was simulated in figure 6.3 was used as an input. In the simulation, the compressor was placed around 13 cm behind the electron gun and applied to 0, 400, 800, 1200, 1600 and 2000 V. Values for the electron pulse duration 6 cm after the compressor are extracted and compared with the experimental result. This comparison is displayed in figure 6.8. Compression in the experiments is not as strong as predicted by simulations. The poor compression as compared to the results in ref. [53] is because the temporal duration was not measured at the temporal focus of the beam as space in the old chamber is limited. Reasons for the compression to be not as good as numerically predicted could be due to a number of reasons:

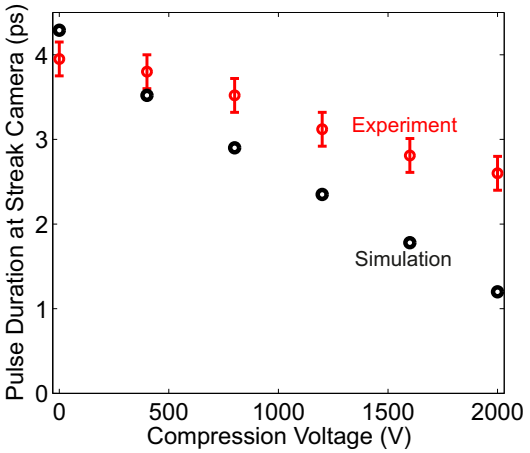

Figure 6.8: Experimental values (red dots) and simulated values (black dots) for the pulse duration of compressed electron pulses (at streak camera position).

- The conductivity of the photoswitch when unpumped is too high, resulting in a leak current such that the streak plates can't maintain the maximum voltage of 2000 V.
- The beam is misaligned such that it is not perpendicular with the cavity plates, resulting in the beam not to experience the maximum field strength for compression.
- The streak cavity plates are misaligned with respect to each other, resulting in the beam not to experience the maximum field strength for compression.
- The charging and discharging of the plates does not happen homogeneously due to the volume of the streak plates resulting in the simulated fields not to represent the experiment.

In principle, it was shown by simulations and a proof-of-principal experiment that the proposed method for compression is experimentally feasible. The compression achieved by the simplified version from figure 6.2 is not as good as predicted by simulations and experiments although pulse durations were not measured at the temporal focus of the compressor. However, the fact that the compact model does compress the incoming electron pulse shows promise for future compressor designs based on the same principle to be more effective. Additional simulation and experimental work will be required to optimise the compressor to a compact and experimentally implementable version that can achieve sufficient compression (<500 fs) for a high electron number per pulse (>10.000 electrons) at a position in the vacuum where a sample can reasonably be placed.

7. Summary

Molecular movies with atomic precision in real time have been made with femtosecond electron diffractometers, and the field is still expanding. A femtosecond laser is employed in a pump-probe experiment in order to make such movies, of which the temporal resolution is determined by the pump and probe pulse duration. In our laboratory, the pump consists of an ultrashort laser pulse with a temporal duration of 150 fs. The fluence of this pump that photo-excites the sample controls the deposited energy in the target which in turn determines the induced processes. The probe beam consists of a sub-picosecond electron beam with 50 keV kinetic energy. The electrons are generated by focussing frequency tripled laser light ($\lambda = 258$ nm) onto a photo-cathode, thereby utilising the photo-electric effect. The generated electrons are accelerated in a strong electric field inside the electron gun and diffracted of the sample under investigation. The generated electron diffraction pattern reveals the atomic structure of the sample.

The electron gun for electron pulse generation is designed, developed and characterised in this work. The short electron pulses take a 'snapshot' of the state of the sample by means of an electron diffraction pattern, with a temporal resolution determined by the electron pulse duration. The time of the snapshot acquirement after laser pulse pump impact can be chosen by tuning the pump-probe arrival time by means of a mechanical delay stage in the optical pump path. In this way, molecular movies of photo-induced processes can be achieved which has the potential to shed light on the driving mechanisms in the excited processes.

A double MCP and phosphor screen configuration detects the electron pattern snapshots after diffraction from a sample, revealing the samples atomic structure. The FED experiments, including the detection system, are housed in an ultra high vacuum (pressures in the 10^{-9} mbar regime). A vacuum is necessary for electron propagation and suppression of electric break down in the high electric fields in the electron gun. An ultra high vacuum is needed to suppress condensation of matter onto cryo-cooled samples during experiments. The vacuum chamber is equipped with a load lock system for sample exchange, and a closed cycle cryostat to achieve, monitor and control cryogenic temperatures at the sample.

Exotic behaviour of the radical salts of dicyanoquinonediimine, $M(R_1,R_2\text{-DCNQI})_2$, make it an interesting candidate for FED experiments. Changes in conductivity as a function of temperature are caused by charge density wave (CDW) formations as observed in static X-ray diffraction patterns. Time resolved macroscopic measurements for conductivity and expansion of the crystal have shown that this insulator-to-conductor transition can be photoswitched. This makes a study of the temporal evolution of atomic structural changes during the switching by employing FED experimentally feasible. A study that provides a direct look at the structural dynamics happening in these crystals (for example $Cu(DCNQI)_2$) at an atomic level is still missing. A molecular movie of this switching process will shed light on the driving mechanisms and the influences of alloy-specific time constants of the transitions.

Observing atomic precision by means of electron diffraction patterns was done in our old HV-FED set-up for the samples at room temperature and sub-phase transition temperature ($T<78$ K for d_6-$Cu(DCNQI)_2$). The external pressure that the sample is subjected to, combined with condensation of matter onto the sample at low temperature, complicates the capturing of a diffraction pattern of the crystal in its insulating phase.

Electrostatic and space tracking simulations show that optimisation of the electron gun design is crucial for minimising the temporal duration of the generated electron pulses that are debunched due to Coulomb repulsion and electron energy spread. Simulations and experiments for the new electron gun design that characterise the broadening effects have shown that sub-picosecond temporal durations are achievable for less than 3500 electrons if the sample is placed within 7 cm of the electron gun. This temporal duration will improve significantly when the gun operates at a higher voltage and when the initial spotsize is increased. The latter will lead to loss in transverse coherence length, but the experimental lower limit of 11 nm — calculated from a $TiSe_2$ diffraction pattern — is sufficient to resolve the crystal structure. It is also a good improvement compared to the transverse coherence length of 9.6 nm of the old system.

Achievements in FED have been made in recompressing debunched electron pulses with high electron numbers. For experiments performed at low repetition rate, the number of electrons in a single pulse must be increased so that atomic structures can be observed with significant signal. To maintain sufficiently low temporal duration, electron pulse compression is necessary. We presented an alternative compressor that is based on an optically initiated RLC-circuit resonance which is easier and more compact to implement.

Conclusion

The task of designing an electron gun where temporal duration is minimised was approached by performing numerical pulse duration calculations. As a starting point, existing electron gun designs were simulated, and alterations to these geometries were made to find the optimal design. The outcome of this task achieved an experimentally implemented new electron gun. Main improved consequences of this gun are that, firstly, it is easier to maintain than the old gun due to increased accessibility. Secondly, this gun can operate on a higher voltage (50 kV instead of 30 kV) which will further improve the experimentally determined temporal and spatial resolution, as well as the (already improved) detection sensitivity. Lastly, its compact design results in improved spatial resolution when a short UV lens is employed. When acquiring diffraction patterns (of for example $Cu(DCNQI)_2$), this all adds up to having brighter and sharper images with better temporal and spatial resolution.

The achievements in the $Cu(DCNQI)_2$ project are the high-quality electron diffraction patterns that have been acquired from prepared samples. Although no CDW-peaks were observed for samples that were cooled to below the phase transition temperature, the encouraging consequence is the development of the CF-flanged ultra-high vacuum FED-setup. With pressures that should be at least an order of magnitude lower, the rate of condensation of matter onto the sample should take an order of magnitude longer. This makes the set-up more suitable for low-temperature electron diffraction which should ultimately lead to the observation of the CDW-state of the sample in an electron diffraction pattern.

The efforts of recompressing debunched electron pulses will be implemented in the time resolved structural dynamics experiments. An accomplishment during the scope of this work is the numerically proven potential for experimental implementation of an oscillating RLC-circuit driven compressor. This is reinforced by preliminary experimental results.

Ultimately the goal of this project are time-resolved high quality electron diffraction experiments on the low temperature photo-induced insulator-to-conductor switching of organic radical ion salts (as the one mentioned above). Our ultrabright pulsed electron beam with sub-ps temporal resolution achieved by electron pulse compression will be employed to do so. Experimental results will have far-reaching effects in the field of ultrafast structural dynamics as small alterations to the complex organic compound influence the dynamical transitions that are happening, arguably leading to these transitions being 'controllable' by selection of different alloys.

Appendices

A. Cryo-Cooled $Cu(DCNQI)_2$ Diffraction Patterns

Numerous attempts to observe the insulating phase (below 78 K for h_8-$Cu(DCNQI)_2$, for which most of the experiments were done) in $Cu(DCNQI)_2$ were performed. These experiments were done with intense collaboration with Dr. Nicolas Erasmus, Florian Hüwe who was a guest for a few months and Aminat Suleiman. In this appendix, diffraction patterns of these attempts are included. For all these diffraction patterns, the repetition rate of the electron pulse was 1 kHz and the exposure time of a single diffraction pattern is 60 seconds.

From the experiments in figure A.1 it becomes apparent that the background signal at 60 K (fig. A.1a) is increased significantly compared to the room temperature diffraction pattern (fig. A.1b). Pumping the sample with the fundamental ($\lambda = 775$ nm) laser (fluence 8 $\mu J/cm^2$) when the sample is at cold temperature in an attempt to recover the diffraction pattern by evaporating the matter that condensated onto the sample had no influence on diffraction quality whatsoever. The quality of the diffraction pattern after the cooldown is significantly worse (fig. A.1c), revealing deterioration during cooldown.
From the molecular extinction graph of $DCNQI^-$-solution in figure A.2[24] it was deducted that the crystal absorption for $\lambda = 775$ nm is relatively low which could explain the inefficient evaporation of matter from the sample. Therefore, the following attempts were done in the

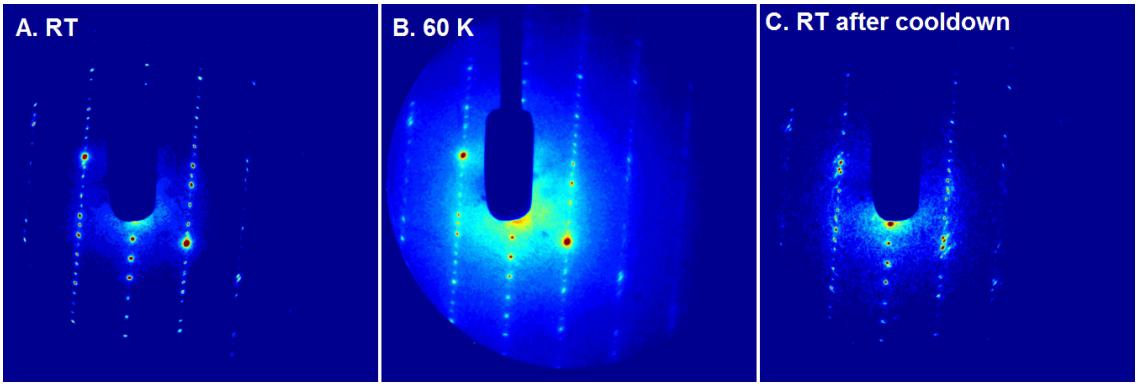

Figure A.1: A single diffraction pattern of $Cu(DCNQI)_2$ at room temperature (a), 60 K (b) and at room temperature after the cool down.

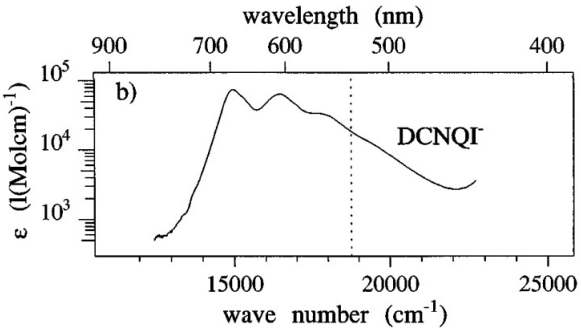

Figure A.2: Molecular extinction of the $DCNQI^-$ anion in CH_3CN solution at 300 K (graph taken from ref. [24]).

old HV chamber to suppress the condensation problem:

- An attempt to pump the sample while cooling down with a fluence of 1.5 μJ/cm^2 – 2.0 μJ/cm^2 at $\lambda = 387$ nm (frequency doubled by a BBO crystal) is shown in figure A.3a-c. From the graph in figure A.3d it becomes clear that the Bragg intensity decreases over time as the sample sits at low temperature (pattern lost after 30 minutes), and the sample is permanently damaged.

- The following attempt was to pump a cooled sample with a 0.03 μ/cm^2 fluence at $\lambda =$ 650 nm. This is shown in figure A.3e-g. Again, the sample deteriorates as it sits at low temperature and after 30 minutes at cold temperature only 20% of the signal is left (fig. A.3h). The sample quality has permanently deteriorated.

- A 0.03 μ/cm^2 fluence at $\lambda = 665$ nm was tried to employ as a pump for condensation evaporation. This is shown in figure A.4a-c and from figure A.4d it becomes clear that that again the signal has dropped (in this experiment to 20% after 40 minutes) and permanent damage has been done to the sample.

- A new approach was to thermally connect a heater to the sample. The reasoning was that the heater could keep the sample (that is thermally connected to the cryostat coldfinger) at room temperature. Once the crystat coldfinger is at its minimum temperature, the heater could be switched off causing the sample to go from room temperature to below phase transition temperature in a very short time (cooling rate of around 4.5 K/min). It was argued that the faster cooling will give matter in the vacuum less time to condensate onto the sample, giving us more time to take good quality low-temperature diffraction patterns. This approach is shown A.4e-g. The sample seems to be quite well preserved after a cooldown and after being at 39 K for 34 minutes 80% of the Bragg signal is still left (fig. A.4h). Good quality low-temperature diffraction patterns were obtained. However, the damage threshold for exposure to cryogenic temperatures is very sample dependent and subsequent attempts with a similar approach have failed.

- Because of a sudden contraction of 0.4% at the phase transition, the following approach was suggested: Cool the sample down with a slow cooling rate (1 K/min). In order to suppress condensation onto the sample during the slow cool-down, the sample is 'parked' in a metal 'shield', which is also thermally coupled to the cryostat. This could protect the sample against condensation as with the ballistic assumption of a coefficient of 1.00 at these temperatures; most matter should condensate onto the shield. Success has been booked with this approach as shown in figure A.5a-c. After 30 minutes of being at cold temperature without being shielded, 80% of the signal is still left (fig. A.5d) and no significant damages have been generated in the sample during cooldown. High-quality low-temperature diffraction patterns were obtained in this way. Unfortunately, the success of this approach is very sample dependent. Figure A.6e-f shows an experiment under similar conditions where the sample does break after a cool down. Figure A.7a-e shows a single sample that has been cooled down twice under similar experimental conditions. Again, for each cool down of the sample, diffraction image quality has worsened significantly.

Conclusively, although some of the above-mentioned approaches have shown improvements in the condensation problem (fig. A.1–A.7), these experiments are not repeatable and obtaining high-quality low-temperature diffraction pattern remains a problem. Hence, a better vacuum is needed.

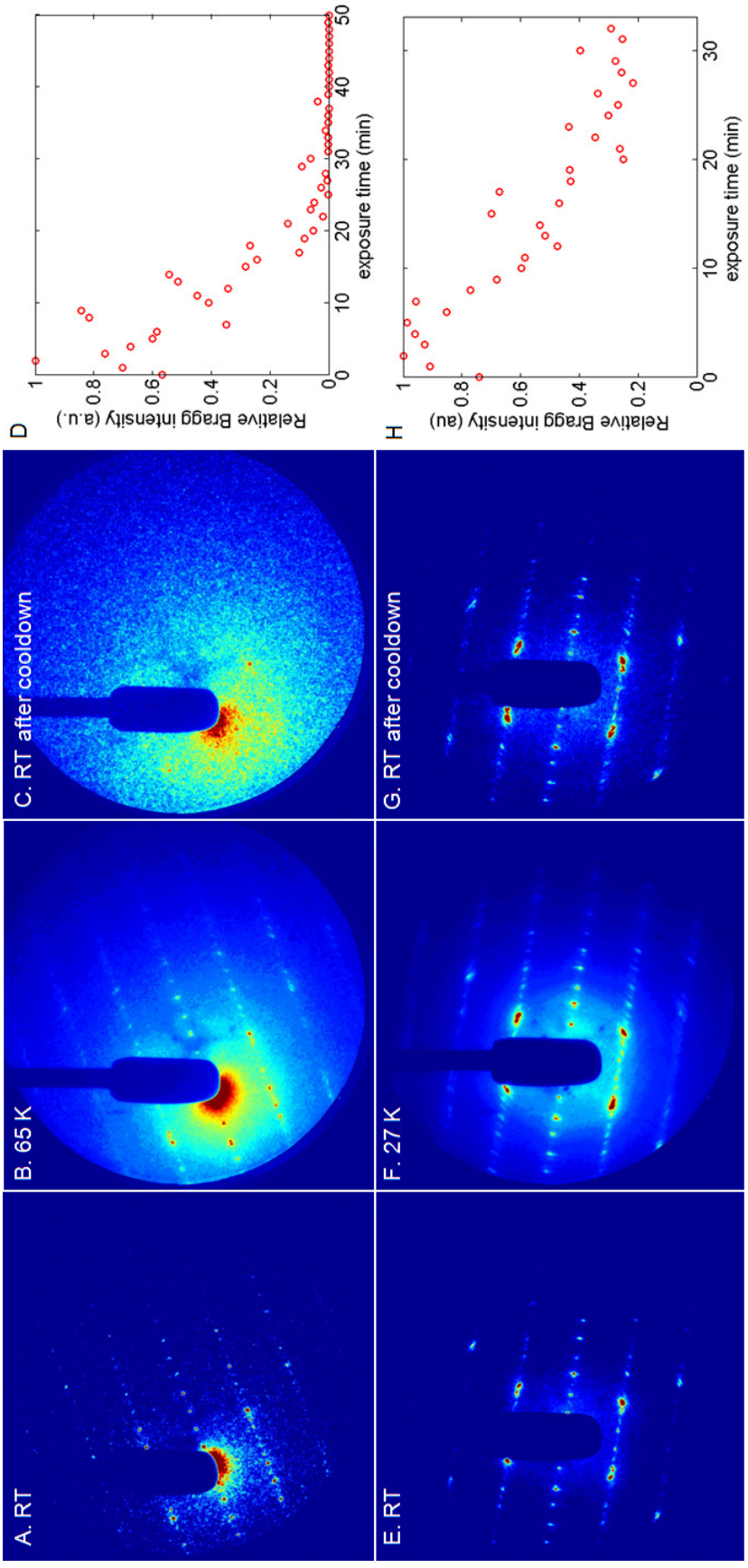

Figure A.3: (a) A single diffraction pattern at room temperature. (b) An average of 10 images at 60 K while the sample was exposed to 1.5 μJ/cm^2 – 2.0 μJ/cm^2 (at $\lambda = 387$ nm) pump fluence. (c) A pattern taken at room temperature after the cooldown. (d) The Bragg intensity drop of the patterns at cold temperature that are shown in b revealing loss of the Bragg signal after 30 minutes. (e) A single diffraction pattern at room temperature. (f) An average of 64 images at 60 K while the sample was exposed to 0.03 μJ/cm^2 (at $\lambda = 650$ nm) pump fluence. (g) A pattern taken at room temperature after the cooldown. (h) The Bragg intensity drop of the patterns at cold temperature that are shown in g showing a drop of 70% Bragg intensity after 30 minutes.

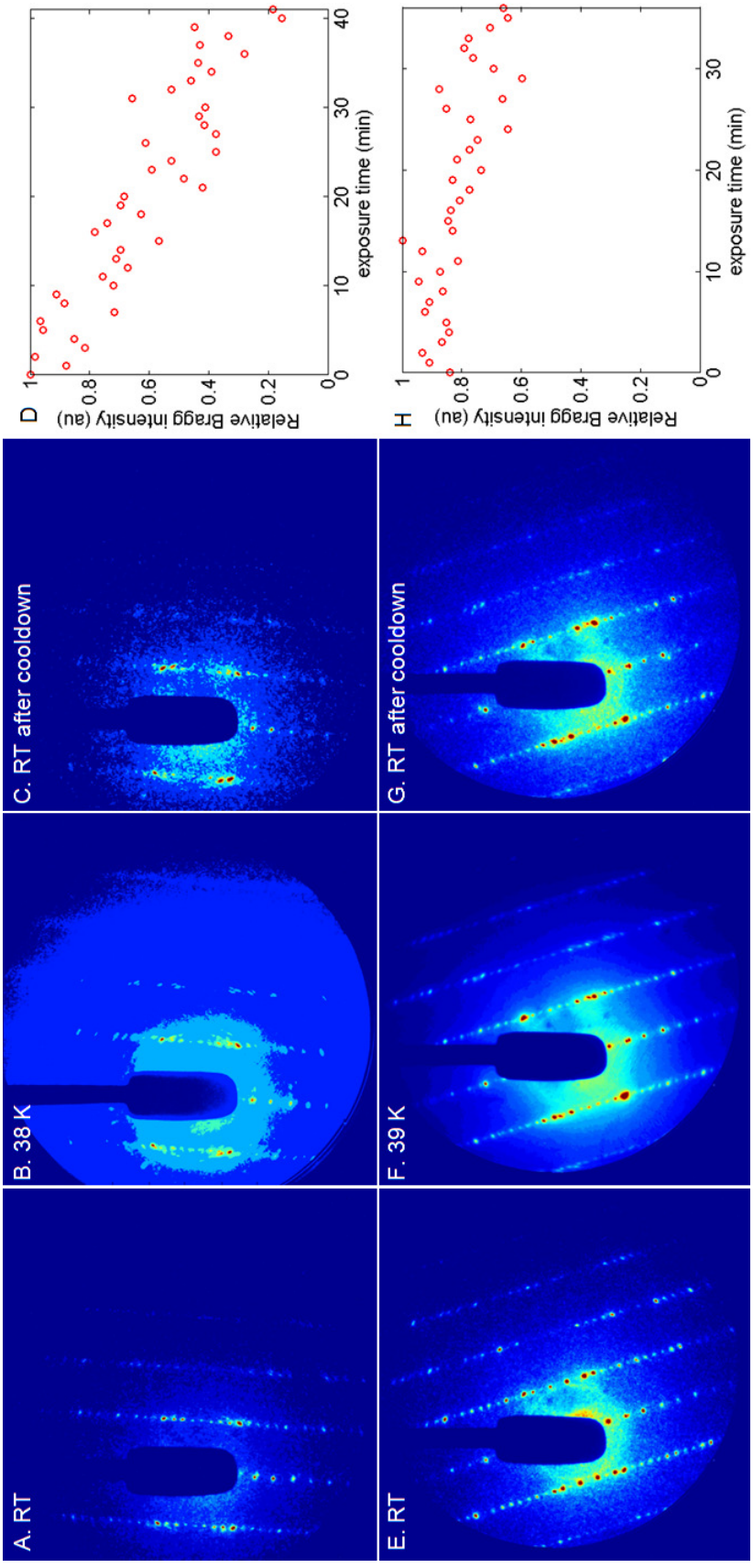

Figure A.4: (a) A single diffraction pattern at room temperature. (b) A single diffraction image taken at 38 K while the sample was exposed to 0.03 μJ/cm^2 (at λ = 665 nm) pump fluence. (c) A pattern taken at room temperature after the cooldown. (d) The Bragg intensity drop of the patterns at cold temperature that are shown in b revealing a loss of 70% in Bragg signal after 40 minutes. (e) A single diffraction pattern at room temperature. (f) An average of 39 images at 39 K while the sample was cooled down as fast as possible with a heater. (g) A pattern taken at room temperature after the cooldown. (h) The Bragg intensity drop of the patterns at cold temperature that are shown in g. After 35 minutes, 70 % of the Bragg signal is still left.

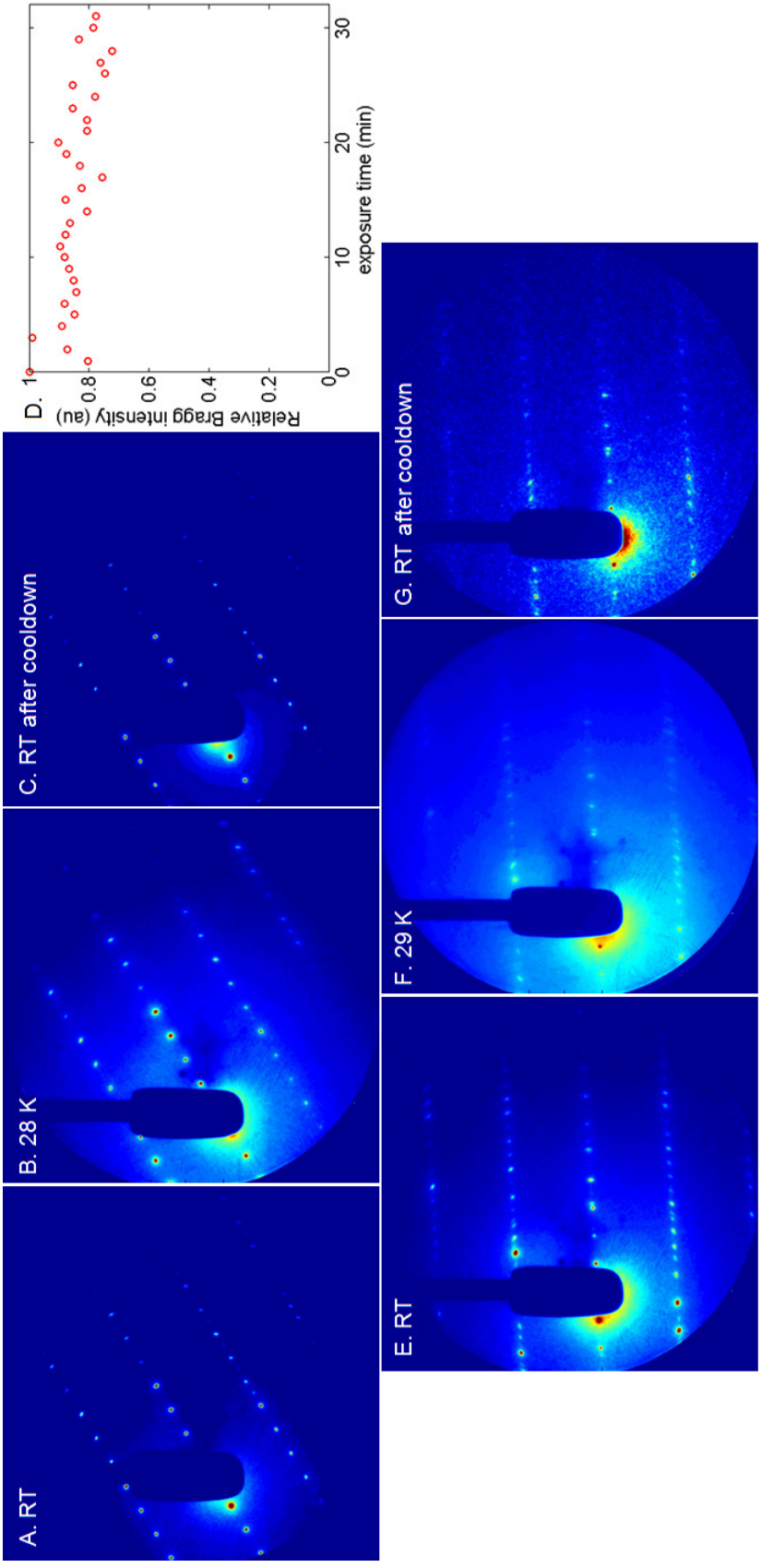

Figure A.5: (a) An average of 10 diffractions pattern at room temperature. (b) An average of 10 diffraction images taken at 28 K where the cooling rate was set to be 1 K/min. (c) An average of 18 patterns taken at room temperature after the cooldown. (d) The Bragg intensity drop of the patterns at cold temperature that are shown in b. After 30 minutes, still 80% of the Bragg signal is observed. (e) An average of 30 diffraction patterns at room temperature. (f) An average of 55 images at 29 K with the sample being cooled with a cooling rate of 1 K/min. (g) A single pattern taken at room temperature after the cooldown (g).

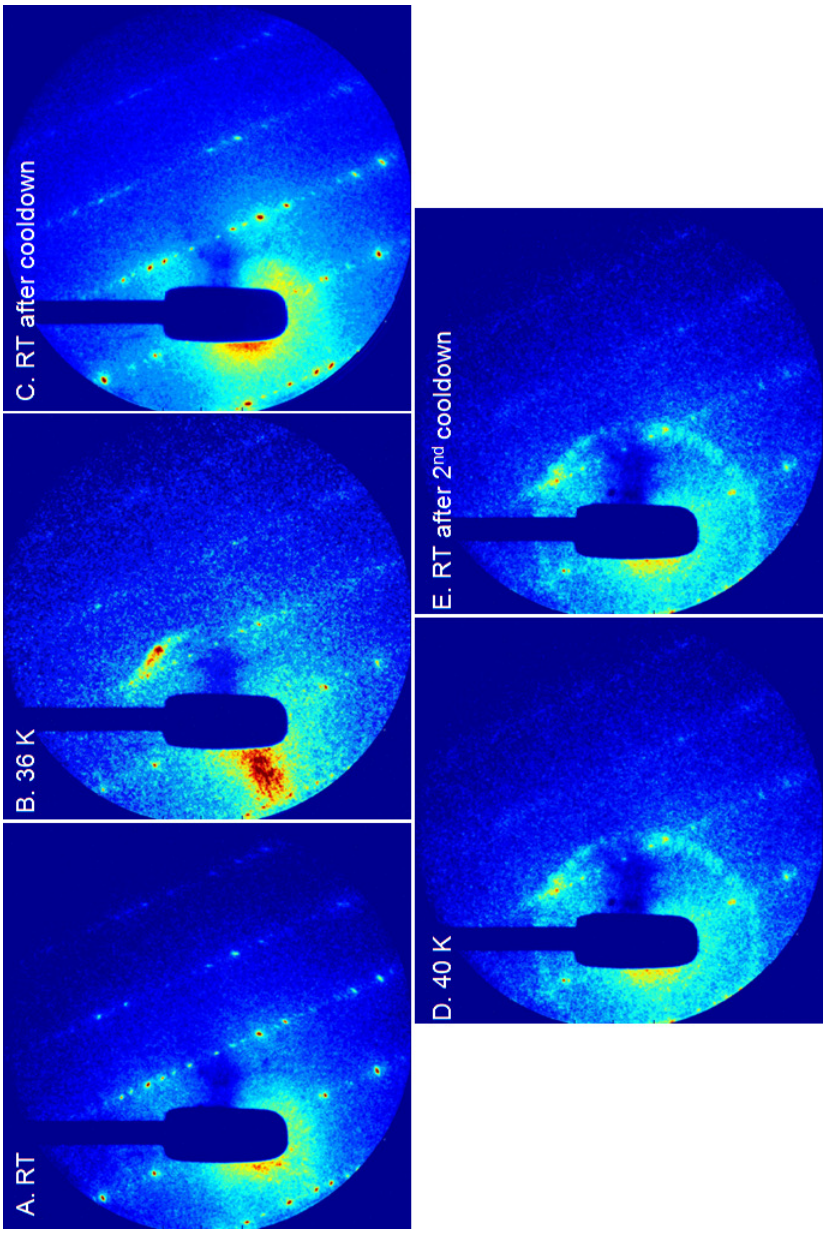

Figure A.6: (a) An average of 10 diffractions pattern at room temperature. (b) An average of 10 diffraction images taken at 36 K where the cooling rate was set to be 1 K/min. (c) An average of 10 patterns taken at room temperature after the cooldown. (d) An average of 10 images at 40 K during second cooldown. (e) An average of 10 images at room temperature after second cooldown.

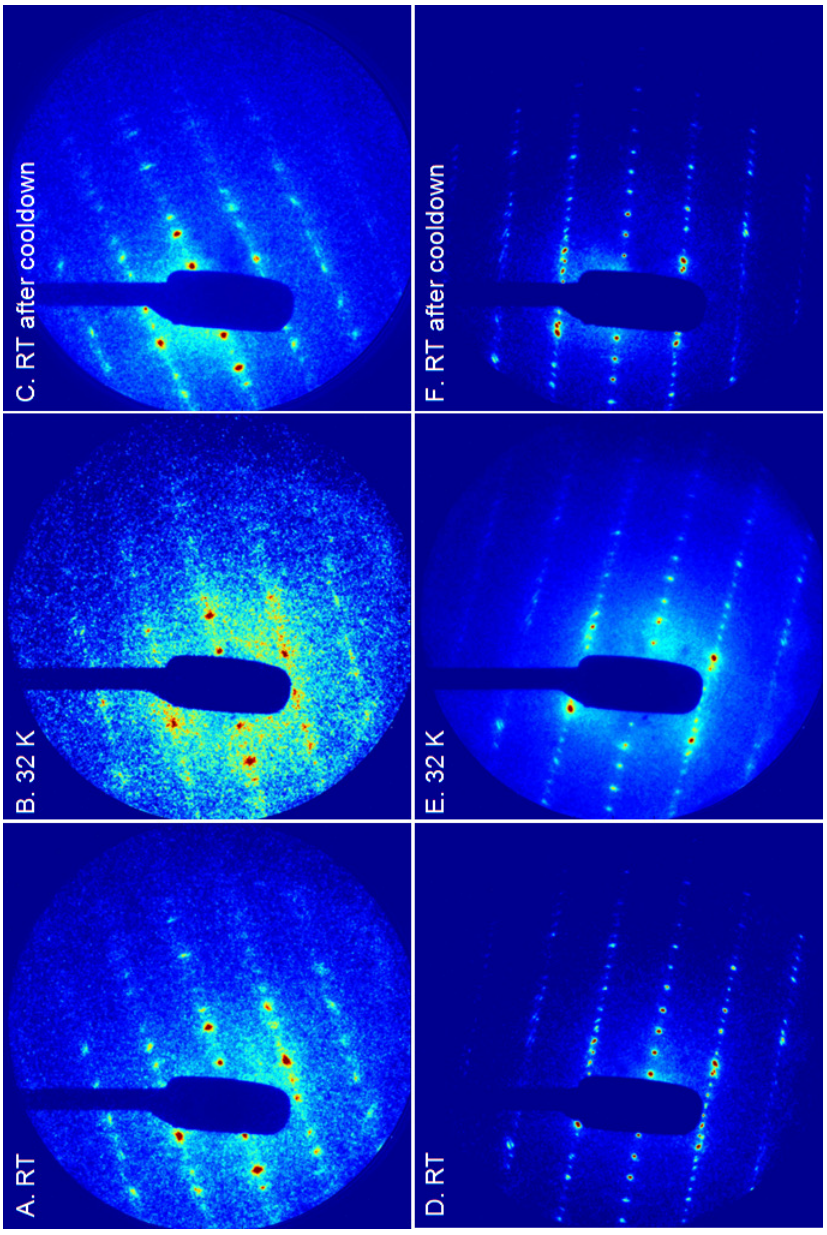

Figure A.7: (a) A single diffraction pattern at room temperature. (b) a single diffraction image taken at 32 K where the cooling rate was set to be 1 K/min. (c) A single pattern taken at room temperature after the cooldown. (d) A single pattern at room temperature. (e) An average of 10 diffraction patterns taken at 32 K. (f) A single diffraction pattern taken at room temperature after the cooldown.

Bibliography

[1] Näsänen, R., Ojanpää, H., Tanskanen, T. and Päällysaho, J.: Estimation of temporal resolution of object identification in human vision. *Experimental brain research*, vol. 172, no. 4, pp. 464–471, 2006.

[2] Edgerton, H.E.: Bullet through apple. *MIT Museum Collections*, 1964.

[3] Dwyer, J.R., Hebeisen, C.T., Ernstorfer, R., Harb, M., Deyirmenjian, V.B., Jordan, R.E. and Miller, R.J.D.: Femtosecond electron diffraction: "making the molecular movie". *Philosophical transactions of the Royal Society A*, vol. 364, no. 1840, pp. 741–778, 2006.

[4] Miller, R.J.D.: Mapping atomic motions with ultrabright electrons: The chemists gedanken experiment enters the lab frame. *Annual Review of Physical Chemistry*, vol. 65, no. 1, pp. 583–604, 2014.

[5] Barty, A., Küpper, J. and Chapman, H.N.: Molecular imaging using x-ray free-electron lasers. *Annual Review of Physical Chemistry*, vol. 64, no. 1, pp. 415–435, 2013.

[6] Siwick, B.J., Dwyer, J.R., Jordan, R.E. and Miller, R.D.: An atomic-level view of melting using femtosecond electron diffraction. *Science*, vol. 302, no. 5649, pp. 1382–1385, 2003.

[7] Eichberger, M., Schäfer, H., Krumova, M., Beyer, M., Demsar, J., Berger, H., Moriena, G., Sciaini, G. and Miller, R.D.: Snapshots of cooperative atomic motions in the optical suppression of charge density waves. *Nature*, vol. 468, no. 7325, pp. 799–802, 2010.

[8] Erasmus, N., Eichberger, M., Haupt, K., Boshoff, I., Kassier, G., Birmurske, R., Berger, H., Demsar, J. and Schwoerer, H.: Ultrafast dynamics of charge density waves in 4 h b-tase 2 probed by femtosecond electron diffraction. *Physical review letters*, vol. 109, no. 16, p. 167402, 2012.

[9] Haupt, K., Eichberger, M., Erasmus, N., Von Flotow, A., Demsar, J., Rossnagel, K. and Schwoerer, H.: Ultrafast metamorphosis of a complex charge-density wave. *Submitted*, February 2014.

[10] Eichberger, M., Erasmus, N., Haupt, K., Kassier, G., von Flotow, A., Demsar, J. and Schwoerer, H.: Femtosecond streaking of electron diffraction patterns to study structural dynamics in crystalline matter. *Applied Physics Letters*, vol. 102, no. 12, p. 121106, 2013.

[11] Jean-Ruel, H., Gao, M., Kochman, M.A., Lu, C., Liu, L.C., Cooney, R.R., Morrison, C.A. and Miller, R.D.: Ring-closing reaction in diarylethene captured by femtosecond electron crystallography. *The Journal of Physical Chemistry B*, vol. 117, no. 49, pp. 15894–15902, 2013.

[12] Gao, M., Lu, C., Jean-Ruel, H., Liu, L.C., Marx, A., Onda, K., Koshihara, S.-y., Nakano, Y., Shao, X., Hiramatsu, T. *et al.*: Mapping molecular motions leading to charge delocalization with ultrabright electrons. *Nature*, vol. 496, no. 7445, pp. 343–346, 2013.

[13] Reckenthaeler, P., Centurion, M., Fuß, W., Trushin, S.A., Krausz, F. and Fill, E.E.: Time-resolved electron diffraction from selectively aligned molecules. *Physical review letters*, vol. 102, no. 21, p. 213001, 2009.

[14] Hensley, C.J., Yang, J. and Centurion, M.: Imaging of isolated molecules with ultrafast electron pulses. *Physical review letters*, vol. 109, no. 13, p. 133202, 2012.

[15] Pedrotti, F.L., Pedrotti, L.S. and Pedrotti, L.M.: *Introduction to optics*, vol. 2. 1993.

[16] Haupt, K.: *Phase Transitions in Transition-Metal Dichalcogenides studied by Femtosecond Electron Diffraction*. PhD, Universiteit Stellenbosch, 2013.

[17] Beeston, B.E.: Electron diffraction and optical diffraction techniques. 1972.

[18] Elsayed-Ali, H. and Herman, J.: Picosecond time-resolved surface-lattice temperature probe. *Applied physics letters*, vol. 57, no. 15, pp. 1508–1510, 1990.

[19] Dowell, D.H. and Schmerge, J.F.: Quantum efficiency and thermal emittance of metal photocathodes. *Physical Review Special Topics-Accelerators and Beams*, vol. 12, no. 7, p. 074201, 2009.

[20] Siwick, B.J., Dwyer, J.R., Jordan, R.E. and Miller, R.D.: Ultrafast electron optics: Propagation dynamics of femtosecond electron packets. *Journal of Applied Physics*, vol. 92, no. 3, pp. 1643–1648, 2002.

[21] Erasmus, N.: *Ultrafast Structural Dynamics in 4Hb-TaSe2 Observed by Femtosecond Electron Diffraction*. PhD, Universiteit Stellenbosch, 2013.

[22] Erasmus, N.: *The Development of an Electron Gun for Performing Ultrafast Electron Diffraction Experiments*. MSc, Universiteit Stellenbosch, 2009.

[23] Kassier, G.: *Ultrafast Electron Diffraction: Source Development, Diffractometer Design and Pulse Characterisation*. PhD, Universiteit Stellenbosch, 2010.

[24] Karutz, F., Von Schuetz, J., Wachtel, H. and Wolf, H.: Optically reversed peierls transition in crystals of cu (dicyanoquinonediimine) 2. *Physical review letters*, vol. 81, no. 1, p. 140, 1998.

[25] Kato, R.: Conductive copper salts of 2, 5-disubstituted n, n'-dicyanobenzoquinonediimines (dcnqis): Structural and physical properties. *Bulletin of the Chemical Society of Japan*, vol. 73, no. 3, pp. 515–534, 2000.

[26] Kobayashi, A., Kato, R., Kobayashi, H., Mori, T. and Inokuchi, H.: The organic π-electron metal system with interaction through mixed-valence metal cation: Electronic and structural properties of radical salts of dicyano-quinodiimine,(dme-dcnqi)< sub> 2</sub> cu and (mecl-dcnqi)< sub> 2</sub> cu. *Solid state communications*, vol. 64, no. 1, pp. 45–51, 1987.

[27] Sinzger, K., Huenig, S., Jopp, M., Bauer, D., Bietsch, W., von Schuetz, J.U., Wolf, H.C., Kremer, R.K. and Metzenthin, T.: The organic metal (me2-dcnqi) 2cu: dramatic changes in solid-state properties and crystal structure due to secondary deuterium effects. *Journal of the American Chemical Society*, vol. 115, no. 17, pp. 7696–7705, 1993.

[28] Collin, S., Merano, M., Gatri, M., Sonderegger, S., Renucci, P., Ganière, J.-D. and Deveaud, B.: Transverse and longitudinal space-charge-induced broadenings of ultrafast electron packets. *Journal of applied physics*, vol. 98, no. 9, p. 094910, 2005.

[29] Gahlmann, A., Park, S.T. and Zewail, A.H.: Ultrashort electron pulses for diffraction, crystallography and microscopy: Theoretical and experimental resolutions. *Physical Chemistry Chemical Physics*, vol. 10, no. 20, pp. 2894–2909, 2008.

[30] van der Geer, S., de Loos, M., Vredenbregt, E. and Luiten, O.: Ultracold electron source for single-shot, ultrafast electron diffraction. *Microscopy and Microanalysis*, vol. 15, no. 04, pp. 282–289, 2009.

[31] Chatelain, R.P., Morrison, V., Godbout, C., van der Geer, B., de Loos, M. and Siwick, B.J.: Space-charge effects in ultrafast electron diffraction patterns from single crystals. *Ultramicroscopy*, vol. 116, pp. 86–94, 2012.

[32] Baum, P.: On the physics of ultrashort single-electron pulses for time-resolved microscopy and diffraction. *Chemical Physics*, vol. 423, pp. 55–61, 2013.

[33] Ropers, C., Solli, D., Schulz, C., Lienau, C. and Elsaesser, T.: Localized multiphoton emission of femtosecond electron pulses from metal nanotips. *Physical review letters*, vol. 98, no. 4, p. 043907, 2007.

[34] Paarmann, A., Gulde, M., Müller, M., Schäfer, S., Schweda, S., Maiti, M., Xu, C., Hohage, T., Schenk, F., Ropers, C. *et al.*: Coherent femtosecond low-energy single-electron pulses for time-resolved diffraction and imaging: A numerical study. *Journal of Applied Physics*, vol. 112, no. 11, p. 113109, 2012.

[35] Li, R., Tang, C., Du, Y., Huang, W., Du, Q., Shi, J., Yan, L. and Wang, X.: Experimental demonstration of high quality mev ultrafast electron diffraction. *Review of Scientific Instruments*, vol. 80, no. 8, p. 083303, 2009.

[36] Murooka, Y., Naruse, N., Sakakihara, S., Ishimaru, M., Yang, J. and Tanimura, K.: Transmission-electron diffraction by mev electron pulses. *Applied Physics Letters*, vol. 98, no. 25, p. 251903, 2011.

[37] Buck, A., Nicolai, M., Schmid, K., Sears, C.M., Sävert, A., Mikhailova, J.M., Krausz, F., Kaluza, M.C. and Veisz, L.: Real-time observation of laser-driven electron acceleration. *Nature Physics*, vol. 7, no. 7, pp. 543–548, 2011.

[38] Zewail, A.H.: 4d ultrafast electron diffraction, crystallography, and microscopy. *Annu. Rev. Phys. Chem.*, vol. 57, pp. 65–103, 2006.

[39] Gallant, P., Forget, P., Dorchies, F., Jiang, Z., Kieffer, J., Jaanimagi, P., Rebuffie, J., Goulmy, C., Pelletier, J. and Sutton, M.: Characterization of a subpicosecond x-ray streak camera for ultrashort laser-produced plasmas experiments. *Review of Scientific Instruments*, vol. 71, no. 10, pp. 3627–3633, 2000.

[40] Janzen, A., Krenzer, B., Heinz, O., Zhou, P., Thien, D., Hanisch, A., Zu Heringdorf, F.-J.M., Von Der Linde, D. and Von Hoegen, M.H.: A pulsed electron gun for ultrafast electron diffraction at surfaces. *Review of scientific instruments*, vol. 78, no. 1, p. 013906, 2007.

[41] Boshoff, I.: *Ultrafast Electron Diffraction on the Charge Density Wave Compound 4Hb-TaSe2*. MSc, Universiteit Stellenbosch, 2012.

[42] Hebeisen, C.T., Ernstorfer, R., Harb, M., Dartigalongue, T., Jordan, R.E. and Dwayne Miller, R.: Femtosecond electron pulse characterization using laser ponderomotive scattering. *Optics letters*, vol. 31, no. 23, pp. 3517–3519, 2006.

[43] Siwick, B.J., Green, A.A., Hebeisen, C.T. and Miller, R.: Characterization of ultrashort electron pulses by electron-laser pulse cross correlation. *Optics letters*, vol. 30, no. 9, pp. 1057–1059, 2005.

[44] Chatelain, R.P., Morrison, V.R., Godbout, C. and Siwick, B.J.: Ultrafast electron diffraction with radio-frequency compressed electron pulses. *Applied Physics Letters*, vol. 101, no. 8, p. 081901, 2012.

[45] Cao, J., Hao, Z., Park, H., Tao, C., Kau, D. and Blaszczyk, L.: Femtosecond electron diffraction for direct measurement of ultrafast atomic motions. *Applied physics letters*, vol. 83, no. 5, pp. 1044–1046, 2003.

[46] Kassier, G.H., Haupt, K., Erasmus, N., Rohwer, E., Von Bergmann, H., Schwoerer, H., Coelho, S. and Auret, F.D.: A compact streak camera for 150 fs time resolved measurement of bright pulses in ultrafast electron diffraction. *Review of Scientific Instruments*, vol. 81, no. 10, p. 105103, 2010.

[47] GRQNVOLD, F. and Langmyhr, F.: X-ray study of titanium selenides. *Acta Chemica Scandinavica*, vol. 15, no. 1961, pp. 19–19, 1962.

[48] Tokita, S., Hashida, M., Inoue, S., Nishoji, T., Otani, K. and Sakabe, S.: Single-shot femtosecond electron diffraction with laser-accelerated electrons: experimental demonstration of electron pulse compression. *Physical review letters*, vol. 105, no. 21, p. 215004, 2010.

[49] Kassier, G., Haupt, K., Erasmus, N., Rohwer, E. and Schwoerer, H.: Achromatic reflectron compressor design for bright pulses in femtosecond electron diffraction. *Journal of Applied Physics*, vol. 105, no. 11, p. 113111, 2009.

[50] Baum, P. and Zewail, A.: Femtosecond diffraction with chirped electron pulses. *Chemical Physics Letters*, vol. 462, no. 1, pp. 14–17, 2008.

[51] Van Oudheusden, T., Pasmans, P., Van Der Geer, S., De Loos, M., Van Der Wiel, M. and Luiten, O.: Compression of subrelativistic space-charge-dominated electron bunches for single-shot femtosecond electron diffraction. *Physical review letters*, vol. 105, no. 26, p. 264801, 2010.

[52] Gao, M., Jean-Ruel, H., Cooney, R.R., Stampe, J., de Jong, M., Harb, M., Sciaini, G., Moriena, G. and Dwayne Miller, R.: Full characterization of rf compressed femtosecond electron pulses using ponderomotive scattering. *Optics express*, vol. 20, no. 11, pp. 12048–12058, 2012.

[53] Kassier, G., Erasmus, N., Haupt, K., Boshoff, I., Siegmund, R., Coelho, S. and Schwoerer, H.: Photo-triggered pulsed cavity compressor for bright electron bunches in ultrafast electron diffraction. *Applied Physics B*, vol. 109, no. 2, pp. 249–257, 2012.